Winter 2008

DGM-FD: A Finite Difference Scheme Based on the Discontinuous Galerkin Method

Anne Marguerite Fernando
Old Dominion University

DGM-FD: A FINITE DIFFERENCE SCHEME BASED ON THE DISCONTINUOUS GALERKIN METHOD

by

Anne Marguerite Fernando
B.S. January 1986, University of Virginia
M.S. December 1988, Georgia Institute of Technology
M.S. December 2002, Georgia Institute of Technology

A Dissertation Submitted to the Faculty of
Old Dominion University in Partial Fulfillment of the
Requirement for the Degree of

DOCTOR OF PHILOSOPHY

MATHEMATICS AND STATISTICS

OLD DOMINION UNIVERSITY
December 2008

Approved by:

Fang Q. Hu (Director)

Chester E. Grosch (Member)

Hideaki Kaneko (Member)

Jin Wang (Member)

Ruhai Zhou (Member)

ABSTRACT

DGM-FD: A FINITE DIFFERENCE SCHEME BASED ON THE DISCONTINUOUS GALERKIN METHOD

Anne Marguerite Fernando
Old Dominion University, 2008
Director: Dr. Fang Q. Hu

Accurate and efficient numerical wave propagation is important in many areas of study such as computational aero-acoustics (CAA). While dissipation and dispersion errors influence the accuracy of a method, efficiency can be assessed by convergence rates and effective adaptability to different mesh structures. Finite difference and finite element methods are commonly used numerical schemes in CAA. Finite difference methods have the advantages of ease of use as well as high order convergence, but often require a uniform grid, and stable boundary closure can be non-trivial. Finite element methods adapt well to different mesh structures but can become difficult to implement as the order of approximation increases. In this research we formulate a numerical method that has high-order convergence, with strong accuracy for numerical wave numbers, and is adaptive to non-uniform grids. Such a method is developed based on the Discontinuous Galerkin Method (DGM) applied to the hyperbolic equation. Finite difference type schemes applicable to non-uniform grids are proposed. The schemes will be referred to as DGM-FD schemes. These schemes inherit, naturally, some features of the DGM, such as high-order approximations, applicability to non-uniform grids and super-accuracy for wave propagations. Two grid structures are studied. In the first structure, a regular, but non-uniform, finite difference type grid is assumed. In the second structure, some grid points are double-valued and the derivative scheme has a shortened stencil. Fourth-order upwind and third order central schemes are presented as examples of the first grid structure. Fifth-order upwind schemes are derived for the second structure. For non-linear equations, flux finite difference formula are given where no explicit upwind and downwind split of the flux is needed. This is in contrast to existing upwind finite difference schemes in the literature. Stability of the schemes with boundary closures and the super-accuracy for wave propagation problems are investigated and validated. The new schemes are demonstrated by numerical examples including the linearized acoustic

waves, the solution of non-linear Burger's equation and the flat-plate boundary layer problem.

ACKNOWLEDGEMENTS

This research was partly supported by the Old Dominion University Graduate Fellowship Program. I start with a huge thank you to my advisor, Dr. Hu for his time, willingness to share his knowledge, incredible patience with my many emails, for shaping my abilities as a future researcher and, finally, for this terrific research topic. I also wish to thank the other members of the committee, Dr. Grosch, Dr. Kaneko, Dr. Wang and Dr. Zhou for their time and input. I extend great appreciation to the Department of Mathematics and Statistics for giving me the opportunity to finish this degree. Thanks to the Math Department at NC State for their support and the opportunity to study there. A big thanks to the Mathematics Department at Ga Tech, where it all started, and in particular to Dr. William Green for his help in turning my A.B.D. status into a second Masters as well as to Dr. Alfred Andrew for his support and kindness. Many thanks to all the new friends I have made in this ODU Math department, and to existing ones from Ga Tech and NC State, your support both mathematically and emotionally has been very important to me. To my great friend, Dr. Mona Meddin, thank you for your years of love and support. To Dr. William Duane, thanks for the guidance in this thing called 'life'. To my neighbors and good friends at Cheshire Forest, thanks for all of the encouragement and support. Finally, to my dear husband, Andrew W. Crowe and our three wonderful boys, Zach, Colin, and Sam, I am eternally grateful to have you as my place of refuge. Thank you for your love, support and patience while 'Mommy is doing her math again'. You are my loves and my life. This dissertation is dedicated to you.

TABLE OF CONTENTS

LIST OF TABLES

LIST OF FIGURES

Chapter I

INTRODUCTION

As Computational Aeroacoustics (CAA) problems involve wave propagation over long time periods, it is important that the numerical schemes used to solve these problems have low dissipation and low dispersion errors [41, 12]. High-order finite volume schemes and finite difference schemes that are optimized for such properties are widely used in these applications. In addition to wave propagation, numerically modeling some physical phenomena requires that a wide range of relevant space and time scales be accurately represented [30]. Many approaches have been explored such as spectral element methods [21], high order discontinuous Galerkin finite element methods [15], dispersion relation preserving methods [41] and compact schemes [30]. The accuracy in discrete dispersion relation is often used in ranking methods for precision in wave propagation [3]. Finite difference methods which demonstrate this precision are the compact schemes and dispersion relation preserving (DRP) schemes [30, 41].

The finite difference schemes usually require a uniform grid. This restriction prevents efficient resolution of the solution in sections of the domain for many non-linear applications. Also, at high orders, due to a wide stencil, construction of stable boundary closure schemes for finite difference schemes is often non-trivial [10, 23, 4, 22].

This research proposes a new finite difference type scheme, based on the Discontinuous Galerkin method (DGM), that has strong numerical to exact wave number agreement, high order accuracy with stable boundary closure and adaptability to non-uniform grids [19]. DGM is chosen as the foundation of this new scheme for many reasons. The discontinuous Galerkin method is a finite element method which can be used on non-uniform grids with high-order basis functions and therefore has high order accuracy. DG methods are adept for handling complicated geometries and require relatively simple treatment of boundary conditions in order to maintain high-order accuracy. DG methods can also handle mesh adaptivity adjustments as refinements of the grid can be taken into account without concern about maintaining

This dissertation follows the style of *The Journal of Computational Physics.*

continuity [15]. In this research, finite difference like schemes based on the discontinuous Galerkin method are derived. They will be referred to as the DGM-FD schemes.

The original DG method was introduced by Reed and Hill in 1973 for solving the neutron transport equation [39]. A more formal analysis of DG as applied to ordinary differential equations was performed by LeSaint and Raviart where, if Δx is the grid spacing, they proved a rate of convergence of $(\Delta x)^k$ in one variable defined on Cartesian grids [31]. In 1986 Johnson and Pitkaranta proved a rate of convergence of $(\Delta x)^{k+1/2}$ [29] for general triangulations. Results were confirmed for exact solutions that were assumed to be smooth [40, 32, 33, 18, 37]. On the issue of super-convergence, it was shown that the approximate solution of the DG method super-converges at the Gauss-Radau points [8, 2, 35]. Atkins and Shu introduced quadrature-free implementation of the Runge-Kutta Discontinuous Galerkin (RKDG) and Local Discontinuous Galerkin (LDG) methods [5]. The extension of RKDG methods to general multi-dimensional systems was used in applications to the Euler equations of gas dynamics [7, 6], and further in a five paper series by Cockburn and Shu for numerically solving hyperbolic conservation laws [17, 13, 14, 16]. Further review and discussion of properties of DGM for conservation laws was done by Flaherty et. al. [20]. Studies have also shown that discontinuous Galerkin schemes have strong super-accuracy with low dissipation and dispersion errors for wave propagation problems [27, 36]. Fourier analysis of DGM schemes reveals that the numerical eigenvalues are accurate to order $2p+2$ locally, and therefore $2p+1$ globally, for the decay of the evolution component of the numerical error [25, 27, 3]. DGM also performs well on non-uniform stencils, as studies on numerical reflections at a grid discontinuity reveal that the reflections are just the non-physical or spurious wave mode which dissipate quickly [27].

With DGM-FD we look to improve on current methods and, therefore, a brief review of traditional Finite Difference Schemes [41], Dispersion Relation Preserving [41], Compact Finite Difference Schemes [30, 46], Spectral Volume Schemes [42, 43, 44, 45, 12], and Spectral Difference Schemes [34] is presented.

Traditional finite difference schemes are central schemes whose coefficients are determined via Taylor series. This method has the limitation of needing a uniform grid. While these methods are simple in derivation and implementation, there is no attempt to improve the numerical dispersion relation in these numerical methods.

Stable boundary closure schemes also become non-trivial as the order of approximation, and the number of grid points in the stencil, increases.

The Dispersion Relation Preserving (DRP) scheme is an optimized finite difference scheme that minimizes the error in the numerical wave numbers [41] while consequently reducing the formal order of accuracy. It is simple to use and high-order with strong accuracy for numerical wave numbers. It was motivated by applications to acoustics with the goal of preserving the dispersion relations inherent in the linear Euler equations. The DRP is a marked improvement on standard finite difference schemes for resolution of wave numbers, however, its main draw back is that it also requires a uniform grid [41].

Compact finite difference schemes are high order and preserve numerical wave number accuracy well, but are implicit and are therefore computationally more expensive [30, 46]. Through grid maps, or less desirably, by directly recalculating coefficients for different grids, they can be applied to a non-uniform grid, but there appears no potential for dynamic grid adaptations without the inefficient or perhaps impossible re-calculation of coefficients at each adjustment.

A high-order compact upwind difference schemes with good spectral resolution is recently reported in [46]. With this method finding first derivatives can be as inexpensive as with explicit schemes even for non-periodic boundaries. Also, when implicit, these methods are less costly than the other compact schemes. Resolution optimization is used to enhance the spectral resolution and this produces a scheme with very high spectral accuracy. The boundary closures are stable and also have spectral accuracy. This method is, however, upwind and therefore wave splitting is required. Furthermore, as with the previously mentioned methods, there appears to be no adaptivity to non-uniform meshes.

Spectral (finite) volume methods (SFV) for conservation laws achieve high-order accuracy by subdividing each spectral volume into control volumes and using cell-averaged data from these control volumes to reconstruct a high-order approximation [42]. Riemann solvers are used for fluxes at spectral volume boundaries. Total variational diminishing and bounded limiters are used to remove spurious oscillations near discontinuities. The reconstruction is carried out analytically which saves memory and CPU time compared to high order finite volume method [42, 43, 44, 45]. While these methods are more robust in their handling of discontinuities and non-uniform meshes, they are, however, more complicated to implement and use more computer

time than most finite difference schemes.

Spectral difference (SD) schemes are recently developed high-order methods with an emphasis on efficiency for conservation laws on unstructured grids. It combines structured and unstructured grid methods to obtain computational efficiency, and, utilizes discontinuous high order representations to achieve high order conservation. It is based on a finite-difference formulation, for simplicity, and reported as easier to implement than DGM and spectral volume methods for unstructured grids [34]. The spatial accuracy is verified through studies on examples, but it is unknown if the accuracy of the numerical wave numbers in DGM found by Hu and Atkins in [27] is preserved in this method.

In this research we turn our attention to combining attractive properties of finite element and volume methods with the simplicity and high order accuracy of finite difference schemes. The new methods proposed in this work, DGM-FD schemes, are explicit and will be shown to possess many of the attractive features of the discontinuous Galerkin method including the ease of use on non-uniform grids, high-order accuracy, and low dissipation and low dispersion errors.

The derivation starts with the semi-discrete form of the hyperbolic equation from which a finite difference formula for the first spatial derivative is constructed. Two families of schemes are formed. In the first family, a regular finite difference grid is assumed. Construction of finite difference schemes and boundary closures are illustrated through a fourth-order scheme. Both the central and upwind schemes are given. A flux difference scheme is derived for non-linear problems and a third order scheme is presented. A second family of schemes with an introduction of double valued nodes, is derived, discussed and illustrated with a fifth order scheme. Stability is demonstrated for each variation. The proposed schemes are also applicable to the discretization of second order derivative terms such as those found in the advection-diffusion equation. All the schemes are illustrated by numerical examples including applications on non-uniform grids and use with the linearized Euler equations. Applications for the flux scheme include the non-linear Burger's equation and a flat-plate boundary layer problem with Navier-Stokes governing equations.

Chapter II

FORMULATION OF DERIVATIVE EXPRESSION BASED ON DGM

II.1 INTRODUCTION TO DISCONTINUOUS GALERKIN METHOD

Discontinuous Galerkin method is a finite element method developed in 1973 for the application of solving the neutron transport equation [39]. It follows a formulation for continuous Galerkin finite element methods with the exception of requiring the basis functions to be continuous over element boundaries.

Here is a brief overview of DGM in multiple dimensions [25, 16]. Consider a conservation equation for a quantity in a region, R

$$\frac{\partial \mathbf{u}}{\partial t} + \nabla \cdot \mathbf{f}(\mathbf{u}) = 0 \tag{1}$$

where $\mathbf{f}(\mathbf{u})$ is a flux vector. Let the domain be partitioned into non-overlapping sub-domains or elements, R_i. The discontinuous Galerkin method is a finite element method in which the functions in the approximation space V_h may be discontinuous across element interfaces. The subscript, h, represents the 'size' or measure of element R_i. In the semi-discrete formulation, V_h contains spatial functions

$$V_h = \{\mathbf{v} \in L^1(D) : \mathbf{v}|_{R_i} \in P(R_i)\},$$

where $P(R_i)$ is a polynomial space defined on R_i. The numerical approximation of the solution is then obtained by solving a weak formulation of (1), where the space, V_h, is also used as the test space. We now identify a polynomial basis for each R_i.

Let $B_i = \{\mathbf{v}_\ell^i\}_{\ell=0,...N_i-1}$, with each $\mathbf{v}_\ell^i$ defined on R, be a local basis set such that

$$\text{Span}(B_i)|_{R_i} = P(R_i), \quad \text{Supp}(\mathbf{v}_\ell^i(\mathbf{x})) = R_i, \quad \ell = 0, ..., N_i - 1$$

We can see that $V_h = \text{Span}(\cup \mathbf{v}_\ell^i)$. We now assume each R_i to have dimension, N and that the basis polynomials on each B_i are each degree, $N-1$ and require that the approximate solution $\mathbf{u}_h$ satisfies

$$\int_{R_i} \mathbf{v}_l^i \left(\frac{\partial \mathbf{u}_h}{\partial t} + \nabla \cdot \mathbf{f}(\mathbf{u}_h) \right) d\mathbf{x} = 0, \quad \ell = 0, ..., N-1 \tag{2}$$

on each element R_i. Using Green's formula (or integration by parts in one space dimension), (2) is re-written as

$$\int_{R_i} \mathbf{v}_l^i \frac{\partial \mathbf{u}_h}{\partial t} - \nabla \mathbf{v}_l^j \cdot \mathbf{f}(\mathbf{u}_h) \; d\mathbf{x} + \int_{\partial R_i} \mathbf{v}_l^i \mathbf{f}(\mathbf{u}_h) \cdot \mathbf{n} \; ds = 0 \quad \ell = 0, ...N-1 \tag{3}$$

where ∂R_i is the boundary of R_i and $\mathbf{n}$ denotes the unit outward normal vector. As the data are discontinuous across the interface of contiguous domains, two unequal values of $\mathbf{u}_h$ i.e. $\mathbf{u}_h^i$ inside R_i and $\mathbf{u}_h^j$ outside R_i are available in the data at the interface. As there is not one value of the flux at the interface, a numerical flux $\mathbf{f}_{num}$ is used to evaluate the interface flux in the surface integral term of (3)

$$\mathbf{f}(\mathbf{u}_h) \cdot \mathbf{n}|_{\partial R_i} = \mathbf{f}_{num}(\mathbf{u}_h^i, \mathbf{u}_h^j, \mathbf{n}). \tag{4}$$

The above formulation can be interpreted as a standard Galerkin method in each element with a weak boundary condition.

The accuracy of the method is at least $(p+\frac{1}{2})$ if the basis functions are polynomials of degree at most p [29]. On a cartesian grid the order of accuracy is $(p+1)^{th}$ order if the basis functions are polynomials of degree at most p [31]. We will stipulate the method to be order $(p+1)$ if the basis functions are polynomials of degree p or less.

II.2 EXTRACTION OF A FINITE DIFFERENCE FORMULA

Consider the discontinuous Galerkin method, in one dimensional space, for

$$\frac{\partial u}{\partial t} + \frac{\partial f(u)}{\partial x} = 0 \tag{5}$$

with the spatial domain in x partitioned into elements E_n=[s_{n-1},s_n], $n = 0, 1, ..., N$. The numerical solution for $x \in$[s_{n-1},s_n] is expanded as:

$$u_h^n(x,t) = \sum_{\ell=0}^{p} u_{n\ell}(t)\phi_\ell^n(\xi) \tag{6}$$

$$f_h^n(x,t) = \sum_{\ell=0}^{p} f_{n\ell}(t)\phi_\ell^n(\xi) \tag{7}$$

where $x = \frac{1}{2}(s_{n-1}+s_n)+\frac{h_n}{2}\xi$, $h_n = s_n - s_{n-1}$, and $\phi_\ell^n(\xi)$ are the basis functions with order p on element E_n, in parametric coordinate ξ, where $-1 \leq \xi \leq 1$.

We note that if $\phi_\ell^n(\xi)$ are chosen to be the Lagrange polynomials, the expansion coefficients will be the same as the nodal values of the numerical solution. This has the advantage that no inversion of a system is required to obtain the expansion

coefficients. If x_{ni} is the i^{th} of the $(p+1)$ collocation points on n^{th} element E_n we have the basis, in terms of x, as

$$\phi_\ell^n(x) = \frac{\prod_{i\neq\ell}(x - x_{ni})}{\prod_{i\neq\ell}(x_{n\ell} - x_{ni})}$$

with the property

$$\phi_{\ell'}^n(x_{n\ell}) = \delta_{\ell'\ell}.$$

By the weak formulation in DGM, it is required that

$$\int_{s_{n-1}}^{s_n} [\frac{\partial u_h^n}{\partial t} + \frac{\partial f_h^n}{\partial x}]\phi_{\ell'}^n(x)dx = 0 \tag{8}$$

for ℓ'=0,1,...p.

Following an integration by parts and the change of variable given above that maps, for each n, E_n=[s_{n-1}, s_n] to [-1, 1], we get

$$\frac{h_n}{2}\int_{-1}^{1} \frac{\partial u_h^n}{\partial t}\phi_{\ell'}^n(\xi)d\xi + f^*(s_n)\phi_{\ell'}^n(1) - f^*(s_{n-1})\phi_{\ell'}^n(-1) - \int_{-1}^{1} f_h^n \frac{\partial \phi_{\ell'}^n}{\partial \xi}d\xi = 0 \tag{9}$$

for ℓ'=0,1,...p, where f^* denotes the flux at the end points of the element. This is necessary as at the interface between two elements, or at element end points s_{n-1} and s_n, the flux vector f^* is not uniquely determined and a flux formula has to be supplied to complete the discretization process, see (4). Here, following the work in ref [27], the Lax-Friedrichs flux formula

$$f^* = \frac{1}{2}\left[f^+ + f^- - \theta|\lambda|(u^+ - u^-)\right] \tag{10}$$

will be applied with $\lambda = ||\frac{\partial f}{\partial u}||_{max}$, the largest eigenvalue of $[\frac{\partial f}{\partial u}]$ or the largest, in magnitude, eigenvalue of the jacobian of flux, f. The $^+$ and $^-$ refer to the values at the right and left of an element boundary, respectively as shown in Figure (1).

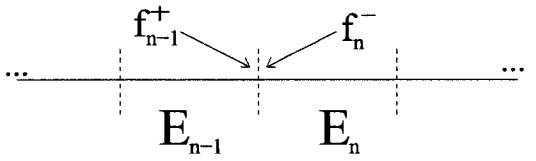

FIG. 1: A description of the location of f^+, f^- on an a grid with element boundary.

With (10), the semi-discrete expression can then be written explicitly as

$$\frac{h_n}{2}\sum_{\ell=0}^{p}\frac{\partial u_{n\ell}}{\partial t}\int_{-1}^{1}\phi_\ell^n(\xi)\phi_{\ell'}^n(\xi)d\xi$$

$$+\frac{1}{2}\left\{\sum_{\ell=0}^{p}f_{nl}\phi_\ell^n(1)+\sum_{\ell=0}^{p}f_{(n+1)l}\phi_\ell^n(-1)-\theta|a|_{max}(\sum_{\ell=0}^{p}u_{(n+1)l}\phi_\ell^n(-1)-\sum_{\ell=0}^{p}u_{nl}\phi_\ell^n(1))\right\}\phi_{l'}^n(1)$$

$$-\frac{1}{2}\left\{\sum_{\ell=0}^{p}f_{(n-1)l}\phi_\ell^n(1)+\sum_{\ell=0}^{p}f_{nl}\phi_\ell^n(-1)-\theta|a|_{max}(\sum_{\ell=0}^{p}u_{nl}\phi_\ell^n(-1)-\sum_{\ell=0}^{p}u_{(n-1)l}\phi_\ell^n(1))\right\}\phi_{l'}^n(-1)$$

$$-\sum_{\ell=0}^{p}f_{nl}\int_{-1}^{1}\phi_l^n(\xi))\frac{\partial\phi_{\ell'}^n(\xi)}{\partial\xi}d\xi=0 \tag{11}$$

for $\ell'=0,1,...p$. In the above, $a=\frac{\partial f}{\partial u}$ and θ, $0\le\theta\le 1$, is a parameter that controls the upwinding effects, with $\theta=0$ being a central scheme and $\theta=1$ being the fully upwinded scheme.

We also assume that the basis functions are the same for all elements (except those next to the boundary), denoted by

$$\phi_\ell^n(\xi)=P_\ell(\xi)$$

and define matrices

$$\mathbf{Q}=\{q_{\ell'\ell}\}=\{\int_{-1}^{1}P_\ell P_{\ell'}d\xi\},\quad \mathbf{Q}'=\{q'_{\ell'\ell}\}=\{\int_{-1}^{1}P_\ell\frac{\partial P_{\ell'}}{\partial\xi}d\xi\},$$

$$\mathbf{B}_{(a,b)}=\{b_{\ell'\ell}\}=\{P_{\ell'}(a)P_\ell(b)\} \tag{12}$$

and vectors $\vec{u}^n=\begin{bmatrix}u_{n0}\\u_{n1}\\\vdots\\u_{np}\end{bmatrix}$, $\vec{f}^n=\begin{bmatrix}f_{n0}\\f_{n1}\\\vdots\\f_{np}\end{bmatrix}$

Then, as given in [27], the semi-discrete equation (11) can be written as

$$\frac{h_n}{2}\mathbf{Q}\frac{\partial\vec{u}^n}{\partial t}-\frac{1}{2}\mathbf{B}_{(-1,1)}\vec{f}^{n-1}+[\frac{1}{2}\mathbf{B}_{(1,1)}-\frac{1}{2}\mathbf{B}_{(-1,-1)}-\mathbf{Q}']\vec{f}^n+\frac{1}{2}\mathbf{B}_{(1,-1)}\vec{f}^{n+1}$$

$$+\frac{\theta}{2}|a|_{max}\{-\mathbf{B}_{(-1,1)}\vec{u}^{n-1}+[\mathbf{B}_{(1,1)}+\mathbf{B}_{(-1,-1)}]\vec{u}^n-\mathbf{B}_{(1,-1)}\vec{u}^{n+1}\}=0$$

or

$$\frac{h_n}{2}\mathbf{Q}\frac{\partial \vec{u}^n}{\partial t}+\mathbf{M}_-\vec{f}^{n-1}+\mathbf{M}_0\vec{f}^{n}+\mathbf{M}_+\vec{f}^{n+1}+\theta|a|_{max}\{\mathbf{N}_-\vec{u}^{n-1}+\mathbf{N}_0\vec{u}^{n}+\mathbf{N}_+\vec{u}^{n+1}\}=0 \quad (13)$$

where it is found that

$$\mathbf{M}_- = -\frac{1}{2}\mathbf{B}_{(-1,1)} \quad (14)$$

$$\mathbf{M}_0 = \frac{1}{2}\mathbf{B}_{(1,1)} - \frac{1}{2}\mathbf{B}_{(-1,-1)} - \mathbf{Q}' \quad (15)$$

$$\mathbf{M}_+ = \frac{1}{2}\mathbf{B}_{(1,-1)} \quad (16)$$

and

$$\mathbf{N}_- = -\frac{1}{2}\mathbf{B}_{(-1,1)} = \mathbf{M}_- \quad (17)$$

$$\mathbf{N}_0 = \frac{1}{2}\mathbf{B}_{(1,1)} + \frac{1}{2}\mathbf{B}_{(-1,-1)} \quad (18)$$

$$\mathbf{N}_+ = -\frac{1}{2}\mathbf{B}_{(1,-1)} = -\mathbf{M}_+ \quad (19)$$

As $\mathbf{Q}$ is not singular because the basis polynomials are linearly independent (with respect to standard L_2 inner product) we may apply $\frac{2}{h_n}\mathbf{Q}^{-1}$ to both sides of (13) to get:

$$\frac{\partial \vec{u}^n}{\partial t}+\frac{2}{h_n}\left\{\bar{\mathbf{M}}_-\vec{f}^{n-1}+\bar{\mathbf{M}}_0\vec{f}^{n}+\bar{\mathbf{M}}_+\vec{f}^{n+1}+\theta|a|_{max}(\bar{\mathbf{M}}_-\vec{u}^{n-1}+\bar{\mathbf{N}}_0\vec{u}^{n}-\bar{\mathbf{M}}_+\vec{u}^{n+1})\right\}=0 \quad (20)$$

where

$$\bar{\mathbf{M}}_- = \mathbf{Q}^{-1}\mathbf{M}_-,\ \ \bar{\mathbf{M}}_+ = \mathbf{Q}^{-1}\mathbf{M}_+,\ \ \bar{\mathbf{M}}_0 = \mathbf{Q}^{-1}\mathbf{M}_0,\ \ \bar{\mathbf{N}}_0 = \mathbf{Q}^{-1}\mathbf{N}_0$$

It is at this point that we propose an idea that is the cornerstone for the rest of this research and dissertation. By comparing the original PDE $\frac{\partial u}{\partial t}+\frac{\partial f}{\partial x}=0$ with the discretized version in (20) it is clear that we get a discretization formula for the spatial derivative of $\vec{f}^n$ as

$$\frac{\partial \vec{f}^n}{\partial x} = \frac{2}{h_n}\left\{\bar{\mathbf{M}}_-\vec{f}^{n-1}+\bar{\mathbf{M}}_0\vec{f}^{n}+\bar{\mathbf{M}}_+\vec{f}^{n+1}+\theta||a||_{max}\left(\bar{\mathbf{M}}_-\vec{u}^{n-1}+\bar{\mathbf{N}}_0\vec{u}^{n}-\bar{\mathbf{M}}_+\vec{u}^{n+1}\right)\right\} \quad (21)$$

In particular, if we let $f=au$, we get an expression for the derivative of $\vec{u}^n$:

$$\frac{\partial \vec{u}^n}{\partial x} = \frac{2}{h_n}\left\{\bar{\mathbf{M}}_- \vec{u}^{n-1} + \bar{\mathbf{M}}_0 \vec{u}^n + \bar{\mathbf{M}}_+ \vec{u}^{n+1} + \theta\frac{|a|}{a}(\bar{\mathbf{M}}_- \vec{u}^{n-1} + \bar{\mathbf{N}}_0 \vec{u}^n - \bar{\mathbf{M}}_+ \vec{u}^{n+1})\right\} \tag{22}$$

or:

$$\frac{\partial \vec{u}^n}{\partial x} = \frac{2}{h_n}\left\{(1+\frac{\theta|a|}{a})\bar{\mathbf{M}}_- \vec{u}^{n-1} + (\bar{\mathbf{M}}_0 + \frac{\theta|a|}{a}\bar{\mathbf{N}}_0)\vec{u}^n + (1-\frac{\theta|a|}{a})\bar{\mathbf{M}}_+ \vec{u}^{n+1}\right\} \tag{23}$$

This derivation is general for any choice of basis polynomials and any choice of collocation points. As mentioned earlier if the basis polynomials are chosen to be the Lagrange interpolating polynomials then the expansion coefficients from (6) and (7), $u_{n\ell'}(t)$ and $f_{n\ell'}(t)$ are simply the nodal values, $u_h^n(x_{n\ell'}, t)$ and $f_h^n(x_{n\ell'}, t)$, which are the numerical solutions on element n at collocation point $x_{n\ell'}$. The equations from this section will be used to develop schemes in the following chapters.

Chapter III

GRID STRUCTURES I, DGM - FINITE DIFFERENCE SCHEME

The formulation derived in the previous chapter can be applied to any family of basis functions, but as noted, when the basis functions $\phi_\ell^n(\xi)$ are chosen to be the Lagrange interpolating polynomials, the expansion coefficients $u_{n\ell}$ become the same as the nodal values of the numerical solution at the prescribed nodes. The nodal points within element E_n will be denoted by $x_{n\ell}$, $\ell = 0, 1, ...p$, where p is the order of the basis functions. Various finite-difference-like schemes can be derived by the formulas given in (21) and (23) based on particular choices on the distribution of nodal points.

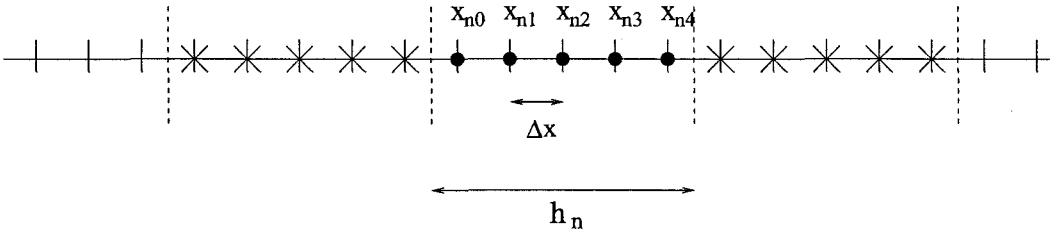

FIG. 2: Schematic of a finite difference grid partitioned into elements of length $h_n = (p+1)\Delta x$, where Δx is the grid size and p is the order of the basis functions.

For instance, a uniform grid system, with a given Δx, that is often found in finite difference methods, can be broken into elements of length $h = (p+1)\Delta x$ with the element boundary placed at the middle of the two grid points of neighboring elements, as shown in Figure (2). In this case, the nodal points on the transformed coordinate ξ, $-1 \leq \xi \leq 1$, are

$$\xi_i = -\frac{p}{p+1} + \frac{2i}{p+1}, \; i = 0, 1, 2, ...p \tag{24}$$

and the basis functions are

$$P_\ell(\xi) = \frac{\Pi_{i=0, i\neq\ell}^{p}(\xi - \xi_i)}{\Pi_{i=0, i\neq\ell}^{p}(\xi_\ell - \xi_i)}, \; \ell = 0, 1, 2, ...p \tag{25}$$

Then the finite difference scheme can be derived by substituting (25) into formulation (11) where the matrices are computed according to (12) and (14)-(19).

III.1 FORMULATION

III.1.1 Interior Scheme

A fourth-order ($p = 4$) scheme is given below as an example. The finite difference formula for a set of five grid points, as illustrated in Figure (2), is yielded as

$$\frac{\partial}{\partial x}\begin{bmatrix} u_{n0} \\ u_{n1} \\ u_{n2} \\ u_{n3} \\ u_{n4} \end{bmatrix} = \frac{2}{h_n}\left(1+\theta\frac{|a|}{a}\right)\bar{\mathbf{M}}_{-}\begin{bmatrix} u_{(n-1)0} \\ u_{(n-1)1} \\ u_{(n-1)2} \\ u_{(n-1)3} \\ u_{(n-1)4} \end{bmatrix} + \frac{2}{h_n}\left(\bar{\mathbf{M}}_0+\theta\frac{|a|}{a}\bar{\mathbf{N}}_0\right)\begin{bmatrix} u_{n0} \\ u_{n1} \\ u_{n2} \\ u_{n3} \\ u_{n4} \end{bmatrix}$$

$$+\frac{2}{h_n}\left(1-\theta\frac{|a|}{a}\right)\bar{\mathbf{M}}_{+}\begin{bmatrix} u_{(n+1)0} \\ u_{(n+1)1} \\ u_{(n+1)2} \\ u_{(n+1)3} \\ u_{(n+1)4} \end{bmatrix} \tag{26}$$

where, using (24) and (25), it is found that

$$\bar{\mathbf{M}}_{-} = \begin{bmatrix} \frac{-29141}{102400} & \frac{37467}{25600} & \frac{-786807}{256000} & \frac{87423}{25600} & \frac{-262269}{102400} \\ \frac{22379}{102400} & \frac{-28773}{25600} & \frac{604233}{256000} & \frac{-67137}{25600} & \frac{201411}{102400} \\ \frac{-525}{4096} & \frac{675}{1024} & \frac{-2835}{2048} & \frac{1575}{1024} & \frac{-4725}{4096} \\ \frac{-3941}{102400} & \frac{5067}{25600} & \frac{-106407}{256000} & \frac{11823}{25600} & \frac{-35469}{102400} \\ \frac{12299}{102400} & \frac{-15813}{25600} & \frac{332073}{256000} & \frac{-36897}{25600} & \frac{110691}{102400} \end{bmatrix}$$

$$\bar{\mathbf{M}}_0 = \begin{bmatrix} \frac{-97037}{38400} & \frac{38191}{6400} & \frac{-5007}{1600} & \frac{8227}{19200} & \frac{9479}{12800} \\ \frac{-33669}{12800} & \frac{14153}{19200} & \frac{3117}{3200} & \frac{2149}{6400} & \frac{-13693}{38400} \\ \frac{1895}{1536} & \frac{-1955}{768} & 0 & \frac{1955}{768} & \frac{-1895}{1536} \\ \frac{13693}{38400} & \frac{-2149}{6400} & \frac{-3117}{3200} & \frac{-14153}{19200} & \frac{33669}{12800} \\ \frac{-9479}{12800} & \frac{-8227}{19200} & \frac{5007}{1600} & \frac{-38191}{6400} & \frac{97037}{38400} \end{bmatrix}$$

$$\bar{\mathbf{N}}_0 = \begin{bmatrix} \frac{24997}{10240} & \frac{-7161}{2560} & \frac{227367}{128000} & \frac{-57}{2560} & \frac{-1631}{2048} \\ \frac{-19747}{10240} & \frac{6207}{2560} & \frac{-248913}{128000} & \frac{339}{512} & \frac{1309}{10240} \\ \frac{2625}{2048} & \frac{-1125}{512} & \frac{2835}{1024} & \frac{-1125}{512} & \frac{2625}{2048} \\ \frac{1309}{10240} & \frac{339}{512} & \frac{-248913}{128000} & \frac{6207}{2560} & \frac{-19747}{10240} \\ \frac{-1631}{2048} & \frac{-57}{2560} & \frac{227367}{128000} & \frac{-7161}{2560} & \frac{24997}{10240} \end{bmatrix}$$

$$\tilde{\mathbf{M}}_+ = \begin{bmatrix} \frac{-110691}{102400} & \frac{36897}{25600} & \frac{-332073}{256000} & \frac{15813}{25600} & \frac{-12299}{102400} \\ \frac{35469}{102400} & \frac{-11823}{25600} & \frac{106407}{256000} & \frac{-5067}{25600} & \frac{3941}{102400} \\ \frac{4725}{4096} & \frac{-1575}{1024} & \frac{2835}{2048} & \frac{-675}{1024} & \frac{525}{4096} \\ \frac{-201411}{102400} & \frac{67137}{25600} & \frac{-604233}{256000} & \frac{28773}{25600} & \frac{-22379}{102400} \\ \frac{262269}{102400} & \frac{-87423}{25600} & \frac{786807}{256000} & \frac{-37467}{25600} & \frac{29141}{102400} \end{bmatrix}$$

A central difference scheme is obtained by letting $\theta = 0$ in (26). On the other hand, a choice of $\theta = 1$ will yield the upwind ($a > 0$) and downwind ($a < 0$) schemes.

III.1.2 Non-uniform grids

As mentioned in the introduction, a finite difference method which can adapt to non-uniform grids while keeping the same scheme coefficients is one of the goals of this research.

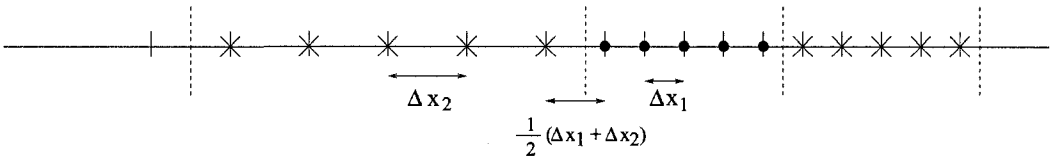

FIG. 3: Schematic of a grid structure with nonuniform grids.

DGM-FD has this property, provided that there is a transition grid between two different spacings, as shown in figure (3) above.

DGM-FD allows grid size to shift in groups of $p+1$ collocation points (per element) with a transition grid inserted where the spacing, Δx_1, on one element changes to another spacing Δx_2. As this method is based on an FEM, the changes in grid size must be done element by element rather than by grid points. However, as we shall see with the insertion of the transitional grid point, the coefficients of the scheme stay the same with the change in grid spacing reflected in the value of h_n used in (26).

We now proceed to verifying that with the transition grid, the coefficients generated by in (26) or in particular **III.1.1**, and in the following section, **III.1.3**, involving boundary closure, will remain the same.

Recall the matrices defined in (12) as they determine the DGM-FD coefficients. As they are dependent solely on the basis polynomials, P, it suffices to show that these stay the same with a change of grid spacing.

Let $\hat{x} \in E_n$=$[s_{n-1},s_n]$. With the change of variable, $x = \frac{1}{2}(s_{n-1}+s_n)+\frac{h_n}{2}\xi$, there is a corresponding $\hat{\xi}$. Let $\xi \in$ [-1, 1] and the basis functions on neighboring elements E_{n-1} and E_{n+1} be

$$P_\ell(\xi) = \frac{\Pi_{i=0,i\neq\ell}^{p}(\xi-\xi_i)}{\Pi_{i=0,i\neq\ell}^{p}(\xi_\ell-\xi_i)},\ \ell = 0,1,...p \tag{27}$$

with spacing Δx_2. Let the spacing on E_n be Δx_1 and call the basis functions on E_n

$$\hat{P}_\ell(\xi) = \frac{\Pi_{i=0,i\neq\ell}^{p}(\xi-\hat{\xi}_i)}{\Pi_{i=0,i\neq\ell}^{p}(\hat{\xi}_\ell-\hat{\xi}_i)},\ \ell = 0,1,...p \tag{28}$$

With the transition grid, each collocation point on the elements retains the same relative spacing (see figure (3)) as s_{n-1} maps to -1 and s_n maps to 1 with nodal point $\hat{x}_{n\ell}$ mapping to $\xi_\ell = -\frac{p}{p+1}+\frac{2\ell}{p+1}$ where ξ_ℓ are the collocation points on $E_{n-1} = [s_{n-2}, s_{n-1}]$ and $E_{n+1} = [s_n, s_{n+1}]$. Consequently, $\hat{\xi}_i = \xi_i$ for each i = 0,1,...p and the denominators of (27) and (28) are the same. Likewise, as ξ is given, the numerators are the same. Therefore, $P_\ell(\xi)$=$\hat{P}_\ell(\xi)$ for all $\xi \in$ [-1,1]. As this is true for each ℓ = 0,...p, the basis polynomials are indeed the same.

As the transition grid insures that the basis polynomials are the same on elements of different lengths, we have that the coefficients in (12) remain the same which is the property we seek.

Any element or portion of the domain can be formulated this way, including regions that contain the boundary.

III.1.3 Boundary closures

The DGM formulation can also be used to derive the difference schemes for the boundary grids. In figures (2) and (3), the nodal points are on the interior of the elements, and yet implementation of boundary conditions often require the boundary to be on collocation points. To reconcile this, the first and last element structures are adjusted so that each begins or ends on a nodal point. As the nodal points for the basis functions at the boundary element are adjusted to include the boundary point, as shown in Figure (4), the basis polynomials generated by these nodal points are different than the ones on the interior elements, and, therefore scheme coefficients are re-derived to complete the finite difference method. In addition, the order of basis

functions will be lowered for stability of the scheme [22]. The boundary closures for $p = 4$, below, are with one order lower, $p = 3$. A 4^{th} order scheme that is closed with 3^{rd} order will be referred to as $p = 3 - 4 - 3$. The adjustment of element length with the lower order closure is also shown in Figure (4).

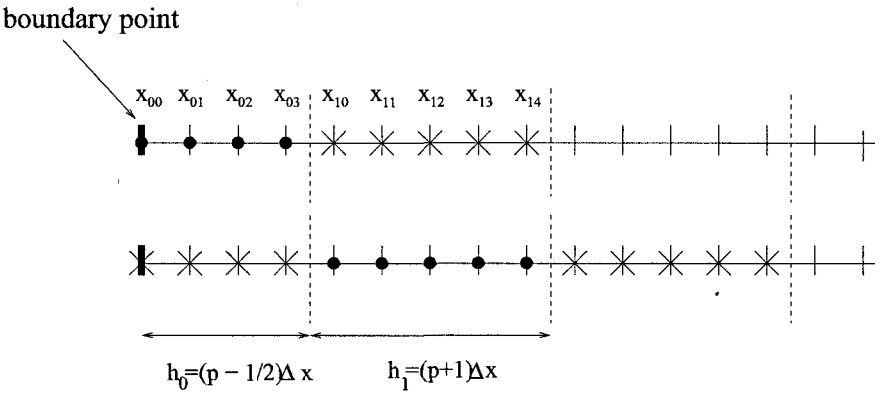

FIG. 4: Schematic of grids at the boundary, showing adjustment of element sizes. $p = 4$

Here are the general boundary closures, for any θ, for the first and last two elements.

For the first element:

$$\frac{\partial}{\partial x}\begin{bmatrix} u_{00} \\ u_{01} \\ u_{02} \\ u_{03} \end{bmatrix} = \frac{2}{h_0}\left((1+\theta\frac{|a|}{a})\bar{\mathbf{M}}^{\alpha}_{10} + \bar{\mathbf{M}}^{\alpha}_{20} + \theta\frac{|a|}{a}\bar{\mathbf{N}}^{\alpha}_{0}\right)\begin{bmatrix} u_{00} \\ u_{01} \\ u_{02} \\ u_{03} \end{bmatrix} + \frac{2}{h_0}\left(1-\theta\frac{|a|}{a}\right)\bar{\mathbf{M}}^{\alpha}_{+}\begin{bmatrix} u_{10} \\ u_{11} \\ u_{12} \\ u_{13} \\ u_{14} \end{bmatrix} \tag{29}$$

$$\bar{\mathbf{M}}^{\alpha}_{10} = \begin{bmatrix} -4 & 0 & 0 & 0 \\ -\frac{24}{49} & 0 & 0 & 0 \\ \frac{4}{49} & 0 & 0 & 0 \\ -\frac{16}{49} & 0 & 0 & 0 \end{bmatrix}, \bar{\mathbf{M}}^{\alpha}_{20} = \begin{bmatrix} \frac{23}{48} & \frac{105}{16} & \frac{-77}{16} & \frac{133}{48} \\ -\frac{2209}{2352} & \frac{-23}{16} & \frac{43}{16} & \frac{-59}{48} \\ \frac{59}{2352} & \frac{-109}{112} & \frac{-47}{112} & \frac{631}{336} \\ \frac{11}{2352} & \frac{171}{112} & \frac{-383}{112} & \frac{463}{336} \end{bmatrix}$$

$$\bar{\mathbf{N}}_0^{\alpha} = \begin{bmatrix} \frac{69}{16} & -\frac{21}{16} & \frac{35}{16} & -\frac{35}{16} \\ -\frac{489}{784} & \frac{9}{16} & -\frac{15}{16} & \frac{15}{16} \\ \frac{81}{784} & -\frac{87}{112} & \frac{145}{112} & -\frac{145}{112} \\ -\frac{51}{784} & \frac{123}{112} & -\frac{205}{112} & \frac{205}{112} \end{bmatrix}$$

$$\bar{\mathbf{M}}_+^{\alpha} = \begin{bmatrix} -\frac{315}{128} & \frac{105}{32} & \frac{-189}{64} & \frac{45}{32} & \frac{-35}{128} \\ \frac{135}{128} & \frac{-45}{32} & \frac{81}{64} & \frac{-135}{224} & \frac{15}{128} \\ -\frac{1305}{896} & \frac{435}{224} & -\frac{783}{448} & \frac{1305}{1568} & -\frac{145}{896} \\ \frac{1845}{896} & -\frac{615}{224} & \frac{1107}{448} & -\frac{1845}{1568} & \frac{205}{896} \end{bmatrix}$$

For the second element:

$$\frac{\partial}{\partial x}\begin{bmatrix} u_{10} \\ u_{11} \\ u_{12} \\ u_{13} \\ u_{14} \end{bmatrix} = \frac{2}{h_1}\left(1+\theta\frac{|a|}{a}\right)\bar{\mathbf{M}}_-^{\beta}\begin{bmatrix} u_{00} \\ u_{01} \\ u_{02} \\ u_{03} \end{bmatrix} + \frac{2}{h_1}\left(\bar{\mathbf{M}}_0^{\beta}+\theta\frac{|a|}{a}\bar{\mathbf{N}}_0^{\beta}\right)\begin{bmatrix} u_{10} \\ u_{11} \\ u_{12} \\ u_{13} \\ u_{14} \end{bmatrix}$$

$$+\frac{2}{h_1}\left(1-\theta\frac{|a|}{a}\right)\bar{\mathbf{M}}_+^{\beta}\begin{bmatrix} u_{20} \\ u_{21} \\ u_{22} \\ u_{23} \\ u_{24} \end{bmatrix} \tag{30}$$

$$\bar{\mathbf{M}}_-^{\beta} = \begin{bmatrix} \frac{4163}{6400} & -\frac{87423}{32000} & \frac{29141}{6400} & -\frac{29141}{6400} \\ -\frac{3197}{6400} & \frac{67137}{32000} & -\frac{22379}{6400} & \frac{22379}{6400} \\ \frac{75}{256} & -\frac{315}{256} & \frac{525}{256} & -\frac{525}{256} \\ \frac{563}{6400} & -\frac{11823}{32000} & \frac{3941}{6400} & -\frac{3941}{6400} \\ -\frac{1757}{6400} & \frac{36897}{32000} & -\frac{12299}{6400} & \frac{12299}{6400} \end{bmatrix}$$

$$\bar{\mathbf{M}}_0^\beta = \begin{bmatrix} -\frac{97037}{38400} & \frac{38191}{6400} & -\frac{5007}{1600} & \frac{8227}{19200} & \frac{9479}{12800} \\ -\frac{33669}{12800} & \frac{14153}{19200} & \frac{3117}{3200} & \frac{2149}{6400} & -\frac{13693}{38400} \\ \frac{1895}{1536} & -\frac{1955}{768} & 0 & \frac{1955}{768} & -\frac{1895}{1536} \\ \frac{13693}{38400} & -\frac{2149}{6400} & -\frac{3117}{3200} & -\frac{14153}{19200} & \frac{33669}{12800} \\ -\frac{9479}{12800} & -\frac{8227}{19200} & \frac{5007}{1600} & -\frac{38191}{6400} & \frac{97037}{38400} \end{bmatrix}$$

$$\bar{\mathbf{N}}_0^\beta = \begin{bmatrix} \frac{24997}{10240} & -\frac{7161}{2560} & \frac{227367}{128000} & -\frac{57}{2560} & -\frac{1631}{2048} \\ -\frac{19747}{10240} & \frac{6207}{2560} & -\frac{248913}{128000} & \frac{339}{512} & \frac{1309}{10240} \\ \frac{2625}{2048} & -\frac{1125}{512} & \frac{2835}{1024} & -\frac{1125}{512} & \frac{2625}{2048} \\ \frac{1309}{10240} & \frac{339}{512} & -\frac{248913}{128000} & \frac{6207}{2560} & -\frac{19747}{10240} \\ -\frac{1631}{2048} & -\frac{57}{2560} & \frac{227367}{128000} & -\frac{7161}{2560} & \frac{24997}{10240} \end{bmatrix}$$

$$\bar{\mathbf{M}}_+^\beta = \begin{bmatrix} -\frac{110691}{102400} & \frac{36897}{25600} & -\frac{332073}{256000} & \frac{15813}{25600} & -\frac{12299}{102400} \\ \frac{5469}{102400} & -\frac{11823}{25600} & \frac{106407}{256000} & -\frac{5067}{25600} & \frac{3941}{102400} \\ \frac{4725}{4096} & -\frac{1575}{1024} & \frac{2835}{2048} & -\frac{675}{1024} & \frac{525}{4096} \\ -\frac{201411}{102400} & \frac{67137}{25600} & -\frac{604233}{256000} & \frac{28773}{25600} & -\frac{22379}{102400} \\ \frac{262269}{102400} & -\frac{87423}{25600} & \frac{786807}{256000} & -\frac{37467}{25600} & \frac{29141}{102400} \end{bmatrix}$$

For the last two elements we make use of the following relationships. Define W^* for a matrix as:

$$W^* = \begin{bmatrix} -i & -h & -g \\ -f & -e & -d \\ -c & -b & -a \end{bmatrix}, \quad where \quad W = \begin{bmatrix} a & b & c \\ d & e & f \\ g & h & i \end{bmatrix} \tag{31}$$

For the $(N-1)^{st}$ element:

$$\frac{\partial}{\partial x}\begin{bmatrix} u_{(N-1)0} \\ u_{(N-1)1} \\ u_{(N-1)2} \\ u_{(N-1)3} \\ u_{(N-1)4} \end{bmatrix} = \frac{2}{h_{N-1}}\left(1+\theta\frac{|a|}{a}\right)\bar{\mathbf{M}}_-^\psi \begin{bmatrix} u_{(N-2)0} \\ u_{(N-2)1} \\ u_{(N-2)2} \\ u_{(N-2)3} \end{bmatrix} + \frac{2}{h_{N-1}}\left(\bar{\mathbf{M}}_0^\psi - \theta\frac{|a|}{a}\bar{\mathbf{N}}_0^\psi\right)\begin{bmatrix} u_{(N-1)0} \\ u_{(N-1)1} \\ u_{(N-1)2} \\ u_{(N-1)3} \\ u_{(N-1)4} \end{bmatrix}$$

$$+\frac{2}{h_{N-1}}\left(1-\theta\frac{|a|}{a}\right)\bar{\mathbf{M}}_{+}^{\psi}\begin{bmatrix} u_{N0} \\ u_{N1} \\ u_{N2} \\ u_{N3} \\ u_{N4} \end{bmatrix} \tag{32}$$

where

$$\bar{\mathbf{M}}_{-}^{\psi}=\left(\bar{\mathbf{M}}_{+}^{\beta}\right)^{*},\bar{\mathbf{M}}_{0}^{\psi}=\left(\bar{\mathbf{M}}_{0}^{\beta}\right)^{*},\bar{\mathbf{N}}_{0}^{\psi}=\left(\bar{\mathbf{N}}_{0}^{\beta}\right)^{*},\bar{\mathbf{M}}_{+}^{\psi}=\left(\bar{\mathbf{M}}_{-}^{\beta}\right)^{*}$$

and for the N^{th} element:

$$\frac{\partial}{\partial x}\begin{bmatrix} u_{N0} \\ u_{N1} \\ u_{N2} \\ u_{N3} \end{bmatrix}=$$

$$\frac{2}{h_N}\left(1+\theta\frac{|a|}{a}\right)\bar{\mathbf{M}}_{-}^{\omega}\begin{bmatrix} u_{(N-1)0} \\ u_{(N-1)1} \\ u_{(N-1)2} \\ u_{(N-1)3} \\ u_{(N-1)4} \end{bmatrix}+\frac{2}{h_N}\left((1-\theta\frac{|a|}{a})\bar{\mathbf{M}}_{10}^{\omega}+\bar{\mathbf{M}}_{20}^{\omega}-\theta\frac{|a|}{a}\bar{\mathbf{N}}_{0}^{\omega}\right)\begin{bmatrix} u_{N0} \\ u_{N1} \\ u_{N2} \\ u_{N3} \end{bmatrix} \tag{33}$$

where

$$\bar{\mathbf{M}}_{-}^{\omega}=\left(\bar{\mathbf{M}}_{+}^{\alpha}\right)^{*},\bar{\mathbf{M}}_{10}^{\omega}=\left(\bar{\mathbf{M}}_{10}^{\alpha}\right)^{*},\bar{\mathbf{M}}_{20}^{\omega}=\left(\bar{\mathbf{M}}_{20}^{\alpha}\right)^{*},\bar{\mathbf{N}}_{0}^{\omega}=\left(\bar{\mathbf{N}}_{0}^{\alpha}\right)^{*}$$

Note that for $\theta \neq 1$ the derivative formulas for the grid points within the last two elements next to the boundary need to be derived. This is because, as discussed in section **III.1.2**, the change in collocation points on any element changes the basis polynomials on this element and therefore the coefficients. As both the first and second elements need data from the first element to compute the derivative on the first, and second, elements respectively, the coefficients on the first two elements are calculated, as per the derivation given above. Likewise, those coefficients on the last two elements also need to be calculated. Two special cases are given below, the central scheme ($\theta = 0$) and the upwind scheme ($\theta = 1$).

Special case, $\theta = 0$, central scheme

The boundary difference formula for the central scheme are

$$\frac{\partial}{\partial x}\begin{bmatrix} u_{00} \\ u_{01} \\ u_{02} \\ u_{03} \end{bmatrix} = \mathbf{B}' \begin{bmatrix} u_{00} \\ u_{01} \\ u_{02} \\ u_{03} \end{bmatrix} + \mathbf{C}' \begin{bmatrix} u_{10} \\ u_{11} \\ u_{12} \\ u_{13} \\ u_{14} \end{bmatrix} \tag{34}$$

$$\frac{\partial}{\partial x}\begin{bmatrix} u_{10} \\ u_{11} \\ u_{12} \\ u_{13} \\ u_{14} \end{bmatrix} = \mathbf{A}'' \begin{bmatrix} u_{00} \\ u_{01} \\ u_{02} \\ u_{03} \end{bmatrix} + \mathbf{B}'' \begin{bmatrix} u_{10} \\ u_{11} \\ u_{12} \\ u_{13} \\ u_{14} \end{bmatrix} + \mathbf{C}'' \begin{bmatrix} u_{20} \\ u_{21} \\ u_{22} \\ u_{23} \\ u_{24} \end{bmatrix} \tag{35}$$

where

$$\mathbf{B}' = \frac{2}{h_0}\left(\bar{\mathbf{M}}^{\alpha}_{10} + \bar{\mathbf{M}}^{\alpha}_{20}\right)$$

and

$$\mathbf{A}'' = \frac{2}{h_1}\,\bar{\mathbf{M}}^{\beta}_{-}, \quad \mathbf{B}'' = \frac{2}{h_1}\,\mathbf{M}^{\beta}_{0}, \quad \mathbf{C}'' = \frac{2}{h_1}\bar{\mathbf{M}}^{\beta}_{+}$$

The derivative formulas for grid points at the right boundary can be obtained using above relationships, or, for this special case of $\theta = 0$ can be calculated from the first two elements using anti-symmetry, or W^* relationship, (31), in the coefficients.

Special Case, $\theta = 1$, upwind scheme

For the upwind scheme ($\theta = 1$ and $a > 0$), the derivative formula for the grid points within the boundary elements E_0, E_1 and E_N need to be defined. At the left boundary, for elements E_0 and E_1, we have,

$$\frac{\partial}{\partial x}\begin{bmatrix} u_{00} \\ u_{01} \\ u_{02} \\ u_{03} \end{bmatrix} = \mathbf{B}''' \begin{bmatrix} u_{00} \\ u_{01} \\ u_{02} \\ u_{03} \end{bmatrix} \tag{36}$$

$$\frac{\partial}{\partial x}\begin{bmatrix} u_{10} \\ u_{11} \\ u_{12} \\ u_{13} \\ u_{14} \end{bmatrix} = \mathbf{A}^{IV}\begin{bmatrix} u_{00} \\ u_{01} \\ u_{02} \\ u_{03} \end{bmatrix} + \mathbf{B}^{IV}\begin{bmatrix} u_{10} \\ u_{11} \\ u_{12} \\ u_{13} \\ u_{14} \end{bmatrix} \tag{37}$$

where

$$B''' = \frac{2}{h_0}\left(\left(2\bar{\mathbf{M}}_{10}^{\alpha} + \bar{\mathbf{M}}_{20}^{\alpha}\right) + \bar{\mathbf{N}}_{0}^{\alpha}\right)$$

$$\mathbf{A}^{IV} = \frac{4}{h_1}\bar{\mathbf{M}}_{-}^{\beta}, \quad \mathbf{B}^{IV} = \frac{2}{h_1}\left(\bar{\mathbf{M}}_{0}^{\beta} + \bar{\mathbf{N}}_{0}^{\beta}\right)$$

For the grid points within the last element at the right boundary, E_N, the derivative formula in the upwind scheme will be

$$\frac{\partial}{\partial x}\begin{bmatrix} u_{N0} \\ u_{N1} \\ u_{N2} \\ u_{N3} \end{bmatrix} = \mathbf{A}^{V}\begin{bmatrix} u_{(N-1)0} \\ u_{(N-1)1} \\ u_{(N-1)2} \\ u_{(N-1)3} \\ u_{(N-1)4} \end{bmatrix} + \mathbf{B}^{V}\begin{bmatrix} u_{N0} \\ u_{N1} \\ u_{N2} \\ u_{N3} \end{bmatrix} \tag{38}$$

where

$$\mathbf{A}^{V} = 2\bar{\mathbf{M}}_{-}^{\omega}, \quad \mathbf{B}^{V} = \frac{2}{h_N}\left(\bar{\mathbf{M}}_{20}^{\omega} - \bar{\mathbf{N}}_{0}^{\omega}\right)$$

III.2 STABILITY AND SUPER-ACCURACY PROPERTIES

III.2.1 Stability

To study the stability of the scheme with boundary closure, we perform an eigenvalue analysis when the scheme is applied to the wave equation

$$\frac{\partial u}{\partial t} + \frac{\partial u}{\partial x} = 0 \tag{39}$$

with a given boundary condition at the left boundary.

Let $\mathbf{u}^h$ denote the vector that contains all nodal values, including those at the boundary, then the semi-discrete equation for (39) can be written as

$$\frac{d\mathbf{u}^h}{dt} + \mathbf{D}\mathbf{u}^h = 0 \tag{40}$$

where $\mathbf{D}$ is the global differentiation matrix.

For central scheme ($\theta = 0$), the global matrix $\mathbf{D}$ will be denoted by $\mathbf{D}_0$ and can be constructed as

$$\mathbf{D}_0 = \begin{bmatrix} B' & C' & \bar{0} & \bar{0} & \cdots & \bar{0} & \bar{0} \\ A'' & B'' & C'' & \bar{0} & \cdots & \bar{0} & \bar{0} \\ \bar{0} & A & B & C & \cdots & \bar{0} & \bar{0} \\ \vdots & \ddots & \ddots & \ddots & \ddots & \vdots & \vdots \\ \bar{0} & \cdots & \bar{0} & A & B & C & \bar{0} \\ \bar{0} & \cdots & \bar{0} & \bar{0} & C''^* & B''^* & A''^* \\ \bar{0} & \cdots & \bar{0} & \bar{0} & \bar{0} & C'^* & B'^* \end{bmatrix} \tag{41}$$

where the sub-matrices are from section **III.1.3**, special case, θ=0. The sub-matrices with a superscript * are formed by anti-asymmetry, (31), as specified previously in the boundary closure section.

For the upwind scheme ($\theta = 1$ and $a > 0$), the global matrix $\mathbf{D}$, will be denoted by $\mathbf{D}_+$, and is of the form

$$\mathbf{D}_+ = \begin{bmatrix} B''' & \bar{0} & \bar{0} & \bar{0} & \cdots & \bar{0} & \bar{0} \\ A^{IV} & B^{IV} & \bar{0} & \bar{0} & \cdots & \bar{0} & \bar{0} \\ \bar{0} & A & B & \bar{0} & \cdots & \bar{0} & \bar{0} \\ \vdots & \ddots & \ddots & \ddots & \ddots & \vdots & \vdots \\ \bar{0} & \cdots & \bar{0} & A & B & \bar{0} & \bar{0} \\ \bar{0} & \cdots & \bar{0} & \bar{0} & A & B & \bar{0} \\ \bar{0} & \cdots & \bar{0} & \bar{0} & \bar{0} & A^V & B^V \end{bmatrix} \tag{42}$$

where again, the sub-matrices are from section **III.1.3** special case θ=1.

The discretization is stable if all of the eigenvalues of $\tilde{\mathbf{D}}$, where an over tilde denotes the matrix without the first row and first column, have positive real parts [10]. The eigenvalues for the third-order central scheme, fourth-order upwind scheme, with coefficients calculated as described in **III.1.1** and **III.1.3** are shown in Figures (5) for $N = 30$. However, the eigenvalues were computed for many values of N, as low as $N = 5$ and as high as $N = 200$. Stability of the eigenvalues was observed for each N chosen.

III.2.2 Super-convergence for wave propagation

The Fourier analysis on the numerical wavenumber for the difference formula (26) is expected to be similar as those for the general discontinuous Galerkin method

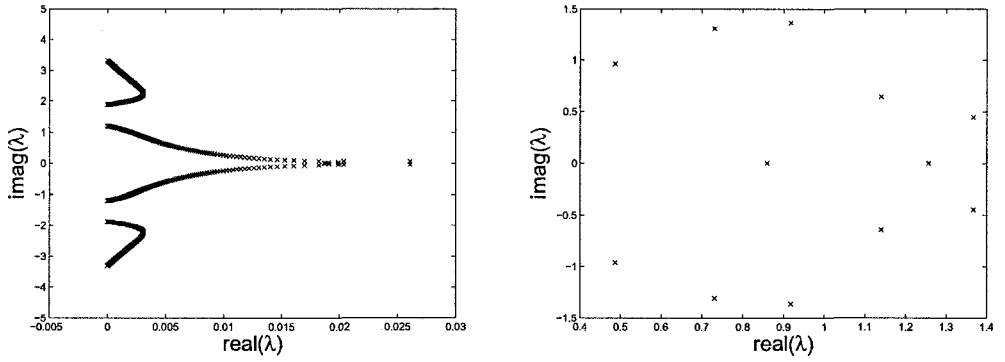

FIG. 5: Left: eigenvalue λ of cental scheme $\tilde{\mathbf{D}}_0$, $p = 3$; Right: eigenvalue λ of upwind scheme $\tilde{\mathbf{D}}_+$, $p = 4$. Eigenvalues are computed using $N = 30$ elements.

[25, 27, 3]. It has been shown that the numerical wavenumber for DGM is accurate to order $2p+1$ where p is the order of basis functions. This is often referred to as the super-convergency property of DGM and, as stated in the introduction, is a desirable property for the proposed finite difference scheme, DGM-FD.

To demonstrate the strong super-accuracy for wave propagation problems for DGM-FD, equation (39) is solved in a domain of $0 \leq x \leq 1$ with periodic boundary condition and an initial condition

$$u(x,0) = e^{-\frac{\ln(2)}{0.0481^2}\left(x-\frac{1}{2}\right)^2} \tag{43}$$

First, using the upwind scheme from **III.1.1** with periodic closure, the numerical solution is calculated , from $t = 0$ to $t = 51$. To demonstrate the super-accuracy for propagation errors, the solutions at $t = 1$ and $t = 51$ are compared and the L2 norm of the error, $||u^h(x,51) - u^h(x,1)||_2$, is shown in Figure (6) as a function of total number of grid points in the grid refine study, and tabulated in Table I. We compare $u^h(x,51)$ to $u^h(x,1)$ rather than to initial, (43), as one advective period is needed to dampen the non-physical mode of the numerical wave [27].

Convergence orders close to 5, 7 and 9 are observed even though the order of the basis function is $p = 2, 3, 4$, respectively, matching the theoretical rate of convergence for the propagation error of order $2p + 1$. See Table I and Figure (6) for data.

Next, the numerical wave number accuracy of the method, DGM-FD, is also examined and then compared to DRP and compact schemes using the following example. First, governing equation (39), is solved in a domain of $-50 \leq x \leq 450$

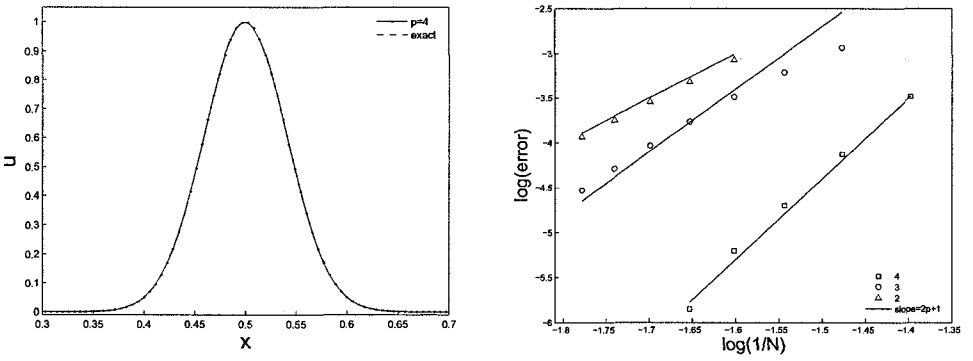

FIG. 6: Left: numerical solution at $t = 51$ in a domain of $[0, 1]$ with periodic boundary condition. Right: mesh refinement study on the L2 norm of the difference between numerical solutions at $t = 1$, $u^h(x, 1)$, and at $t = 51$, $u^h(x, 51)$. $p = 1, 2, 3, 4$ as indicated.

TABLE I: Convergence rate data $p = 2, 3, 4$ for Grid Structure I

			θ=1			
	error	*rate*	*error*	*rate*	*error*	*rate*
N		$p = 2$		$p = 3$		$p = 4$
25	——	——	——	——	3.2675E-4	——
30	——	——	1.1546E-2	——	7.4374E-5	8.1181
35	——	——	6.1181E-3	4.1199	1.9982E-5	8.5260
40	8.4202E-4	——	3.2212E-3	4.8040	6.2433E-6	8.7123
45	4.7652E-4	4.8335	1.7098E-3	5.3779	1.3989E-6	8.7984
50	2.8463E-4	4.8908	9.2492E-4	5.8315	——	——
55	1.7800E-4	4.9250	5.1363E-4	6.1708	——	——
60	1.1576E-4	4.9453	2.9398E-4	6.4133	——	——

with periodic boundary condition and initial condition

$$u(x,0) = e^{-\frac{\ln(2)}{3^2}(x)^2} \tag{44}$$

until a final time, $t_{final} = 400$.

Then, the Fast Fourier Transform (FFT) function in Matlab is used to obtain the difference, $k^* - k$, where k^* is the numerical approximation to the wave number k.

If the FFT of exact solution is $u_{exact}(k,t) = e^{-ikt}\hat{u}_0(k)$, then the FFT of numerical solution can be written in terms of numerical wavenumber k^* as $\hat{u}(k^*,t) = e^{-ik^*t}\hat{u}_0(k)$. Therefore an estimation of the difference, $k^* - k$, is

$$k^* - k = -\frac{ln[\hat{u}(k^*,t)/\hat{u}_{exact}(k,t)]}{it}. \tag{45}$$

Further details can be found in the Appendix. As noted above for convergence rates, for DGM [27], after the wave propagates for one time period, the non-physical wave mode is eliminated. To estimate the numerical wave number, the initial profile, (44), is advanced to $u^h(x,1)$ which is then compared to the numerical solution $u^h(x,401)$.

First we examine the DGM-FD scheme and study the numerical wave number accuracy for the upwind ($\theta = 1$) and central ($\theta = 0$) schemes for varying orders, p=2,3,4. Note that in Figure (7), as expected, the numerical solution becomes better resolved as the order, p, increases for the upwind scheme.

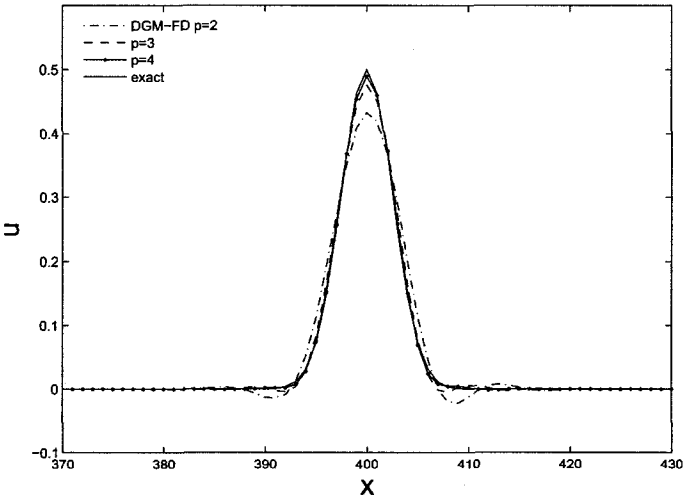

FIG. 7: DGM-FD Gaussian profile Upwind $p = 2, 3, 4$.

The numerical wave number accuracy, both for dispersion, Real($k^* - k$), and dissipation, Imag($k^* - k$) follows the same trend. See Figure (8).

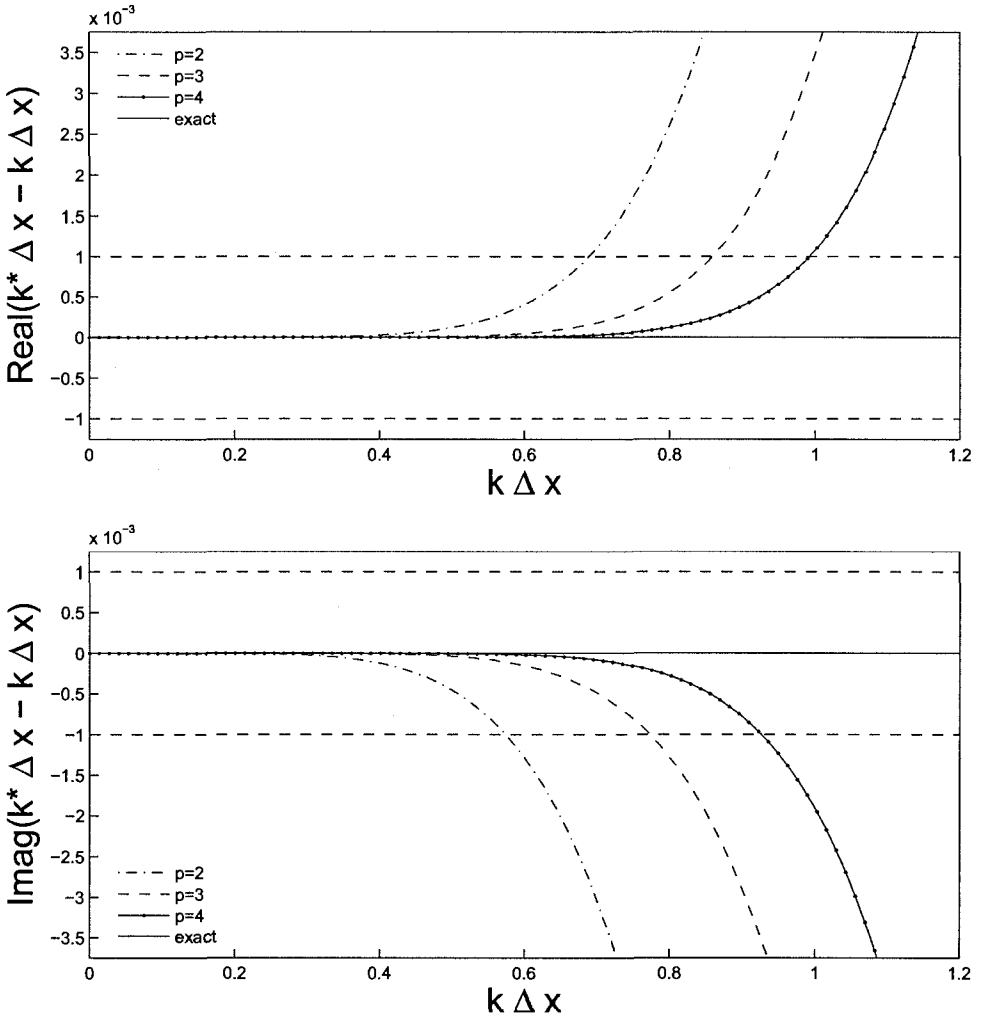

FIG. 8: DGM-FD Top: Real(k^*-k) upwind, $p = 2, 3, 4$; Bottom: Imag(k^*-k) upwind, $p = 2, 3, 4$.

Likewise for the central scheme ($\theta = 0$), we expect the numerical solution to appear more accurate as p increases. However, the $p = 3$ profile appears to have a better numerical result than that for $p = 4$. We will see this same trend with the numerical wave number plots that follow. See Figures (9) and (10).

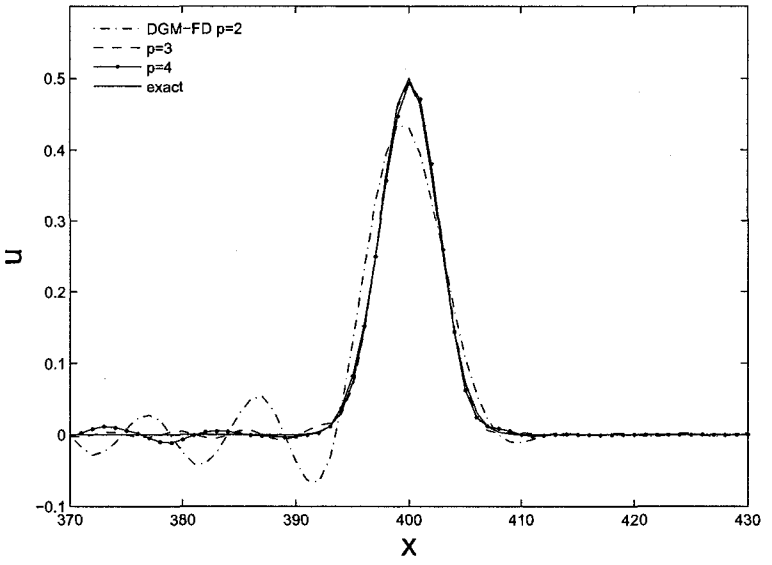

FIG. 9: Gaussian profile Central $p = 2, 3, 4$

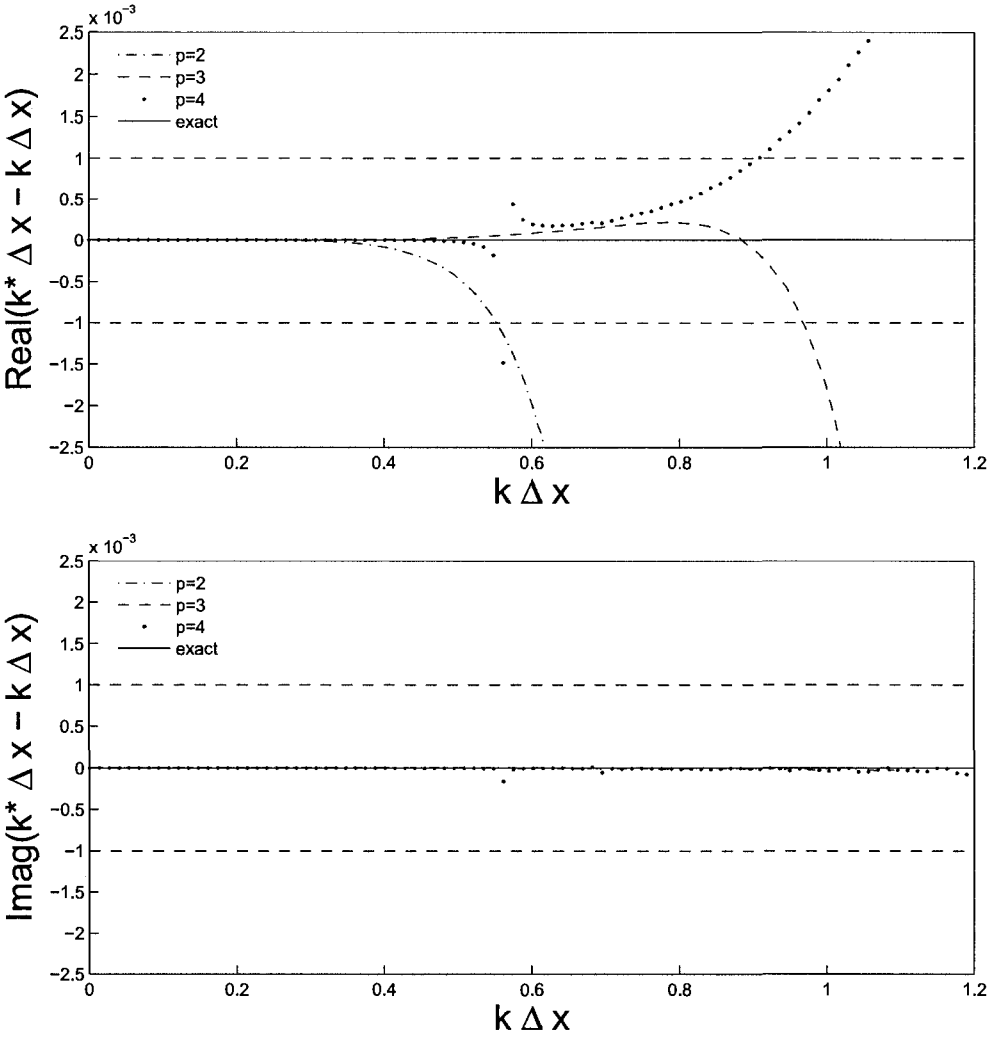

FIG. 10: Top: Real(k^*-k) central, $p = 2, 3, 4$; Bottom: Imag(k^*-k) central, $p = 2, 3, 4$.

Now we turn to comparing the performances of DGM-FD, DRP and compact schemes on the accuracy of numerical wavenumbers. First, their numerical solutions, then the numerical wave number accuracy followed by a log-log plot to show their numerical wave number convergence rates. In Figure (11), profiles for DGM-FD of p=4, 4^{th} and 6^{th} order compact and DRP are shown. DGM-FD performs similarly with 6^{th} order compact scheme and better than both 4^{th} order and DRP. In Figure (12) the dispersion properties are examined. For the given tolerance of 10^{-3}, the difference between numerical and theoretical wave numbers, $k^* - k$, is comparable for DGM-FD, 6^{th} order compact, and DRP, with $k\Delta x \leq 1$. Figure (13) shows the rate of convergence of the numerical wave number (slope in figure) for DGM-FD as higher than 4^{th}, 6^{th}, 8^{th} order compact and DRP for the given range of Real($k\Delta x$).

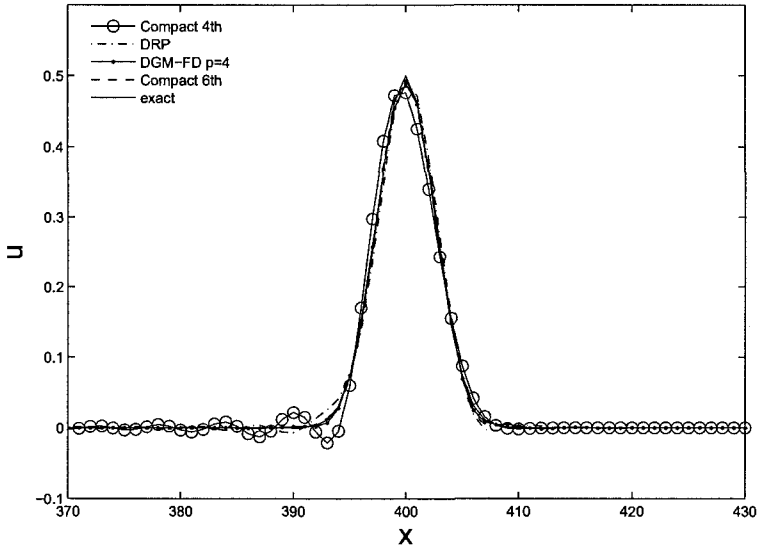

FIG. 11: Gaussian profile DGM-FD upwind $p = 4$, Compact 4^{th}, 6^{th}, DRP

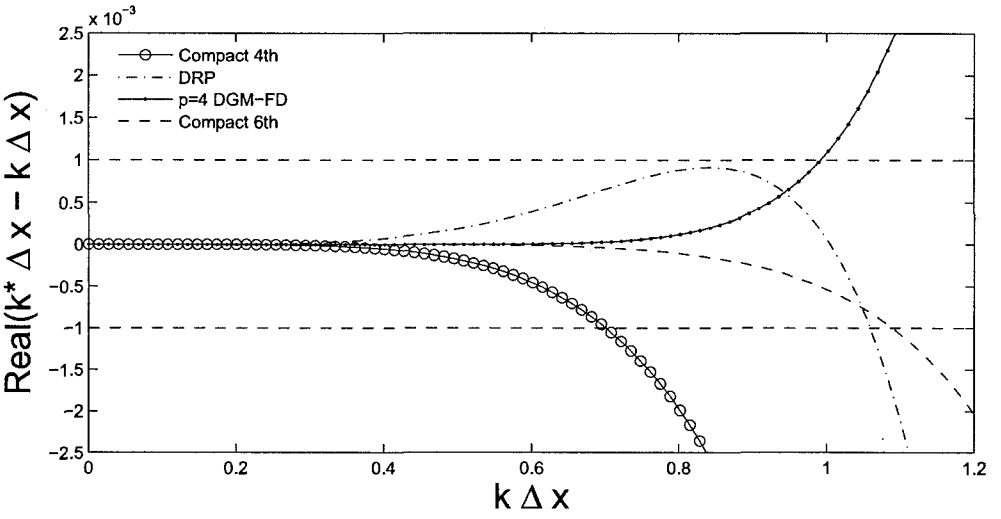

FIG. 12: Real(k*-k) Compact, DRP, DGM-FD.

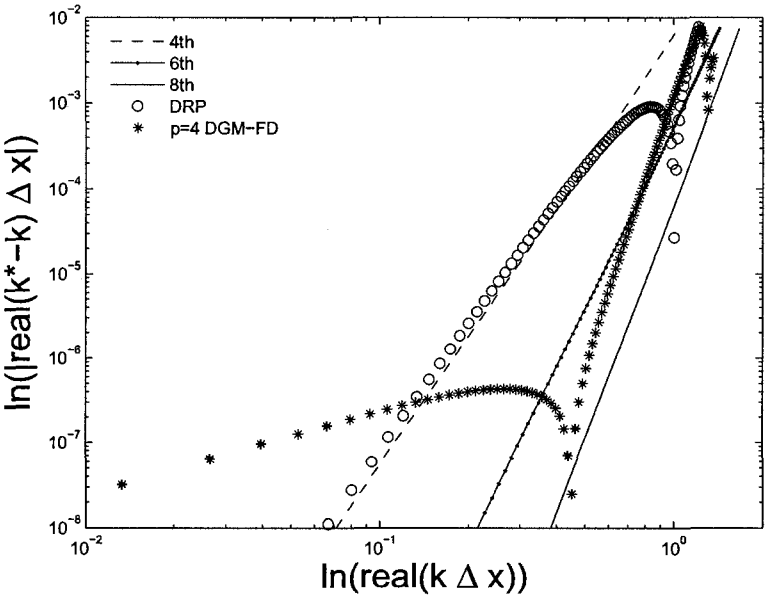

FIG. 13: loglog(Real(k*-k)) Compact, DRP, DGM-FD.

We close this section with a recommendation for upwind parameter, θ for DGM-FD. With the central scheme ($\theta = 0$), the results in Figure (10) show no dissipation. With full upwinding ($\theta = 1$) the results in Figure (8) show better dispersion properties than for the central scheme, but with more numerical dissipation. We look to balance both in Figure (14). Numerical wave number errors for $\theta = 0.50, 0.75$, and 1 are plotted with $\theta = 0.75$ recommended as the dispersion and dissipation errors are of similar magnitude.

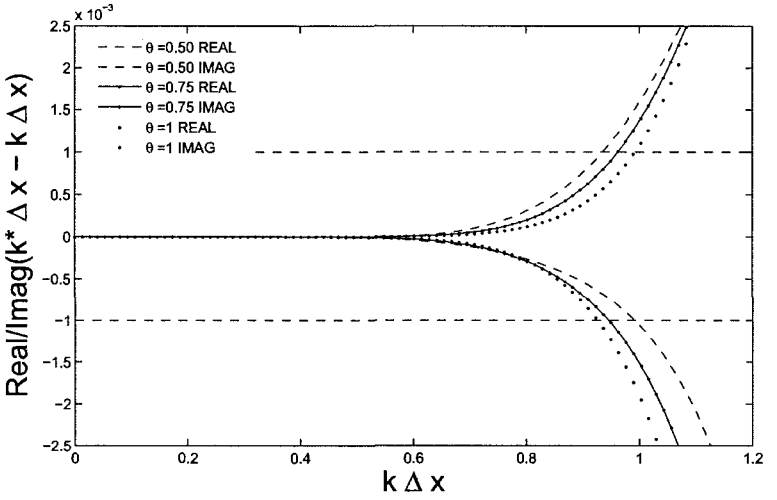

FIG. 14: Real(k*-k) and Imag(k*-k) $\theta = 0.50, 0.75, 1$.

III.3 NUMERICAL EXAMPLES

This section presents numerical examples using the DGM-FD Grid I scheme. The fourth-order upwind and third order central finite difference schemes are used. The governing equations are the linearized Euler equations

$$\frac{\partial \mathbf{U}}{\partial t} + \frac{\partial \mathbf{E}}{\partial x} + \frac{\partial \mathbf{F}}{\partial y} = 0$$

where

$$\mathbf{U} = \begin{bmatrix} \rho \\ u \\ v \\ p \end{bmatrix} \qquad \mathbf{E} = \begin{bmatrix} M_x\rho + u \\ M_x u + p \\ M_x v \\ M_x p + u \end{bmatrix} \qquad \mathbf{F} = \begin{bmatrix} M_y\rho + v \\ M_y u \\ M_y v + p \\ M_y p + v \end{bmatrix}$$

M_x and M_y are constant mean flow Mach numbers in the x and y direction, respectively. In all examples, $M_x = 0.5$, $M_y = 0$. While optimized time integration schemes like Low-Dissipation and Low-Dispersion Runge-Kutta (LDDRK) [24] are available, five stage Runge-Kutta with the traditional coefficients is used.

III.3.1 Linear Acoustic Example I

The first example is an acoustic pulse in free space. The computational domain is $[-110, 110] \times [-110, 110]$ with the PML absorbing condition applied for the ten grid points around the boundary [26]. Figure (15) shows the computational domain with variable grids. For each axis the grid starts as unrefined, with $\Delta x = 1$, then refined with a ratio of four elements per one element with $\Delta x = \frac{1}{4}$, then back to unrefined. The number of grid points per axis is 250. The initial condition is:

$$\rho(x,0) = e^{[-ln(2)(\frac{x^2+y^2}{9})]} + 0.1e^{[-ln(2)(\frac{(x-67)^2+y^2}{25})]}, \quad u(x,0) = 0.04ye^{[-ln(2)(\frac{(x-67)^2+y^2}{25})]}$$

$$v(x,0) = -0.04(x-67)e^{[-ln(2)(\frac{(x-67)^2+y^2}{25})]}, \quad p(x,0) = e^{[-ln(2)(\frac{x^2+y^2}{9})]}$$

The numerical solution is simulated until time t=1050. Density contours computed with the upwind scheme are shown in Figure (16) and a comparison with the exact solution are shown in Figures (17). For $t = 30, 60, 80, 100$, very good agreement is observed.

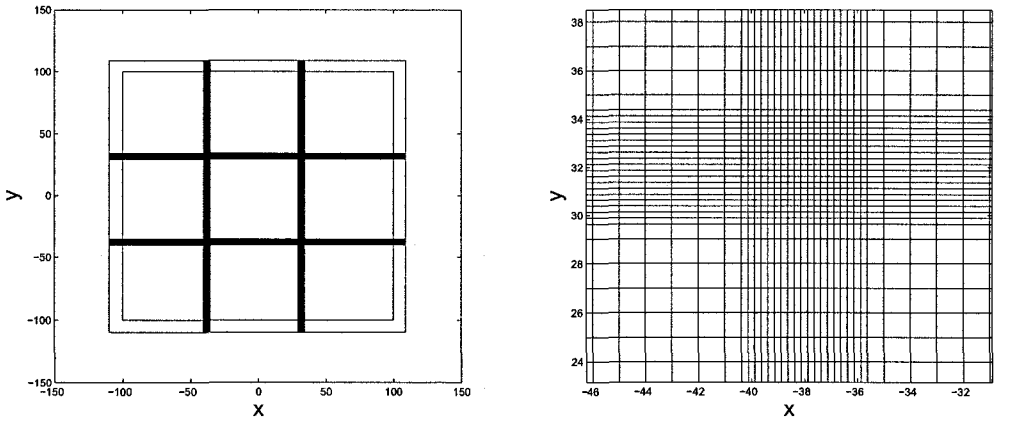

FIG. 15: Computational domain with variable grid sizes.

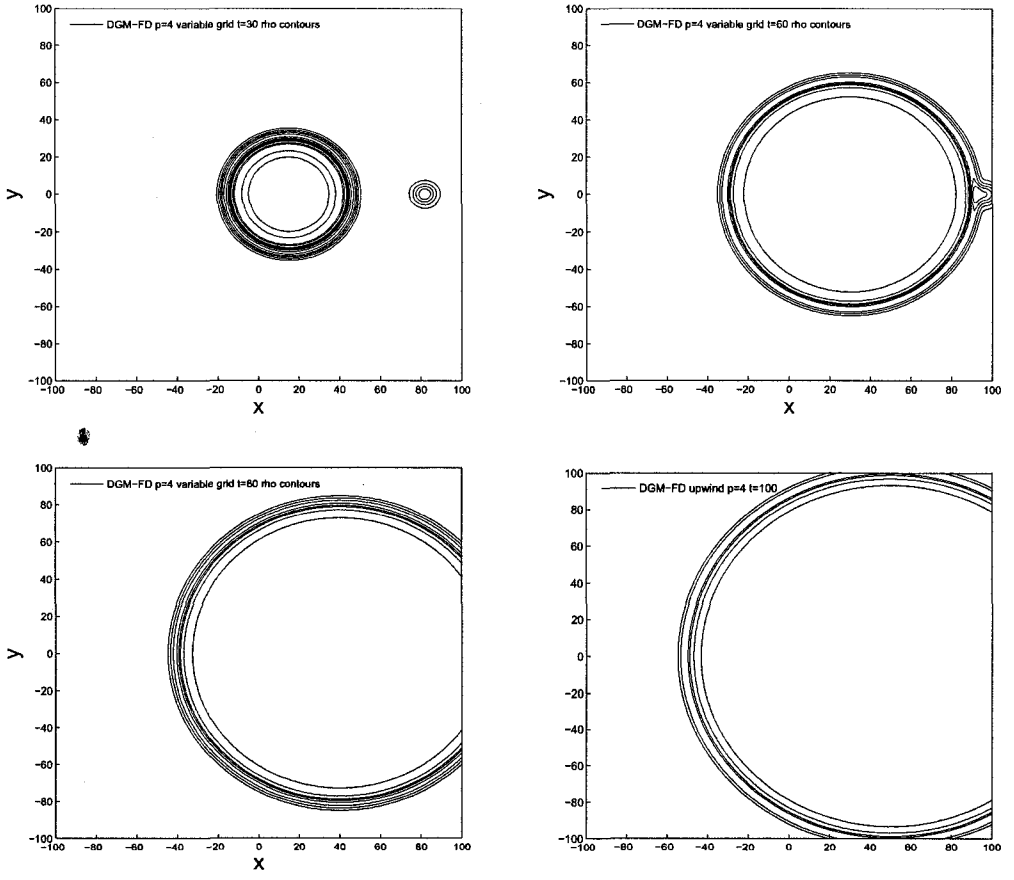

FIG. 16: Contours of density at $t = 30, 60, 80, 100$ in the physical domain for upwind, $p = 3 - 4 - 3$

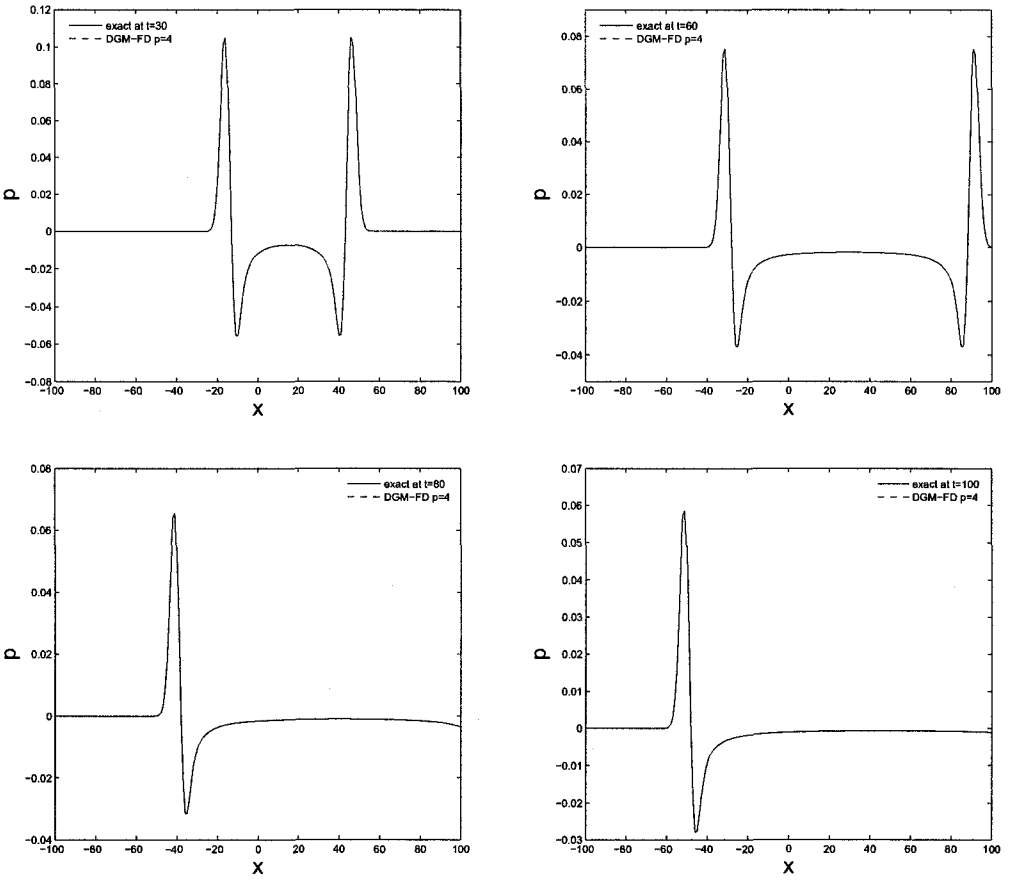

FIG. 17: Comparison of pressure with exact solution along $y = 0$ for upwind, $p = 3 - 4 - 3$

The central scheme, p=3, is a lower order than upwind $p = 4$, and as seen with numerical wave number plots, the central $p = 3$ scheme has a slightly smaller range of numerical wave number resolution, consequently the initial condition profiles are adjusted as follows:

$$\rho(x,0) = e^{[-ln(2)(\frac{x^2+y^2}{25})]} + 0.1e^{[-ln(2)(\frac{(x-67)^2+y^2}{25})]}, \quad u(x,0) = 0.04ye^{[-ln(2)(\frac{(x-67)^2+y^2}{25})]}$$

$$v(x,0) = -0.04(x-67)e^{[-ln(2)(\frac{(x-67)^2+y^2}{25})]}, \quad p(x,0) = e^{[-ln(2)(\frac{x^2+y^2}{25})]}$$

Density contours are shown in Figure (18) and a comparison with the exact solution is shown in Figure (19). Strong agreement is observed with slight noise in the central pressure profiles, which cause no instability and disappear as t increases.

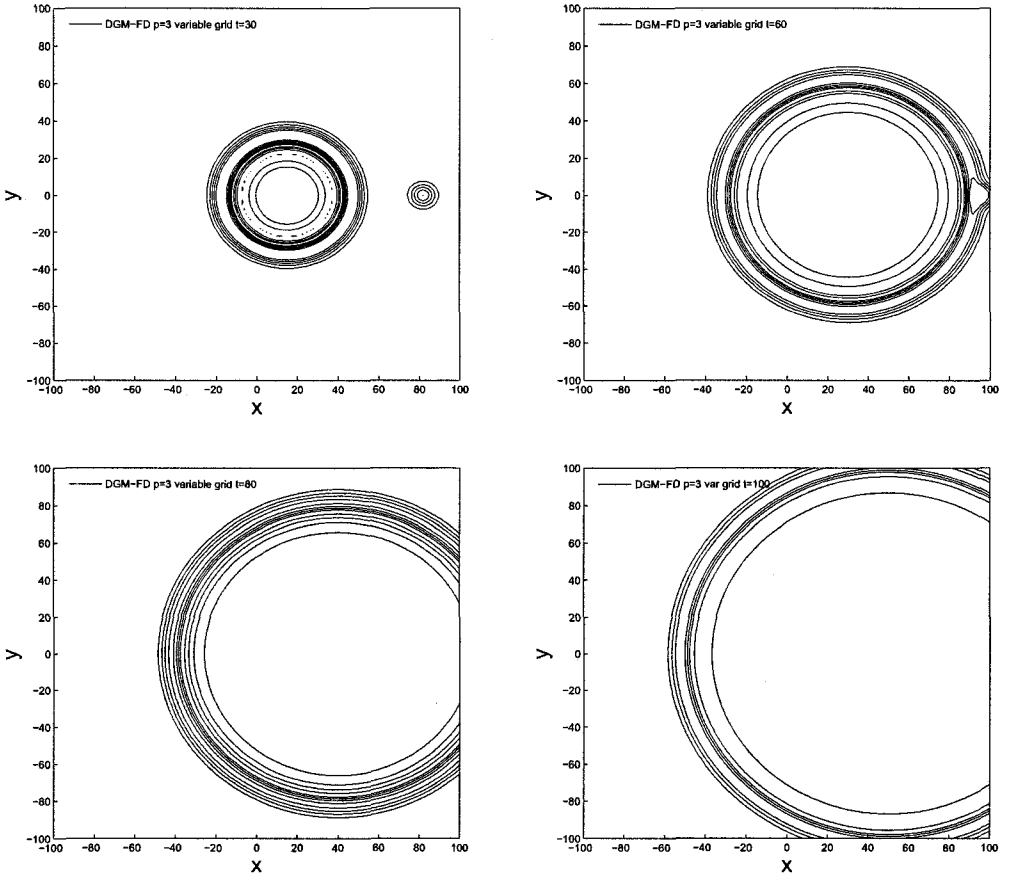

FIG. 18: Contours of density at $t = 30, 60, 80, 100$ for central, $p = 2 - 3 - 2$ with larger pulse initial condition.

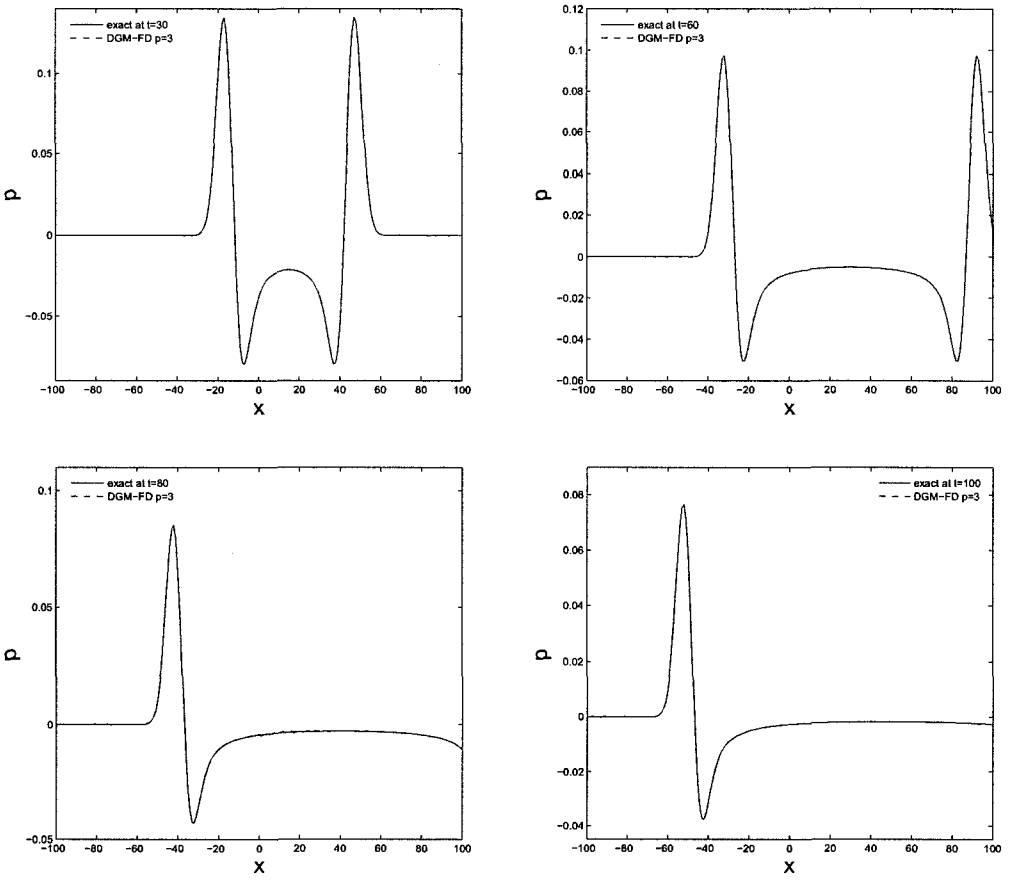

FIG. 19: Comparison of pressure with exact solution along $y = 0$ for central, $p = 2 - 3 - 2$.

III.3.2 Linear Acoustic Example II

This example is the reflection of an acoustic pulse with a wall at $y = 0$. The computational domain is $[-110, 110] \times [0, 220]$ with the PML absorbing condition applied for the ten grid points on the left and right and twenty grid points on the top boundary [26]. The initial condition is the following:

$$p(x,0) = \rho(x,0) = e^{[-ln(2)(\frac{x^2+(y-25)^2}{25})]}, u(x,0) = v(x,0) = 0$$

Density contours and a comparison with the exact solution are shown in Figures (20) and (21) for upwind scheme $p = 4$ followed by central scheme $p = 3$ in Figures (22) and (23). Very good agreement is observed for numerical results compared to the exact solution at t=30, 60, 100, and 150, see Figures (21) and (23), as well as between the two schemes in Figures (20) and (22). The numerical simulation is run to t=2000.

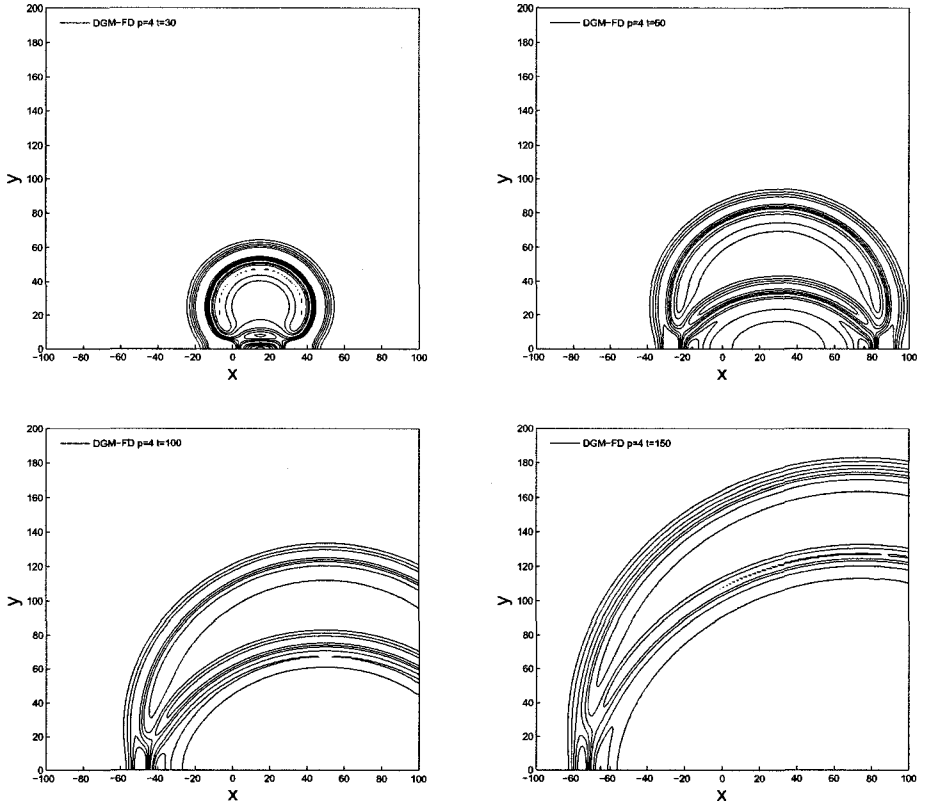

FIG. 20: Contours of density at $t = 30, 60, 100, 150$ in the physical domain for upwind, $p = 3 - 4 - 3$.

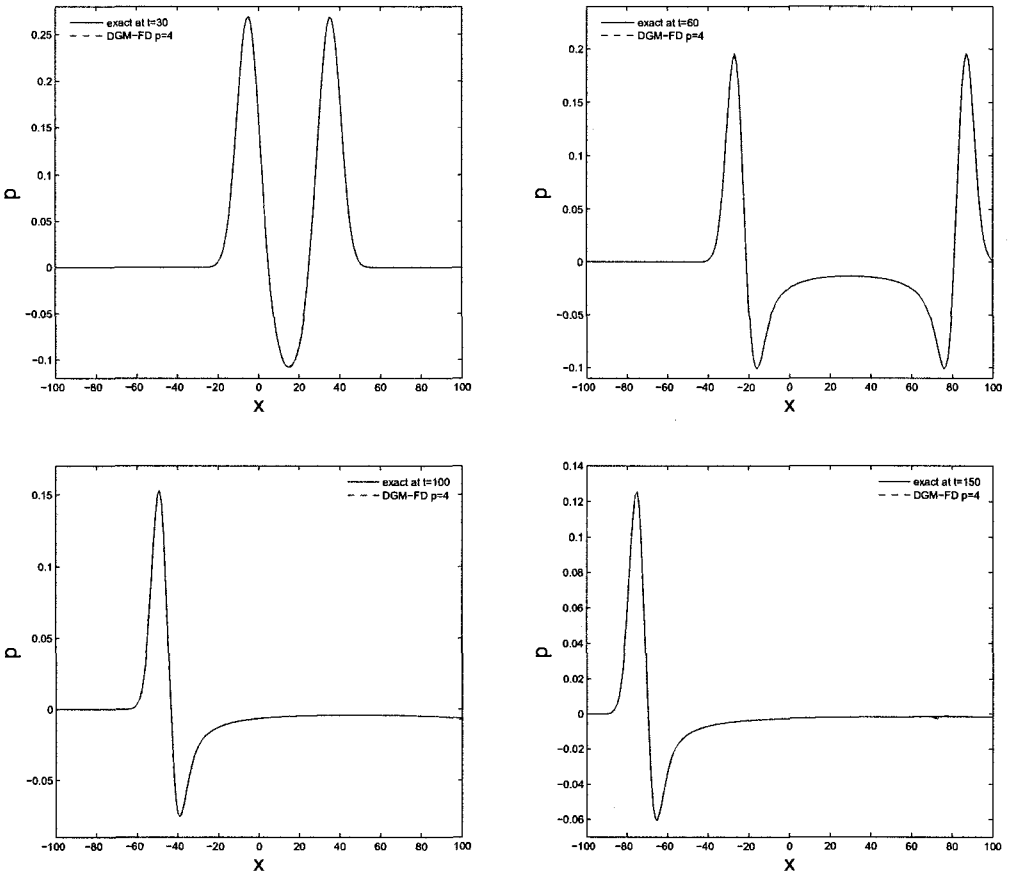

FIG. 21: Comparison of pressure with exact solution along $y = 0$ for upwind, $p = 3 - 4 - 3$.

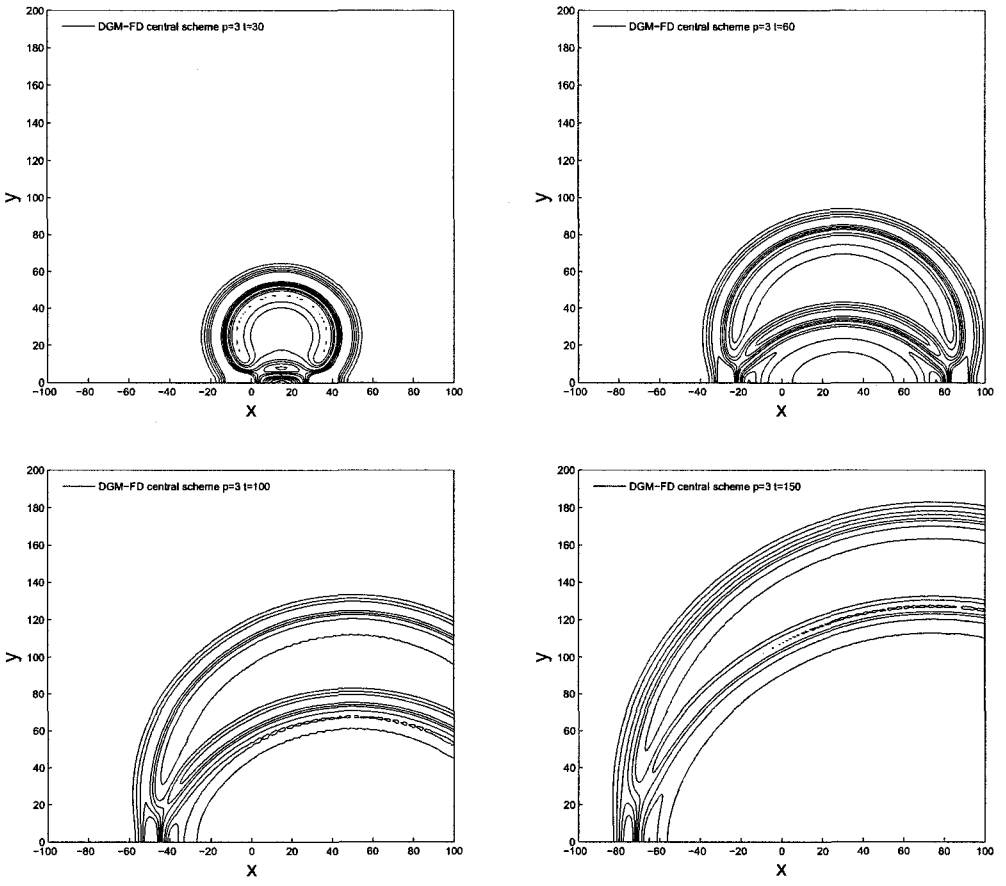

FIG. 22: Contours of density at $t = 30, 60, 100, 150$ in the physical domain for central, $p = 2 - 3 - 2$.

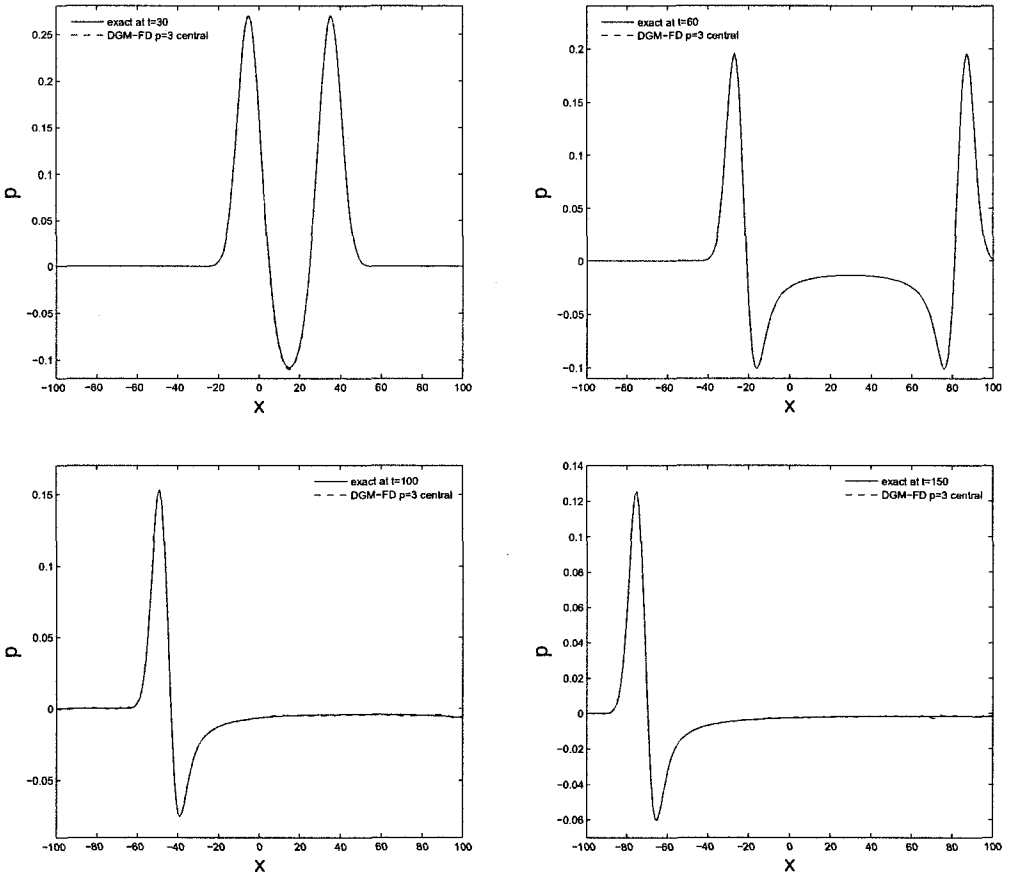

FIG. 23: Comparison of pressure with exact solution along $y = 0$ for central, $p = 2 - 3 - 2$.

Chapter IV

GRID STRUCTURE I, DGM - FLUX FINITE DIFFERENCE SCHEME

A finite difference type scheme with upwinding parameter θ was presented in the previous chapter. It is derived following the expression given in (21) with the assumption of $f = au$. In order for the scheme presented earlier to be applied to a general flux function $f(u)$, wave splitting is required. This would involve linearizing the flux, f, and then finding the eigenvalues and eigenvectors. The positive eigenvalues and their corresponding eigenvectors would be acted on by the upwind scheme, and the rest, by the downwind scheme. This approach is reasonable for linear problems, as presented in the last chapter, but for non-linear problems it is preferable to apply a flux scheme where no explicit splitting will be required. This chapter provides this general flux formulation, derived from (21), for $f(u)$.

Recall the discretization formula for the spatial derivative of $\vec{f}^n$ given in (21):

$$\frac{\partial \vec{f}^n}{\partial x} = \frac{2}{h_n}\left\{\bar{\mathbf{M}}_- \vec{f}^{n-1} + \bar{\mathbf{M}}_0 \vec{f}^n + \bar{\mathbf{M}}_+ \vec{f}^{n+1} + \theta||a||_{max}\left(\bar{\mathbf{M}}_- \vec{u}^{n-1} + \bar{\mathbf{N}}_0 \vec{u}^n - \bar{\mathbf{M}}_+ \vec{u}^{n+1}\right)\right\} \tag{46}$$

where $||a||_{max}$ is the largest eigenvalue of the jacobian of f.

In particular, if we let $\theta = 0$, we get an expression for the central derivative of $\vec{f}^n$:

$$\frac{\partial \vec{f}^n}{\partial x} = \frac{2}{h_n}\left\{\bar{\mathbf{M}}_- \vec{f}^{n-1} + \bar{\mathbf{M}}_0 \vec{f}^n + \bar{\mathbf{M}}_+ \vec{f}^{n+1}\right\} \tag{47}$$

We call the term left over in (46) the upwinding term.

$$\frac{\partial \vec{u}^n_{upw}}{\partial x} = \frac{2}{h_n}\left\{\theta||a||_{max}\left(\bar{\mathbf{M}}_- \vec{u}^{n-1} + \bar{\mathbf{N}}_0 \vec{u}^n - \bar{\mathbf{M}}_+ \vec{u}^{n+1}\right)\right\} \tag{48}$$

The upwinding term improves stability and the parameter, θ, can be any number between 0 and 1. Reasonable values of θ are 0.5, or the optimal value with respect to minimizing dissipation and dispersion errors shown before in Figure (14) to be about 0.75.

Note that if $f = au$ the derivative formulation for the flux together with the upwinding term result in the general formulation for $\frac{\partial \vec{u}^n}{\partial x}$ shown before:

$$\frac{\partial \vec{u}^n}{\partial x} = \frac{2}{h_n}\left\{(1 + \frac{\theta|a|}{a})\bar{\mathbf{M}}_- \vec{u}^{n-1} + (\bar{\mathbf{M}}_0 + \frac{\theta|a|}{a}\bar{\mathbf{N}}_0)\vec{u}^n + (1 - \frac{\theta|a|}{a})\bar{\mathbf{M}}_+ \vec{u}^{n+1}\right\} \tag{49}$$

The general flux scheme coefficients, including those for closure are now presented for the $p = 3$ case. The scheme for $p = 4$ is also recommended and its derivation is similar to what is presented next.

IV.1 FORMULATION

IV.1.1 Interior Scheme

The third-order ($p = 3$) scheme for interior points is presented. Recall that h_n is the element length and that for interior elements, $h_n{=}(p+1)\Delta x$. Then by (46), the finite difference formula for a set of four grid points is given by

$$\frac{\partial}{\partial x}\begin{bmatrix} f_{n0} \\ f_{n1} \\ f_{n2} \\ f_{n3} \end{bmatrix} = \frac{2}{h_n}\bar{\mathbf{M}}_- \begin{bmatrix} f_{(n-1)0} \\ f_{(n-1)1} \\ f_{(n-1)2} \\ f_{(n-1)3} \end{bmatrix} + \frac{2}{h_n}\bar{\mathbf{M}}_0 \begin{bmatrix} f_{n0} \\ f_{n1} \\ f_{n2} \\ f_{n3} \end{bmatrix} + \frac{2}{h_n}\bar{\mathbf{M}}_+ \begin{bmatrix} f_{(n+1)0} \\ f_{(n+1)1} \\ f_{(n+1)2} \\ f_{(n+1)3} \end{bmatrix}$$

$$+\frac{2}{h_n}\theta||a||_{max}\bar{\mathbf{M}}_- \begin{bmatrix} u_{(n-1)0} \\ u_{(n-1)1} \\ u_{(n-1)2} \\ u_{(n-1)3} \end{bmatrix} + \frac{2}{h_n}\theta\,||a||_{max}\bar{\mathbf{N}}_0 \begin{bmatrix} u_{n0} \\ u_{n1} \\ u_{n2} \\ u_{n3} \end{bmatrix} - \frac{2}{h_n}\theta\,||a||_{max}\bar{\mathbf{M}}_+ \begin{bmatrix} u_{(n+1)0} \\ u_{(n+1)1} \\ u_{(n+1)2} \\ u_{(n+1)3} \end{bmatrix} \tag{50}$$

where, using (24) and (25), it is found that

$$\bar{\mathbf{M}}_- = \begin{bmatrix} \frac{2865}{8192} & \frac{-12033}{8192} & \frac{20055}{8192} & \frac{-20055}{8192} \\ \frac{-1685}{8192} & \frac{7077}{8192} & \frac{-11795}{8192} & \frac{11795}{8192} \\ \frac{365}{8192} & \frac{-1533}{8192} & \frac{2555}{8192} & \frac{-2555}{8192} \\ \frac{615}{8192} & \frac{-2583}{8192} & \frac{4305}{8192} & \frac{-4305}{8192} \end{bmatrix}, \bar{\mathbf{M}}_0 = \begin{bmatrix} \frac{-14051}{12288} & \frac{13257}{4096} & \frac{-4119}{4096} & \frac{-2563}{12288} \\ \frac{-25337}{12288} & \frac{1035}{4096} & \frac{5831}{4096} & \frac{-5401}{12288} \\ \frac{5401}{12288} & \frac{-5931}{4096} & \frac{-1035}{4096} & \frac{25337}{12288} \\ \frac{2563}{12288} & \frac{4119}{4096} & \frac{-13257}{4096} & \frac{14051}{12288} \end{bmatrix}$$

$$\bar{\mathbf{N}}_0 = \begin{bmatrix} \frac{1215}{512} & \frac{-273}{128} & \frac{483}{512} & \frac{45}{256} \\ \frac{-95}{64} & \frac{833}{512} & \frac{-301}{256} & \frac{265}{512} \\ \frac{265}{512} & \frac{-301}{256} & \frac{833}{512} & \frac{-95}{64} \\ \frac{45}{256} & \frac{483}{512} & \frac{-273}{128} & \frac{1215}{512} \end{bmatrix}, \bar{\mathbf{M}}_+ = \begin{bmatrix} \frac{4305}{8192} & \frac{-4305}{8192} & \frac{2583}{8192} & \frac{-615}{8192} \\ \frac{2555}{8192} & \frac{-2555}{8192} & \frac{1533}{8192} & \frac{-365}{8192} \\ \frac{-11795}{8192} & \frac{11795}{8192} & \frac{-7077}{8192} & \frac{1685}{8192} \\ \frac{20055}{8192} & \frac{-20055}{8192} & \frac{12033}{8192} & \frac{-2865}{8192} \end{bmatrix}$$

IV.1.2 Non-uniform grids

As before, the same scheme is also applicable to a nonuniform grid structure provided that, the basis polynomials on each element are the same (as mentioned in the formulation section) and that between grids of spacings Δx_1 and Δx_2, there is a transitional grid of length $\frac{1}{2}(\Delta x_1 + \Delta x_2)$, i.e., the average of the two grid spacings, as shown in Figure (24). The scheme remains unchanged as the factor of $\frac{2}{h_n}$ in (50) adjusts for change in element lengths. Any element or portion of the domain can be

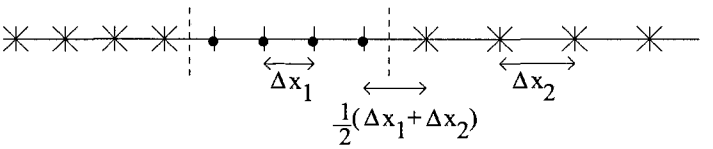

FIG. 24: Schematic of a grid structure with nonuniform grids $p = 3$.

formulated this way, including regions that contain the boundary.

IV.1.3 Boundary closures

The DGM formulation is used to derive the difference schemes for the boundary grids. As done before, the nodal points for the basis functions at the boundary element will be adjusted to include the boundary point, as shown in Figure (25). In addition, the order of basis functions is lowered to $p = 2$ for stability of the scheme [22].

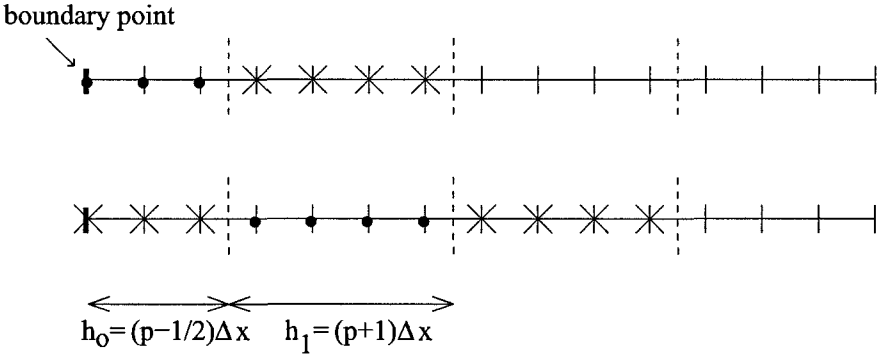

FIG. 25: Schematic of grids at the boundary, showing adjustment of element sizes. $p = 3$

Here are the general boundary closures for the first and last two elements.

For the first element:

$$\frac{\partial}{\partial x}\begin{bmatrix} f_{00} \\ f_{01} \\ f_{02} \end{bmatrix} = \frac{2}{h_0}\left(\bar{\mathbf{M}}^{\alpha}_{10} + \bar{\mathbf{M}}^{\alpha}_{20}\right)\begin{bmatrix} f_{00} \\ f_{01} \\ f_{02} \end{bmatrix} + \frac{2}{h_0}\bar{\mathbf{M}}^{\alpha}_{+}\begin{bmatrix} f_{10} \\ f_{11} \\ f_{12} \\ f_{13} \end{bmatrix}$$

$$+\frac{2}{h_0}\theta||a||_{max}\left(\bar{\mathbf{M}}^{\alpha}_{10} + \bar{\mathbf{N}}^{\alpha}_{0}\right)\begin{bmatrix} u_{00} \\ u_{01} \\ u_{02} \end{bmatrix} - \frac{2}{h_0}\theta||a||_{max}\bar{\mathbf{M}}^{\alpha}_{+}\begin{bmatrix} u_{10} \\ u_{11} \\ u_{12} \\ u_{13} \end{bmatrix} \tag{51}$$

$$\bar{\mathbf{M}}^{\alpha}_{10} = \begin{bmatrix} -\frac{9}{4} & 0 & 0 \\ \frac{3}{20} & 0 & 0 \\ \frac{3}{20} & 0 & 0 \end{bmatrix}, \bar{\mathbf{M}}^{\alpha}_{20} = \begin{bmatrix} \frac{3}{32} & \frac{55}{16} & -\frac{65}{32} \\ -\frac{97}{160} & -\frac{9}{16} & \frac{47}{32} \\ \frac{31}{160} & -\frac{25}{16} & \frac{15}{32} \end{bmatrix}$$

$$\bar{\mathbf{N}}^{\alpha}_{0} = \begin{bmatrix} \frac{81}{32} & -\frac{15}{16} & \frac{45}{32} \\ -\frac{51}{160} & \frac{9}{16} & -\frac{27}{32} \\ \frac{21}{160} & -\frac{15}{16} & \frac{45}{32} \end{bmatrix}, \bar{\mathbf{M}}^{\alpha}_{+} = \begin{bmatrix} \frac{105}{64} & -\frac{105}{64} & \frac{63}{64} & -\frac{15}{64} \\ -\frac{63}{64} & \frac{63}{64} & -\frac{189}{320} & \frac{9}{64} \\ \frac{105}{64} & -\frac{105}{64} & \frac{63}{64} & -\frac{15}{64} \end{bmatrix}$$

For the second element:

$$\frac{\partial}{\partial x}\begin{bmatrix} f_{10} \\ f_{11} \\ f_{12} \\ f_{13} \end{bmatrix} = \frac{2}{h_1}\bar{\mathbf{M}}^{\beta}_{-}\begin{bmatrix} f_{00} \\ f_{01} \\ f_{02} \end{bmatrix} + \frac{2}{h_1}\bar{\mathbf{M}}^{\beta}_{0}\begin{bmatrix} f_{10} \\ f_{11} \\ f_{12} \\ f_{13} \end{bmatrix} + \frac{2}{h_1}\bar{\mathbf{M}}^{\beta}_{+}\begin{bmatrix} f_{20} \\ f_{21} \\ f_{22} \\ f_{23} \end{bmatrix}$$

$$+\frac{2}{h_1}\theta||a||_{max}\bar{\mathbf{M}}_{-}^{\beta}\begin{bmatrix} u_{00} \\ u_{01} \\ u_{02} \end{bmatrix} + \frac{2}{h_1}\theta||a||_{max}\bar{\mathbf{N}}_{0}^{\beta}\begin{bmatrix} u_{10} \\ u_{11} \\ u_{12} \\ u_{13} \end{bmatrix} - \frac{2}{h_1}\theta\ ||a||_{max}\bar{\mathbf{M}}_{+}^{\beta}\begin{bmatrix} u_{20} \\ u_{21} \\ u_{22} \\ u_{23} \end{bmatrix} \quad (52)$$

$$\bar{\mathbf{M}}_{-}^{\beta} = \begin{bmatrix} -\frac{1719}{4096} & \frac{2865}{2048} & -\frac{8595}{4096} \\ \frac{1011}{4096} & -\frac{1685}{2048} & \frac{5055}{4096} \\ -\frac{219}{4096} & \frac{365}{2048} & -\frac{1095}{4096} \\ -\frac{369}{4096} & \frac{615}{2048} & -\frac{1845}{4096} \end{bmatrix}, \bar{\mathbf{M}}_{0}^{\beta} = \begin{bmatrix} -\frac{14051}{12288} & \frac{13257}{4096} & -\frac{4119}{4096} & -\frac{2563}{12288} \\ -\frac{25337}{12288} & \frac{1035}{4096} & \frac{5931}{4096} & -\frac{5401}{12288} \\ \frac{5401}{12288} & -\frac{5931}{4096} & -\frac{1035}{4096} & \frac{25337}{12288} \\ \frac{2563}{12288} & \frac{4119}{4096} & -\frac{13257}{4096} & \frac{14051}{12288} \end{bmatrix}$$

$$\bar{\mathbf{N}}_{0}^{\beta} = \begin{bmatrix} \frac{1215}{512} & -\frac{273}{128} & \frac{483}{512} & \frac{45}{256} \\ -\frac{95}{64} & \frac{833}{512} & -\frac{301}{256} & \frac{265}{512} \\ \frac{265}{512} & -\frac{301}{256} & \frac{833}{512} & -\frac{95}{64} \\ \frac{45}{256} & \frac{483}{512} & -\frac{273}{128} & \frac{1215}{512} \end{bmatrix}, \bar{\mathbf{M}}_{+}^{\beta} = \begin{bmatrix} \frac{4305}{8192} & -\frac{4305}{8192} & \frac{2583}{8192} & -\frac{615}{8192} \\ \frac{2555}{8192} & -\frac{2555}{8192} & \frac{1533}{8192} & -\frac{365}{8192} \\ -\frac{11795}{8192} & \frac{11795}{8192} & -\frac{7077}{8192} & \frac{1685}{8192} \\ \frac{20055}{8192} & -\frac{20055}{8192} & \frac{12033}{8192} & -\frac{2865}{8192} \end{bmatrix}$$

For the last two elements, the anti-symmetry relationship, (31) is used.

For the $(N-1)^{st}$ element:

$$\frac{\partial}{\partial x}\begin{bmatrix} f_{(N-1)0} \\ f_{(N-1)1} \\ f_{(N-1)2} \\ f_{(N-1)3} \end{bmatrix} = \frac{2}{h_{N-1}}\bar{\mathbf{M}}_{-}^{\psi}\begin{bmatrix} f_{(N-2)0} \\ f_{(N-2)1} \\ f_{(N-2)2} \end{bmatrix} + \frac{2}{h_{N-1}}\bar{\mathbf{M}}_{0}^{\psi}\begin{bmatrix} f_{(N-1)0} \\ f_{(N-1)1} \\ f_{(N-1)2} \\ f_{(N-1)3} \end{bmatrix} + \frac{2}{h_{N-1}}\bar{\mathbf{M}}_{+}^{\psi}\begin{bmatrix} f_{N0} \\ f_{N1} \\ f_{N2} \\ f_{N3} \end{bmatrix}$$

$$+\frac{2}{h_{N-1}}\theta\ ||a||_{max}\bar{\mathbf{M}}_{-}^{\psi}\begin{bmatrix} u_{(N-2)0} \\ u_{(N-2)1} \\ u_{(N-2)2} \end{bmatrix} - \frac{2}{h_{N-1}}\theta\ ||a||_{max}\bar{\mathbf{N}}_{0}^{\psi}\begin{bmatrix} u_{(N-1)0} \\ u_{(N-1)1} \\ u_{(N-1)2} \\ u_{(N-1)3} \end{bmatrix} - \frac{2}{h_{N-1}}\theta||a||_{max}\bar{\mathbf{M}}_{+}^{\psi}\begin{bmatrix} u_{N0} \\ u_{N1} \\ u_{N2} \\ u_{N3} \end{bmatrix} \quad (53)$$

where

$$\bar{\mathbf{M}}_{-}^{\psi} = \left(\bar{\mathbf{M}}_{+}^{\beta}\right)^{*}, \bar{\mathbf{M}}_{0}^{\psi} = \left(\bar{\mathbf{M}}_{0}^{\beta}\right)^{*}, \bar{\mathbf{N}}_{0}^{\psi} = \left(\bar{\mathbf{N}}_{0}^{\beta}\right)^{*}, \bar{\mathbf{M}}_{+}^{\psi} = \left(\bar{\mathbf{M}}_{-}^{\beta}\right)^{*}$$

and for the N^{th} element:

$$\frac{\partial}{\partial x}\begin{bmatrix} f_{N0} \\ f_{N1} \\ f_{N2} \end{bmatrix} = \frac{2}{h_N}\bar{\mathbf{M}}_{-}^{\omega}\begin{bmatrix} f_{(N-1)0} \\ f_{(N-1)1} \\ f_{(N-1)2} \\ f_{(N-1)3} \end{bmatrix} + \frac{2}{h_N}\left(\bar{\mathbf{M}}_{10}^{\omega} + \bar{\mathbf{M}}_{20}^{\omega}\right)\begin{bmatrix} f_{N0} \\ f_{N1} \\ f_{N2} \end{bmatrix}$$

$$+\frac{2}{h_N}\theta||a||_{max}\bar{\mathbf{M}}_{-}^{\omega}\begin{bmatrix} u_{(N-1)0} \\ u_{(N-1)1} \\ u_{(N-1)2} \\ u_{(N-1)3} \end{bmatrix} - \frac{2}{h_N}\theta||a||_{max}\left(\bar{\mathbf{N}}_{0}^{\omega} + \bar{\mathbf{M}}_{10}^{\omega}\right)\begin{bmatrix} u_{N0} \\ u_{N1} \\ u_{N2} \end{bmatrix} \tag{54}$$

where

$$\bar{\mathbf{M}}_{-}^{\omega} = \left(\bar{\mathbf{M}}_{+}^{\alpha}\right)^{*}, \bar{\mathbf{M}}_{10}^{\omega} = \left(\bar{\mathbf{M}}_{10}^{\alpha}\right)^{*}, \bar{\mathbf{M}}_{20}^{\omega} = \left(\bar{\mathbf{M}}_{20}^{\alpha}\right)^{*}, \bar{\mathbf{N}}_{0}^{\omega} = \left(\bar{\mathbf{N}}_{0}^{\alpha}\right)^{*}$$

IV.2 APPLICATION EXAMPLES

In this section the flux scheme is applied to two non-linear examples. The third-order flux finite difference scheme developed in this section is used for both examples.

IV.2.1 Burger's Equation

The first example is Burger's Equation. The governing equation is:

$$\frac{\partial u}{\partial t} + \frac{1}{2}\frac{\partial(u^2)}{\partial x} = \nu\frac{\partial^2 u}{\partial x^2}$$

where ν is taken to be 0.02.

The computational domain is $x \in [0, 430]$ with boundary and initial conditions given below. As the wave front changes rapidly over a small region in the domain, the grid size changes where Δx is 0.2 in the coarse part of the grid and 0.02 in the refined portion [38]. The initial and boundary conditions are:

$$IC: \quad u(x,0) = 1 - tanh(\frac{x - x_c}{2\nu}), \quad x_c = 5$$

$$BC: \quad u(0,t) = 2, \quad u(\infty,t) = 0$$

with exact solution:

$$u(x,t) = 1 - tanh(\frac{x - x_c - t}{2\nu})$$

Here the flux, $f = \frac{1}{2}u^2$, and the value of θ is taken to be 1 for the scheme given in (50). The second derivative was evaluated using (D+)(D-) where D+ is the upwind scheme from section **III.1** with $\theta = 1$ and $a = 1$ and D- the corresponding downwind scheme.

Time integration is five stage Runge-Kutta where dt is 0.025 times the smallest dx, 0.02 or $dt = 0.0006250$.

Figure (26) shows the numerical and exact solution at $t = 30$ as well as the computational domain with a variable grid that is more refined in the area supporting the wave front (see figure (27) for initial condition and grid plots). Note the close up of the numerical solution and the good agreement between the numerical and exact solutions.

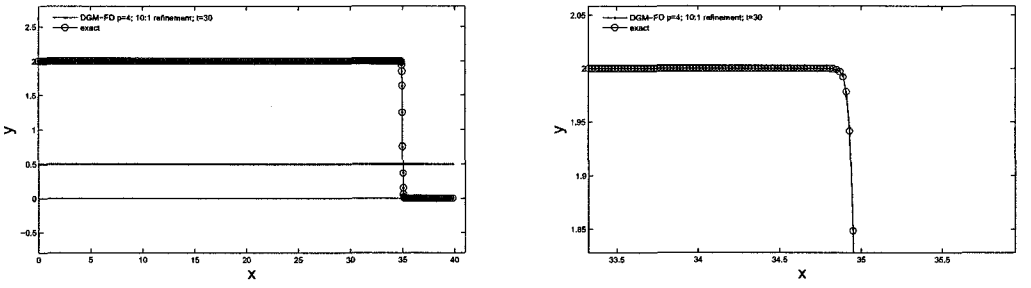

FIG. 26: left: plot of exact and numerical solution at t=30; right: zoom at t=30 of exact and numerical solution.

In order to verify the accuracy and stability over a longer time period, with t_{final} 420, a moving frame is used. For the adaptive grid, the code checks to see if the wave front is moving too far away from the center of the refined region and then, if so, refines a unit on the right of the region while coarsening a unit on the left. As the wave front is still well within the refined region, this results in refining an area of the solution that is constant, through interpolation, and coarsening an area that is also constant, through interpolation. In this way the adaptive grid is dynamic.

The shape of the numerical solution is the same as the exact solution from 0 to 420 and the numerical solution is stable as shown in Figures (27), (29). Again note the strong agreement between numerical and exact solutions.

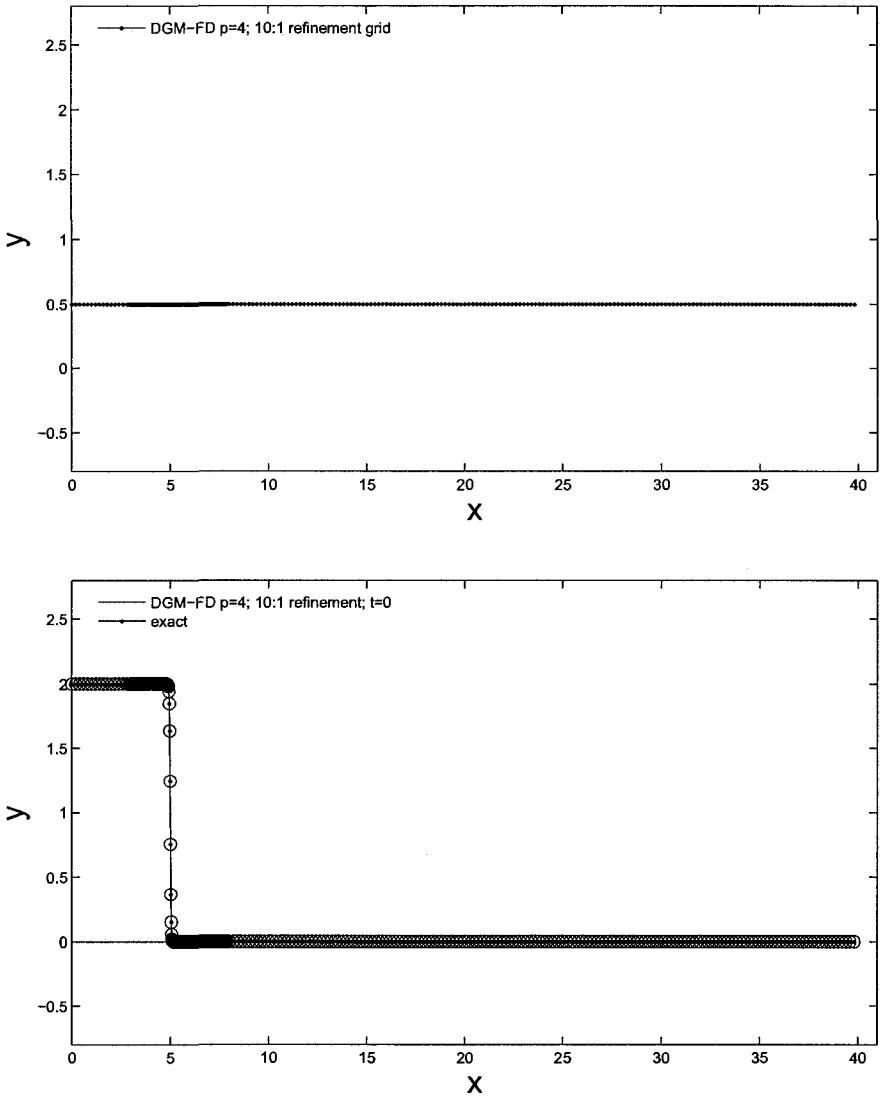

FIG. 27: Top: variable grid with 10:1 refinement, t=0; Bottom: Burger's Equation t=0

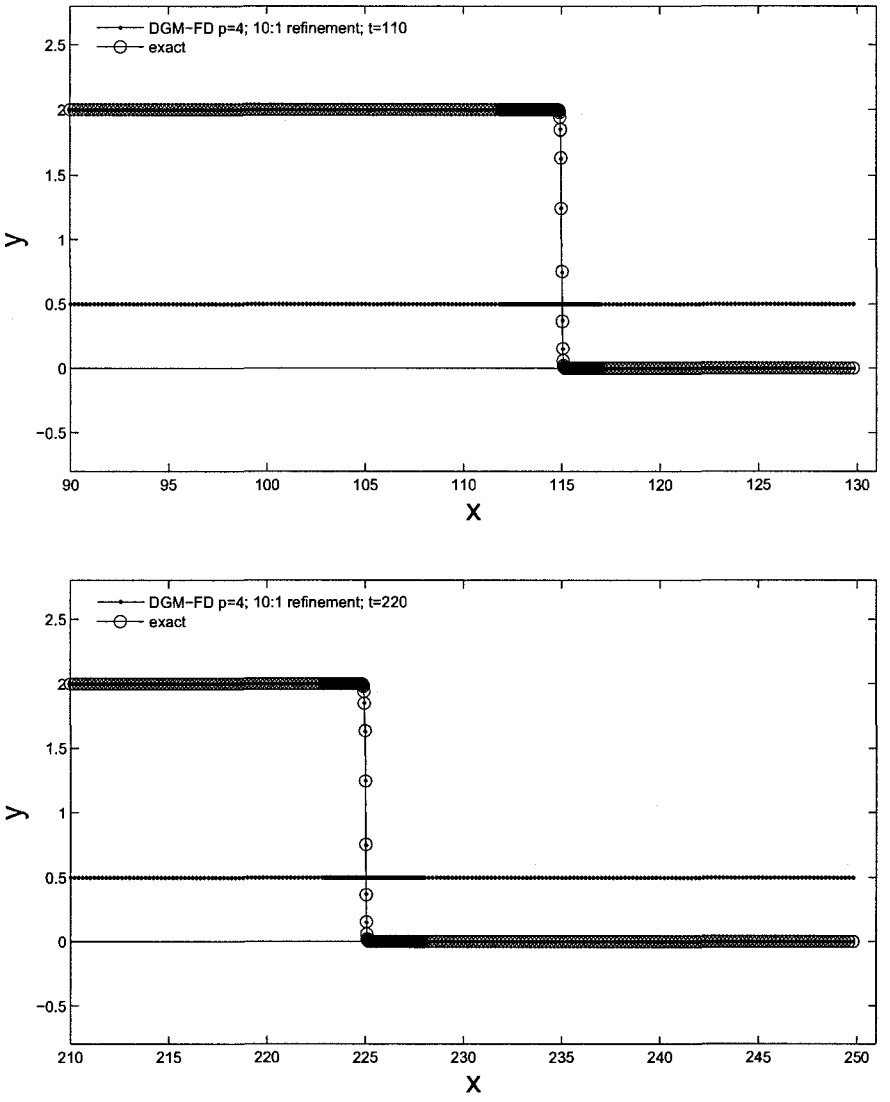

FIG. 28: Top: Burger's Equation t=110.0; Bottom: Burger's Equation t=220.0 with moving frame, dynamic grid

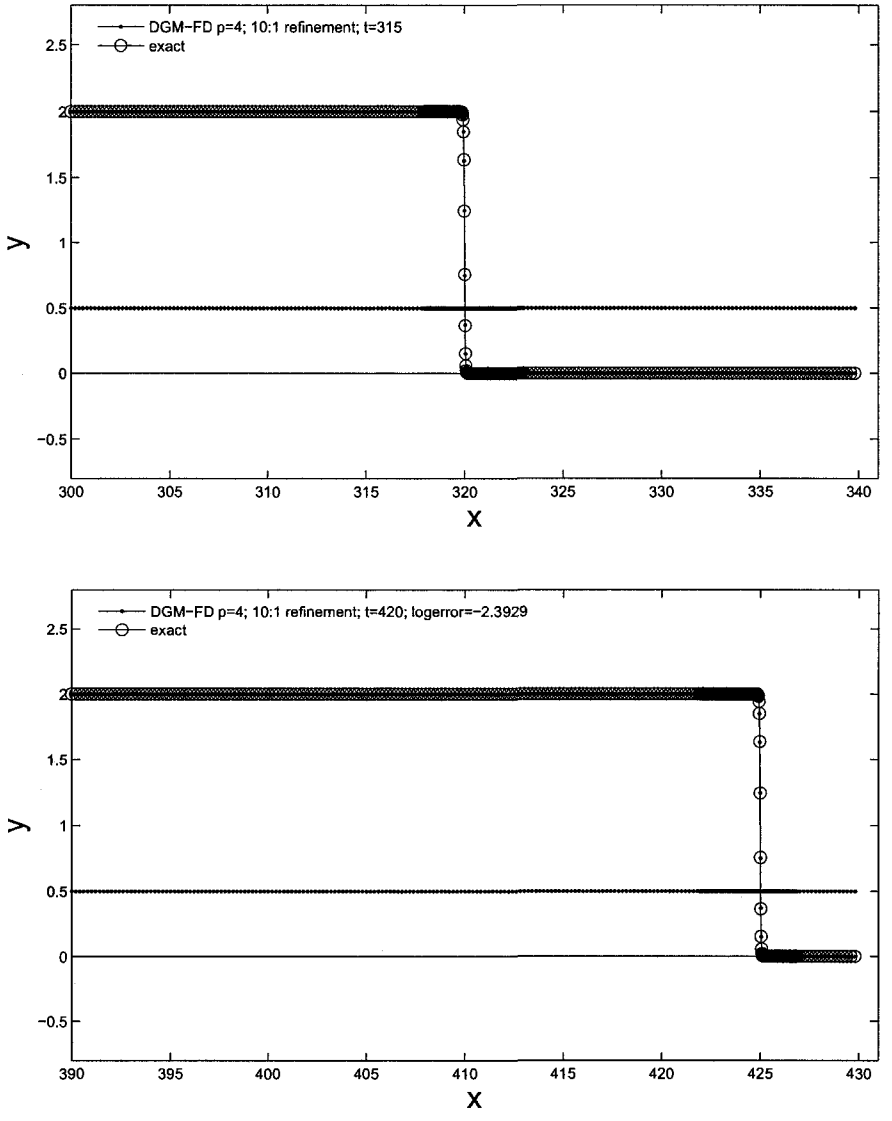

FIG. 29: Top: Burger's Equation t=315; Bottom: Burger's Equation t=420.0 with moving frame, dynamic grid

IV.2.2 Flat-plate Boundary Layer Problem

This example involves the computation of a steady-state boundary layer profile formed by uniform flow over a flat plate. The governing equations are the Navier-Stokes equations [28]

$$\frac{\partial \mathbf{U}}{\partial t} + \frac{\partial \mathbf{E}}{\partial x} + \frac{\partial \mathbf{F}}{\partial y} = 0$$

where

$$\mathbf{U} = \begin{bmatrix} \rho \\ \rho u \\ \rho v \\ \rho e \end{bmatrix}$$

and flux vectors

$$\mathbf{E} = \begin{bmatrix} \rho u \\ \rho u^2 + p - \tau_{xx} \\ \rho uv - \tau_{xy} \\ (\rho e + p)u - u\tau_{xx} - v\tau_{xy} + q_x \end{bmatrix}$$

$$\mathbf{F} = \begin{bmatrix} \rho v \\ \rho uv - \tau_{xy} \\ \rho v^2 + p - \tau_{yy} \\ (\rho e + p)v - u\tau_{xy} - v\tau_{yy} + q_y \end{bmatrix}$$

with viscous stress terms written as

$$\tau_{xx} = \frac{M_x}{Re_N}\left[2\mu\frac{\partial u}{\partial x} - \lambda(\frac{\partial u}{\partial x} + \frac{\partial v}{\partial y})\right], \quad \tau_{yy} = \frac{M_x}{Re_N}\left[2\mu\frac{\partial v}{\partial y} - \lambda(\frac{\partial u}{\partial x} + \frac{\partial v}{\partial y})\right]$$

$$\lambda = \frac{2}{3}\mu, \quad \tau_{xy} = \frac{M_x}{Re_N}\mu(\frac{\partial u}{\partial y} + \frac{\partial v}{\partial x})$$

and heat transfer terms

$$q_x = -\frac{M_x}{(\gamma - 1)PrRe_N}\mu\frac{\partial T}{\partial x}, \quad q_y = -\frac{M_x}{(\gamma - 1)PrRe_N}\mu\frac{\partial T}{\partial y}$$

where viscosity, μ, non-dimensionalized by a reference value, μ_∞, is assumed to be 1. The equation of state and the energy function are

$$\gamma p = \rho T, \quad e = \frac{u^2 + v^2}{2} + \frac{p}{(\gamma - 1)\rho}$$

In the above, u and v are the velocity components in the x and y directions respectively, p is the pressure, ρ the density, and T is the temperature, the Prandtl number, Pr is 0.708 and γ the specific heats ratio. The velocity is non-dimensionalized by a reference speed of sound, a_∞, density by ρ_∞ and pressure by $\rho_\infty a_\infty^2$. The Reynolds number, Re_N, is $\rho_\infty U_\infty L_\infty / \mu_\infty$ where U_∞ is a characteristic flow velocity and L_∞, a length scale.

This application is shown for two cases, one with Reynolds number 500 and the other with 5000. A schematic of the domains for each are shown in Figures (30) and (33) respectively. The incoming flow is uniform in the direction of the x-axis with Mach number, $M{=}U_\infty/a_\infty{=}0.1$. Numerical calculation starts with an initialization of all variables in the physical domain by the uniform incoming flow:

$$\rho(x,0) = 1, \quad u(x,0) = 0.1, \quad v(x,0) = 0.0, \quad p(x,0) = \frac{1}{\gamma}, \quad \gamma = 1.4$$

For Reynolds number 500 the variable grid structure has three distinct regions with respect to the x-axis. The first for the coarser portion, then refined near the plate leading edge and coarser again away (see Figure (30), top). Here the grid spacing in the refined region is in a 2:1 ratio compared to the unrefined. Likewise, with respect to the y-axis a 2:1 refinement is shown and there are two regions (Figure (30), bottom). Close-up views of the grids are given in Figure (31).

Extrapolation boundary conditions are used for this Reynolds number where the value at 19 points in on each of the three boundaries is extended out to the border and the dashed lines in Figure (30), top, indicate the boundary region.

Figure (32) (top) shows the contours of the u-velocity in the whole computational domain including outlines of the extrapolation boundary regions and Figure (32) (bottom) shows the normalized stream-wise velocity profile, where the stream-wise velocity is plotted as a function of a similarity variable, $y\sqrt{u_e/(\nu x)}$, with $\frac{u_e}{\nu}{=}500$, the Reynolds number, at x = 0.35, 0.50, 0.60, and 0.75. Similarity solutions are observed.

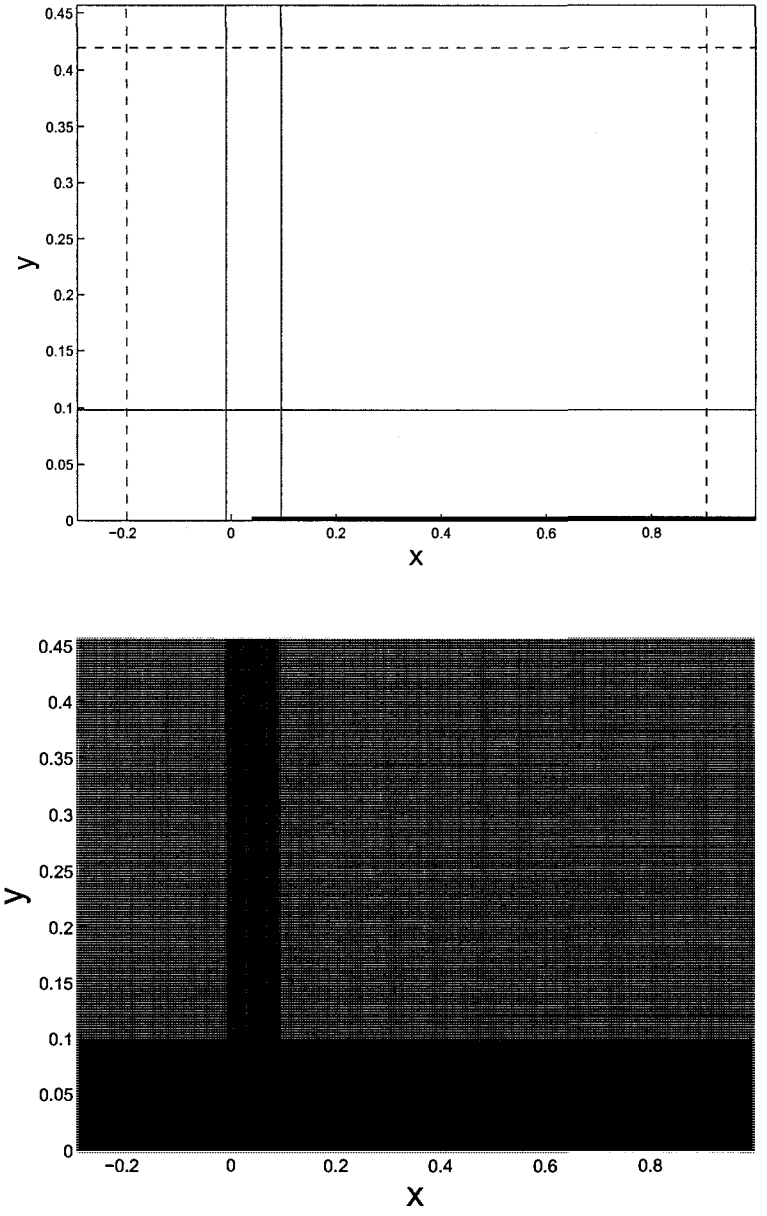

FIG. 30: Top: Schematic of domain including plate. In particular are grid lines where dx and dy change and boundary condition locations, with dashed lines for boundary region, Re_N=500; Bottom: grid is, left to right, dx=.0052, .0026, .0052 and, bottom to top, dy=.0010, .0021

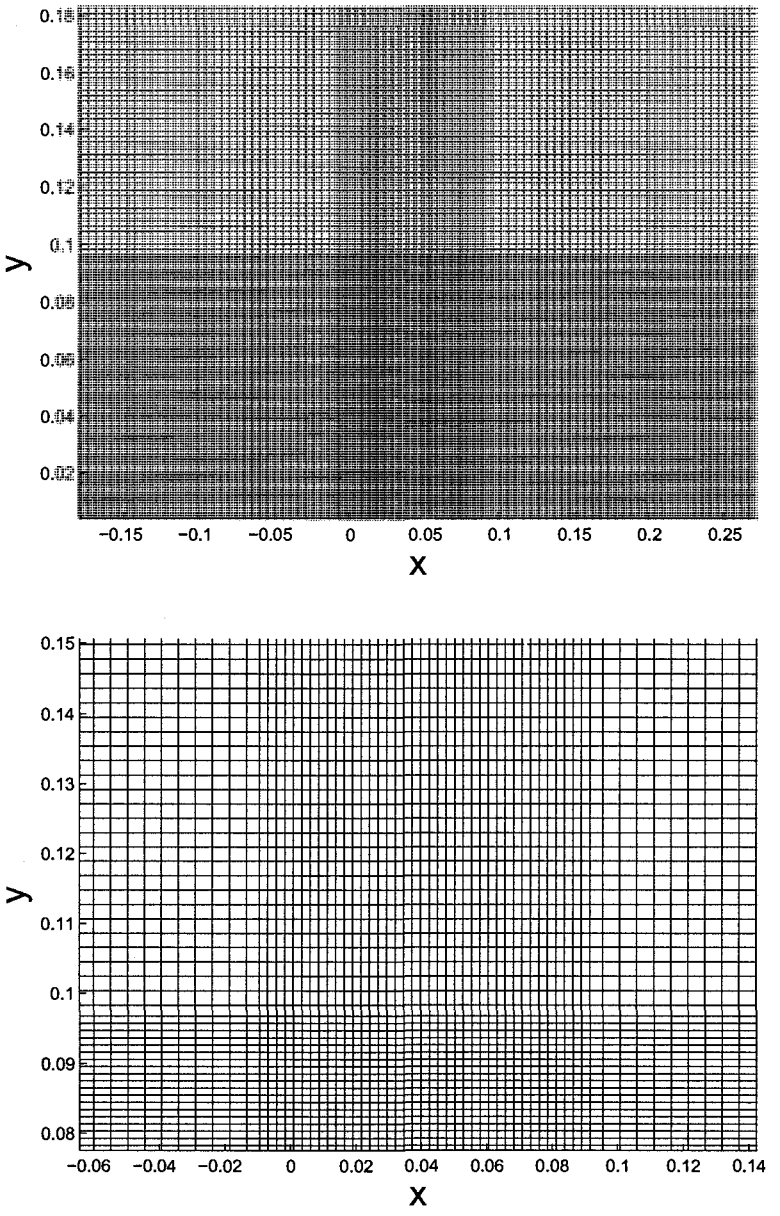

FIG. 31: Top and Bottom: closer looks at grid refinements and transition grid points, Re_N=500

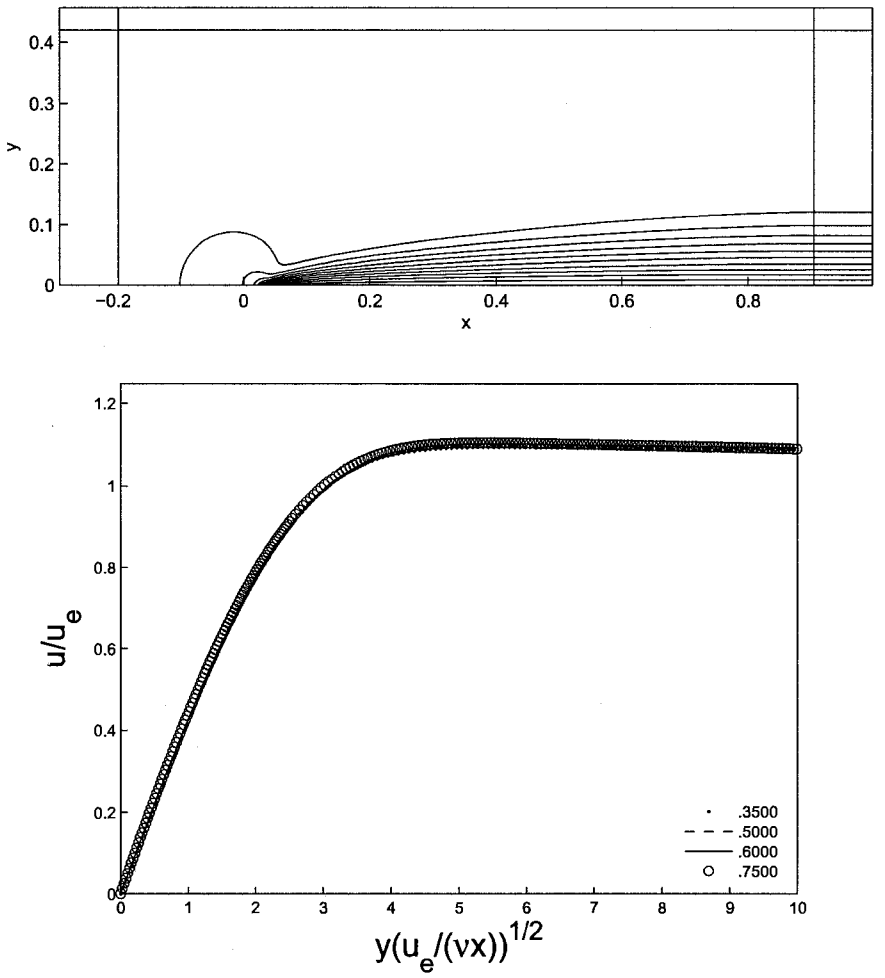

FIG. 32: Top: Boundary layer stream-wise velocity Re_N=500 t=20.00 with solid lines indicating boundary regions.; Bottom: Similarity velocity profile at selected locations, x=.35, .50, .60, .75. Horizontal variable is $y(u_e/(\nu x))^{1/2}$ and u_e is the exterior stream-wise velocity, 0.1.

The higher Reynolds number, 5000, required the variable grid structure to have three distinct regions with respect to the y-axis as greater refinement is needed on the region closest to the plate (see figure (33), bottom). For the y-axis the refined region starts with a 4:1 ratio then transitions to a 2:1 ratio and finally to the non-refined portion. Likewise, with respect to the x-axis a 2:1, 12:1 then 2:1 refinement is shown and there are five regions here where the third region, 12:1, includes the plate leading edge where extra refinements are necessary because of the higher Reynolds number. Figures (34) and (35) show close-up views of the refinements. For Reynolds number of 5000, PML boundary conditions of [28] are used at the three boundaries where the pseudo mean flow re-adjusts to the primitive variables after each Runge-Kutta time loop with dashed lines indicating the boundary region in Figure (33), top.

Figure (36), top, shows the contours of the u-velocity in the whole computational domain with borders of PML region and figure (36), bottom, shows the normalized stream-wise velocity profile where the stream-wise velocity is plotted as a function of a similarity variable, $y\sqrt{u_e/(\nu x)}$, with $\frac{u_e}{\nu}$=5000, the Reynolds number, at $x = 0.50$, 0.65, 0.75, and 0.90. The similarity solutions, again, show good agreement.

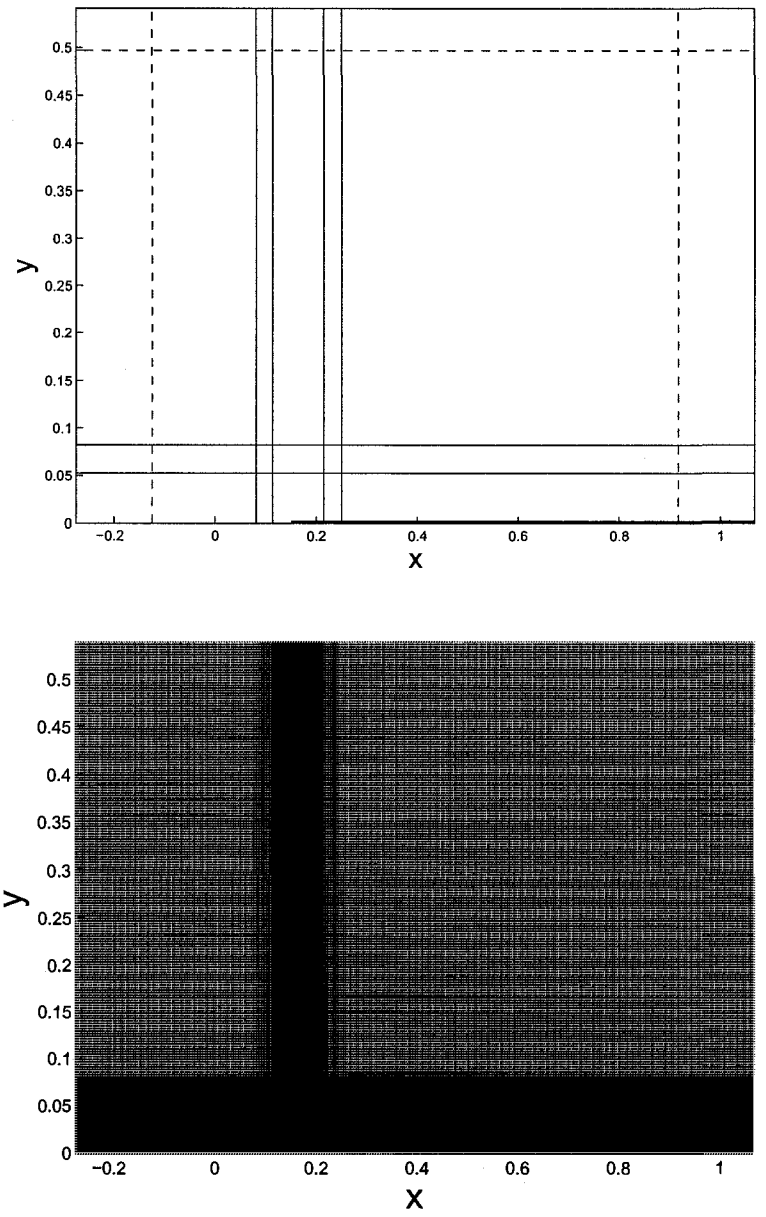

FIG. 33: Top: Schematic of domain including plate. In particular are grid lines where dx and dy change and boundary condition locations, Re_N=5000 with dashed lines for PML boundaries.; Bottom: grid, left to right, is dx=.0083, .0042, .0007, .0042, .0083 and, bottom to top, dy=.0006, .0012, .0024

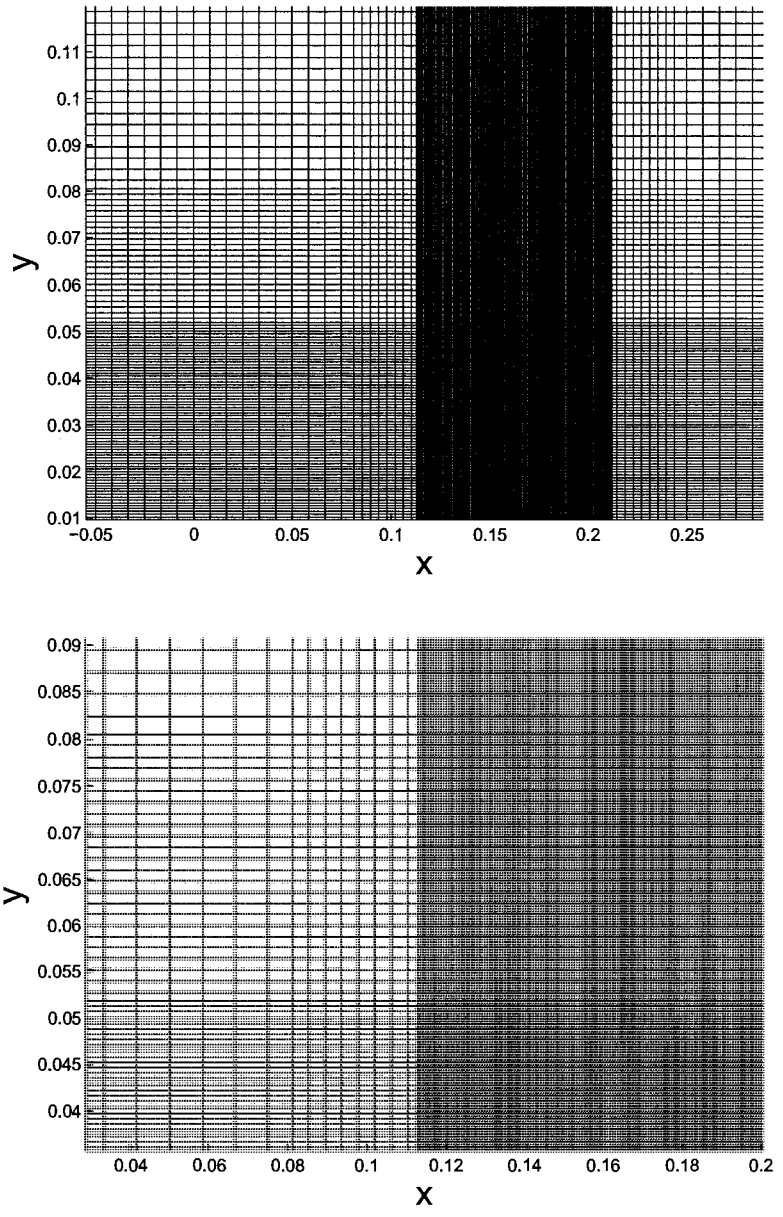

FIG. 34: Top and Bottom: one closer look at grid refinements and transition grid points, Re_N=5000

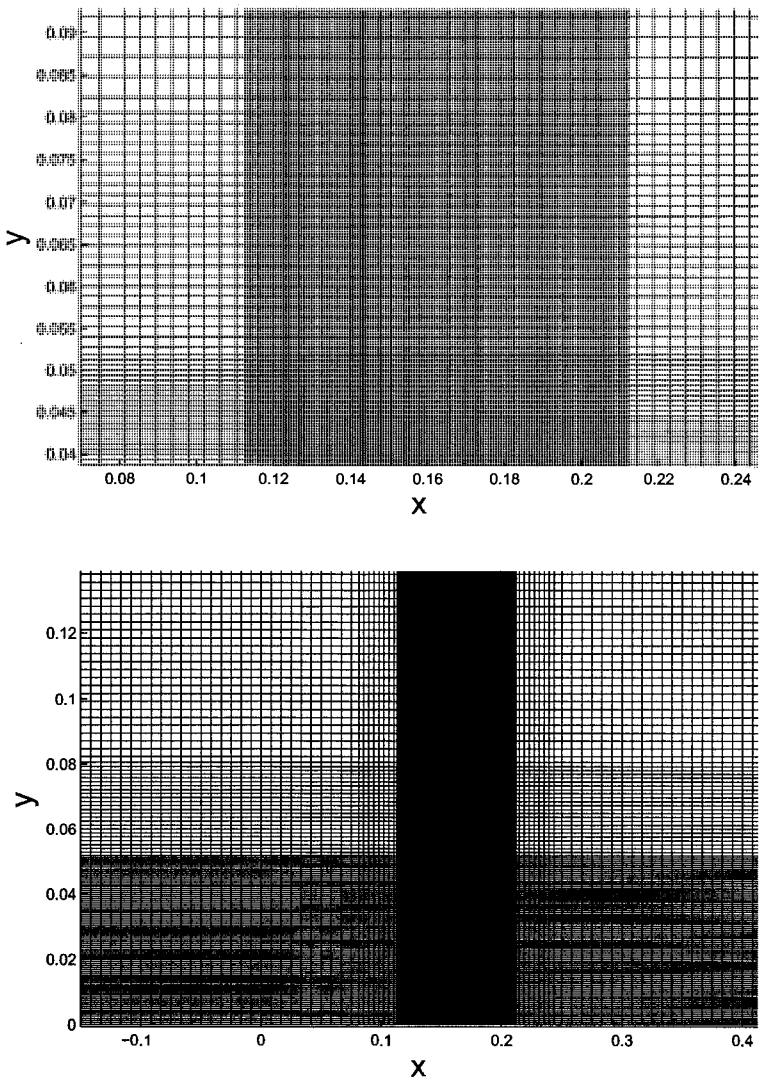

FIG. 35: Top and Bottom: another closer look at grid refinements and transition grid points, Re_N=5000

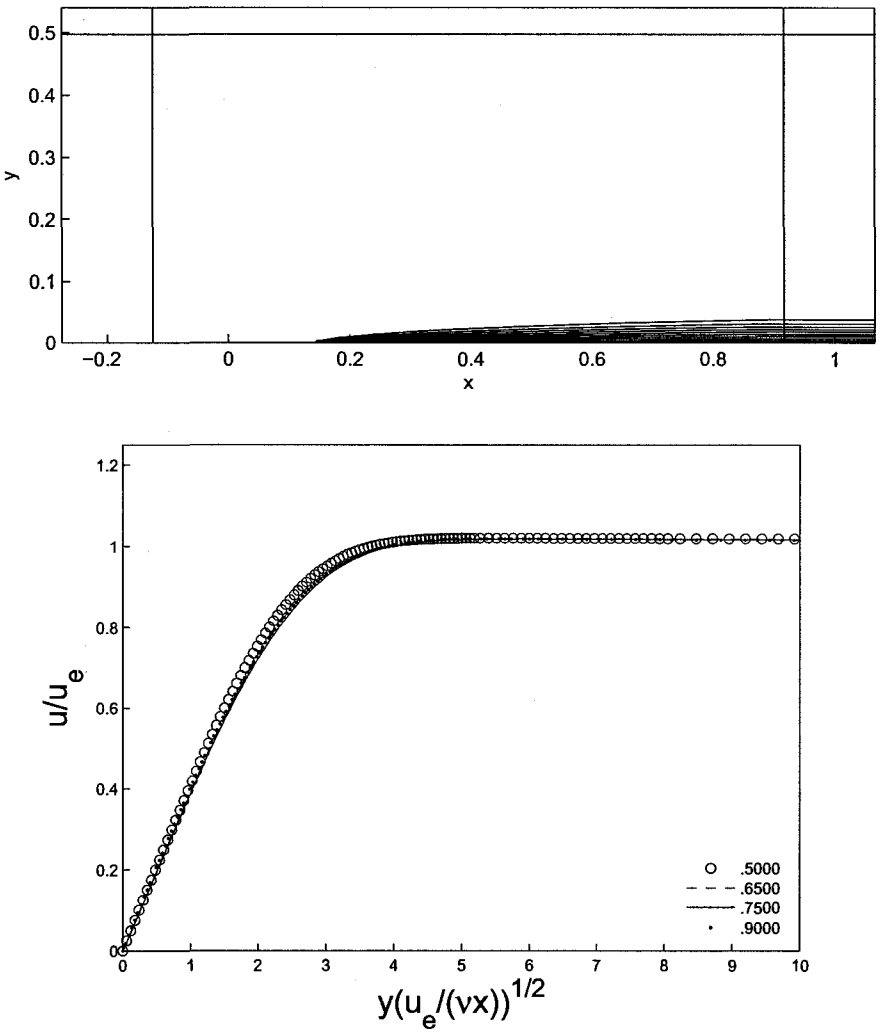

FIG. 36: Top: Boundary layer of stream-wise velocity Re_N=5000 at t=20.00 including borders of PML region; Bottom: Similarity velocity profile at x=.50, .65, .75, .90. Horizontal variable is $y(u_e/(\nu x))^{1/2}$ and u_e is the exterior stream-wise velocity, 0.1

Chapter V

GRID STRUCTURES II, DGM - FINITE DIFFERENCE SCHEME

As the spatial derivative formulas given in (21) and (23) are quite general, they can be used to construct other high-order schemes other than those given in Chapters **III** and **IV**. For instance, the nodal points in the element can be chosen to include the end points of the element. This will be referred to as Grid Structure II and will be studied in this chapter. As noted earlier, when the basis functions $\phi_\ell^n(\xi)$ are chosen to be the Lagrange polynomials, the expansion coefficients $u_{n\ell}$ become the same as the nodal values of the numerical solution at the prescribed nodes. This will result in a grid structure with double valued nodes, but a more compact stencil for the spatial derivative.

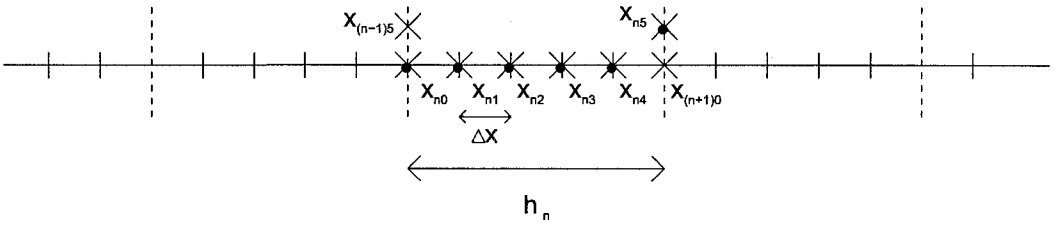

FIG. 37: Schematic of a finite difference grid partitioned into elements of length $h_n = p\Delta x$, where Δx is the grid size and p is the order of the basis functions.

In Grid Structure II, a uniform grid system that is often found in finite difference methods can be broken into elements of length $h = p\Delta x$, with the element boundary coinciding with a collocation point, as shown in Figure (37). In this case, the nodal points on the transformed coordinate ξ, $-1 \leq \xi \leq 1$, are

$$\xi_i = -1 + \frac{2i}{p}, \; i = 0, 1, 2, ...p \tag{55}$$

and the basis functions are

$$P_\ell(\xi) = \frac{\Pi_{i=0, i\neq\ell}^{p}(\xi - \xi_i)}{\Pi_{i=0, i\neq\ell}^{p}(\xi_\ell - \xi_i)} \tag{56}$$

Then, the finite difference scheme can be derived by substituting (56) into formulation (11) where the matrices are computed according to (12) and (14)-(19).

For higher order schemes, or $p \geq 7$, Chebychev-Lobatto collocation points are to be used to avoid the Runge phenomenon [9]. As these points are not uniformly

distributed, the data from this research is not emphasized as much as that from the uniform collocation points. However, it is worth noting that stability, super-convergence and accuracy for the applications is observed with these points as well.

V.1 FORMULATION

V.1.1 Interior Scheme

A fifth-order ($p = 5$) scheme is given below as an example. The finite difference formula for a set of five grid points is given by

$$\frac{\partial}{\partial x}\begin{bmatrix} u_{n0} \\ u_{n1} \\ u_{n2} \\ u_{n3} \\ u_{n4} \\ u_{n5} \end{bmatrix} = \frac{2}{h_n}\left(1+\theta\frac{|a|}{a}\right)\bar{\mathbf{M}}_{-}\begin{bmatrix} u_{(n-1)0} \\ u_{(n-1)1} \\ u_{(n-1)2} \\ u_{(n-1)3} \\ u_{(n-1)4} \\ u_{(n-1)5} \end{bmatrix} + \frac{2}{h_n}\left(\bar{\mathbf{M}}_0+\theta\frac{|a|}{a}\bar{\mathbf{N}}_0\right)\begin{bmatrix} u_{n0} \\ u_{n1} \\ u_{n2} \\ u_{n3} \\ u_{n4} \\ u_{n5} \end{bmatrix}$$

$$+\frac{2}{h_n}\left(1-\theta\frac{|a|}{a}\right)\bar{\mathbf{M}}_{+}\begin{bmatrix} u_{(n+1)0} \\ u_{(n+1)1} \\ u_{(n+1)2} \\ u_{(n+1)3} \\ u_{(n+1)4} \\ u_{(n+1)5} \end{bmatrix} \tag{57}$$

or more concisely:

$$\frac{\partial}{\partial x}\begin{bmatrix} u_{n0} \\ u_{n1} \\ u_{n2} \\ u_{n3} \\ u_{n4} \\ u_{n5} \end{bmatrix} = \frac{2}{h_n}\left(1+\theta\frac{|a|}{a}\right)\bar{\mathbf{M}}_{-}\begin{bmatrix} 0 \\ 0 \\ 0 \\ 0 \\ 0 \\ u_{(n-1)5} \end{bmatrix} + \frac{2}{h_n}\left(\bar{\mathbf{M}}_0+\theta\frac{|a|}{a}\bar{\mathbf{N}}_0\right)\begin{bmatrix} u_{n0} \\ u_{n1} \\ u_{n2} \\ u_{n3} \\ u_{n4} \\ u_{n5} \end{bmatrix}$$

$$+\frac{2}{h_n}\left(1-\theta\frac{|a|}{a}\right)\bar{\mathbf{M}}_+\begin{bmatrix} u_{(n+1)0} \\ 0 \\ 0 \\ 0 \\ 0 \end{bmatrix} \tag{58}$$

where, using (55) and (56), it is found that

$$\bar{\mathbf{M}}_- = \begin{bmatrix} 0 & 0 & 0 & 0 & 0 & -9 \\ 0 & 0 & 0 & 0 & 0 & \frac{7611}{6250} \\ 0 & 0 & 0 & 0 & 0 & -\frac{2274}{3125} \\ 0 & 0 & 0 & 0 & 0 & \frac{1773}{6250} \\ 0 & 0 & 0 & 0 & 0 & \frac{57}{3125} \\ 0 & 0 & 0 & 0 & 0 & \frac{3}{2} \end{bmatrix}, \bar{\mathbf{M}}_0 = \begin{bmatrix} \frac{79}{24} & \frac{25}{2} & -\frac{25}{2} & \frac{25}{3} & -\frac{25}{8} & 2 \\ -\frac{5368}{3125} & -\frac{65}{24} & 5 & -\frac{5}{2} & \frac{5}{6} & -\frac{2669}{25000} \\ \frac{21317}{25000} & -\frac{5}{4} & -\frac{5}{6} & \frac{5}{2} & -\frac{5}{8} & \frac{13763}{37500} \\ -\frac{13763}{37500} & \frac{5}{8} & -\frac{5}{2} & \frac{5}{6} & \frac{5}{4} & -\frac{21317}{25000} \\ \frac{2669}{25000} & -\frac{5}{6} & \frac{5}{2} & -5 & \frac{65}{24} & \frac{5368}{3125} \\ -2 & \frac{25}{8} & -\frac{25}{3} & \frac{25}{2} & -\frac{25}{2} & -\frac{79}{22} \end{bmatrix}$$

$$\bar{\mathbf{N}}_0 = \begin{bmatrix} 9 & 0 & 0 & 0 & 0 & -\frac{3}{2} \\ -\frac{7611}{6250} & 0 & 0 & 0 & 0 & -\frac{57}{3125} \\ \frac{2274}{3125} & 0 & 0 & 0 & 0 & -\frac{1773}{6250} \\ -\frac{1773}{6250} & 0 & 0 & 0 & 0 & \frac{2274}{3125} \\ -\frac{57}{3125} & 0 & 0 & 0 & 0 & -\frac{7611}{6250} \\ -\frac{3}{2} & 0 & 0 & 0 & 0 & 9 \end{bmatrix}, \bar{\mathbf{M}}_+ = \begin{bmatrix} -\frac{3}{2} & 0 & 0 & 0 & 0 & 0 \\ -\frac{57}{3125} & 0 & 0 & 0 & 0 & 0 \\ -\frac{1773}{6250} & 0 & 0 & 0 & 0 & 0 \\ \frac{2274}{3125} & 0 & 0 & 0 & 0 & 0 \\ -\frac{7611}{6250} & 0 & 0 & 0 & 0 & 0 \\ 9 & 0 & 0 & 0 & 0 & 0 \end{bmatrix}$$

Note that the choice of $\theta = 1$ will yield the upwind ($a > 0$) and downwind ($a < 0$) schemes.

Coefficients for order $p = 9$, along with the corresponding Chebychev-Lobatto collocation points, are listed in the Appendix.

As (58) illustrates, the neighboring elements contribute at most one collocation point, so another view of the finite-difference like scheme is:

$$\frac{\partial u_{nl}}{\partial x} = \frac{2}{h}[\alpha_l u_{(n-1)p} + \sum_{k=0}^{p} d_{lk} u_{nk} \; + \beta_l u_{(n+1)0}]$$

or in vector form:

$$\frac{\partial}{\partial x}\begin{bmatrix} u_{n0} \\ u_{n1} \\ \vdots \\ u_{np} \end{bmatrix} = \frac{2}{h_n}\begin{bmatrix} \alpha_0 & d_{10} & d_{11} & \cdots & d_{1p} & \beta_0 \\ \alpha_1 & d_{20} & d_{21} & \cdots & d_{2p} & \beta_1 \\ \vdots & \vdots & \vdots & \ddots & \vdots & \vdots \\ \alpha_p & d_{p0} & d_{p1} & \cdots & d_{pp} & \beta_p \end{bmatrix}\begin{bmatrix} u_{(n-1)p} \\ u_{n0} \\ u_{n1} \\ \vdots \\ u_{np} \\ u_{(n+1)0} \end{bmatrix} \equiv \frac{2}{h_n} D_\theta \begin{bmatrix} u_{(n-1)p} \\ u_{n0} \\ u_{n1} \\ \vdots \\ u_{np} \\ u_{(n+1)0} \end{bmatrix} \tag{59}$$

There are patterns in the coefficients for $\theta = 1$. If $a < 0$ then $\alpha_i = 0$ and if $a > 0$ then $\beta_i = 0$ and in each case the coefficients are anti-symmetric for $\pm$ a. However, if $\theta \neq 1$ then $\alpha_i \neq 0$ and $\beta_i \neq 0$.

In particular, if we take $\theta = 1$ and $a > 0$, we get an upwind difference operator $\mathbf{D}_+$ as follows:

$$\mathbf{D}_+ = \frac{2}{h_n}\begin{bmatrix} -18 & \frac{295}{24} & \frac{25}{2} & -\frac{25}{2} & \frac{25}{3} & -\frac{25}{8} & \frac{1}{2} & 0 \\ \frac{7611}{3125} & -\frac{18347}{6250} & -\frac{65}{24} & 5 & -\frac{5}{2} & \frac{5}{6} & -\frac{1}{8} & 0 \\ -\frac{4548}{3125} & \frac{39509}{25000} & -\frac{5}{4} & -\frac{5}{6} & \frac{5}{2} & -\frac{5}{8} & \frac{1}{12} & 0 \\ \frac{1773}{3125} & -\frac{24401}{37500} & \frac{5}{8} & -\frac{5}{2} & \frac{5}{6} & \frac{5}{4} & -\frac{1}{8} & 0 \\ \frac{114}{3125} & \frac{2213}{25000} & -\frac{5}{6} & \frac{5}{2} & -5 & -\frac{65}{24} & \frac{1}{2} & 0 \\ 3 & -\frac{7}{2} & \frac{25}{8} & -\frac{25}{3} & \frac{25}{2} & -\frac{25}{2} & \frac{137}{24} & 0 \end{bmatrix}$$

Unlike Grid Structure I, stability of central schemes ($\theta = 0$) were not observed. This may be because of the double values of grid points at element boundaries and that DGM allows these values to be unequal. All orders of p tested (to 11^{th} order) yield instability. Therefore, $\theta > 0$ is recommended for Grid Structure II.

V.1.2 Non-uniform grids

As with Grid Structure I, DGM-FD with Grid Structure II adapts to non-uniform grids while keeping the same scheme coefficients.

Grid size may shift in groups of $p+1$ collocation points (per element) where grid spacings of Δx_1 on one element change to another spacing Δx_2 on a neighboring element. The coefficients of the scheme stay the same and the change in grid spacing is reflected only in the value of h_n, as used in (58).

The argument to verify that the coefficients generated by (58) in section **V.1.1**, and in the following section, **V.1.3**, will remain the same, follows that from section **III.1.2** for Grid Structure I.

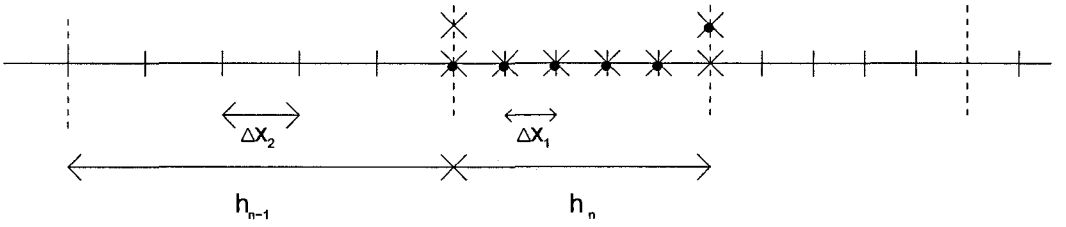

FIG. 38: Schematic of nonuniform grid structure, h_{n-1}=pΔx_2, h_n=pΔx_1.

As in section **III.1.2**, the matrices defined in (12) are dependent on the basis polynomials, P, so it suffices to show that these stay the same with a change of grid spacing. As presented earlier, if the relative spacing of collocation points is the same on each element, then the basis polynomials are the same. Using the same steps presented in **III.1.2** applied to these ξ_i in (55), this is the case, and note that, as seen in Figure (38), unlike Grid Structure I, no transition grid is necessary.

Recall the block structure of the derivative on each element, as seen in (59) and Figure (39), and include the different element lengths in the value of the factor $\frac{2}{h_n}$ in front of each block . Any element or portion of the domain can be formulated this way, including regions that contain the boundary.

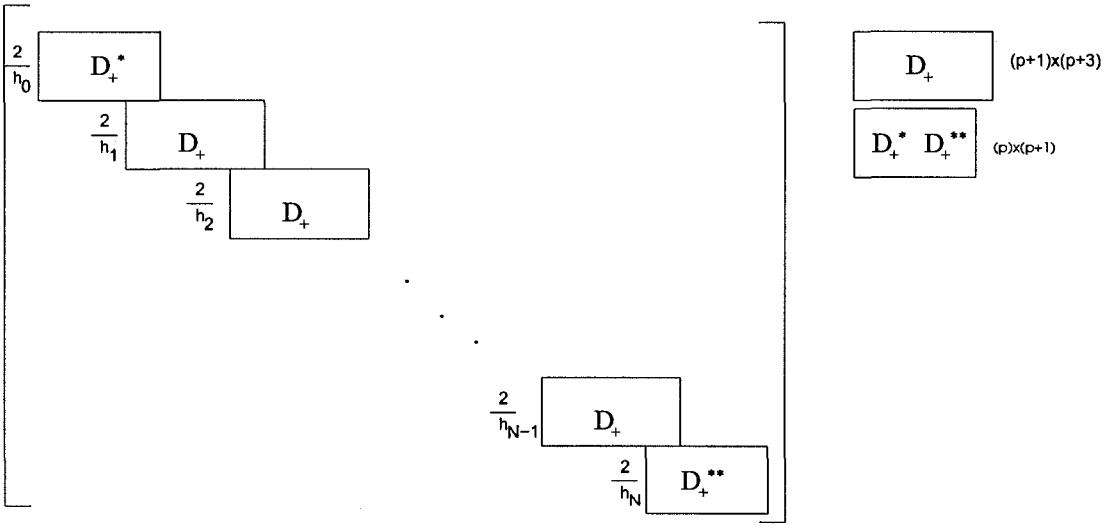

FIG. 39: Global matrix block structure for nonuniform grids.

V.1.3 Boundary closures

Forming a boundary closure is accomplished by a linear combination of two columns of coefficients. Grid points near the boundary are shown in Figure (40) where a left boundary is closed one order down, $p = 4$, for added stability [22]. Using the formulation outlined in (59), boundary closure involves adjusting the coefficient for the first collocation point, d_{i0}, of the first element by adding α_i and for last collocation point, the coefficients β_i are added to d_{ip}. The interior and boundary coefficients follow from the same matrices generated by (12) and (14)-(19) as no adjustment to the collocation points on the boundary elements is needed, so the basis polynomials, P, on all elements, stay the same. This is another difference between Grid I and Grid II structures.

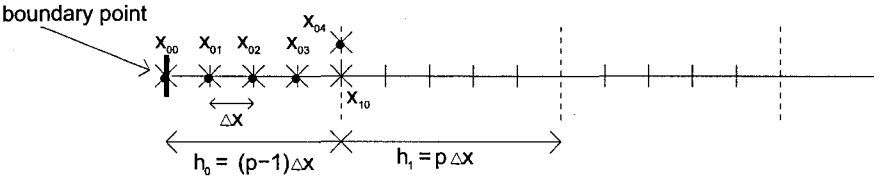

FIG. 40: Schematic of grids at the boundary, $p = 4$

For instance, the general finite difference matrix for 4^{th} order closure, denoted by $\mathbf{D}_\theta^n$, is a linear combination of the 4^{th} order (interior) coefficients as given below

$$\mathbf{D}_\theta^0 = (1 + \frac{\theta|a|}{a})\bar{\mathbf{M}}_-^{cl} + (\bar{\mathbf{M}}_0^{cl} + \frac{\theta|a|}{a}\bar{\mathbf{N}}_0^{cl}) \tag{60}$$

$$\mathbf{D}_\theta^N = (\bar{\mathbf{M}}_0^{cl} + \frac{\theta|a|}{a}\bar{\mathbf{N}}_0^{cl}) + (1 - \frac{\theta|a|}{a})\bar{\mathbf{M}}_+^{cl} \tag{61}$$

For the scheme on the 1^{st} element, $\mathbf{D}_\theta^0$, the first column of $\bar{\mathbf{M}}_-^{cl}$ is multiplied by $(1+\frac{\theta|a|}{a})$, and added to the first column of $\bar{\mathbf{M}}_0$. For the N^{th} element coefficients, $\mathbf{D}_\theta^N$, the last column of $\bar{\mathbf{M}}_+^{cl}$ is multiplied by $(1-\frac{\theta|a|}{a})$ and added to the last column of $\bar{\mathbf{M}}_0$, for the coefficient matrices given below

$$\bar{\mathbf{M}}_-^{cl} = \begin{bmatrix} -\frac{25}{4} & 0 & 0 & 0 & 0 \\ \frac{485}{512} & 0 & 0 & 0 & 0 \\ -\frac{15}{32} & 0 & 0 & 0 & 0 \\ \frac{85}{512} & 0 & 0 & 0 & 0 \\ -\frac{5}{4} & 0 & 0 & 0 & 0 \end{bmatrix}, \bar{\mathbf{M}}_0^{cl} = \begin{bmatrix} \frac{25}{12} & 8 & -6 & \frac{8}{3} & -\frac{7}{4} \\ -\frac{741}{512} & -\frac{5}{3} & 3 & -1 & \frac{511}{1536} \\ \frac{61}{96} & -\frac{4}{3} & 0 & \frac{4}{3} & -\frac{61}{96} \\ -\frac{511}{1536} & 1 & -3 & \frac{5}{3} & \frac{741}{512} \\ \frac{7}{4} & -\frac{8}{3} & 6 & -8 & -\frac{25}{12} \end{bmatrix}$$

$$\bar{\mathbf{N}}_0^{cl} = \begin{bmatrix} \frac{25}{4} & 0 & 0 & 0 & \frac{5}{4} \\ -\frac{485}{512} & 0 & 0 & 0 & -\frac{85}{512} \\ \frac{15}{32} & 0 & 0 & 0 & \frac{15}{32} \\ -\frac{85}{512} & 0 & 0 & 0 & -\frac{485}{512} \\ \frac{5}{4} & 0 & 0 & 0 & \frac{25}{4} \end{bmatrix}, \bar{\mathbf{M}}_+^{cl} = \begin{bmatrix} 0 & 0 & 0 & 0 & \frac{5}{4} \\ 0 & 0 & 0 & 0 & -\frac{85}{512} \\ 0 & 0 & 0 & 0 & \frac{15}{32} \\ 0 & 0 & 0 & 0 & -\frac{485}{512} \\ 0 & 0 & 0 & 0 & \frac{25}{4} \end{bmatrix}$$

To use the coefficients given above for an interior scheme with (58), rearrange the columns of $\bar{\mathbf{M}}_-^{cl}$ to resemble coefficient matrix $\bar{\mathbf{M}}_-$ by moving zero columns to the left and sole non-zero coefficients to the right most column. Likewise, columns in $\bar{\mathbf{M}}_+^{cl}$ can be moved as per $\bar{\mathbf{M}}_+$, and these, with $\bar{\mathbf{M}}_0^{cl}$ and $\bar{\mathbf{N}}_0^{cl}$, complete a 4^{th} order interior scheme.

For the closure scheme, in particular, if we take $\theta = 1$ and $a > 0$, we get an upwind difference operator $\mathbf{D}_+$, with coefficients on the first element:

$$\mathbf{D}_+^* = \frac{2}{h_0} \begin{bmatrix} -\frac{25}{6} & 8 & -6 & \frac{8}{3} & -\frac{1}{2} \\ -\frac{1}{2} & -\frac{5}{3} & 3 & -1 & \frac{1}{6} \\ \frac{1}{6} & -\frac{4}{3} & 0 & \frac{4}{3} & -\frac{1}{6} \\ -\frac{1}{6} & 1 & -3 & \frac{5}{3} & \frac{1}{2} \\ \frac{1}{2} & -\frac{8}{3} & 6 & -8 & \frac{25}{6} \end{bmatrix}$$

and the corresponding operator on the last element:

$$\mathbf{D}_+^{**} = \frac{2}{h_N} \begin{bmatrix} \frac{25}{3} & 8 & -6 & \frac{8}{3} & -\frac{1}{2} \\ -\frac{613}{256} & -\frac{5}{3} & 3 & -1 & \frac{1}{6} \\ \frac{53}{48} & -\frac{4}{3} & 0 & \frac{4}{3} & -\frac{1}{6} \\ -\frac{383}{768} & 1 & -3 & \frac{5}{3} & \frac{1}{2} \\ 3 & -\frac{8}{3} & 6 & -8 & \frac{25}{6} \end{bmatrix}$$

The above coefficients are for a single element, so the block structure of the global matrix is presented in a diagram form. In Figure (41) if, instead, periodic boundary conditions are desired, in place of $\mathbf{D}_+^*$ and $\mathbf{D}_+^{**}$, the first and last columns of $\mathbf{D}_+$ 'wrap around' the global matrix in the first and last blocks respectively, and the order for boundary elements can be kept the same as interior.

For the uniform scheme, another option for stable boundary closure is to use same order coefficients generated from the Chebychev-Lobatto nodal points. In other words, $p = 6^{ch} - 6 - 6^{ch}$ where the first and last elements are the 6^{th} order Chebychev-Lobatto nodal points is a stable scheme. Consequently, the higher order schemes, unaltered on boundary elements, are stable .

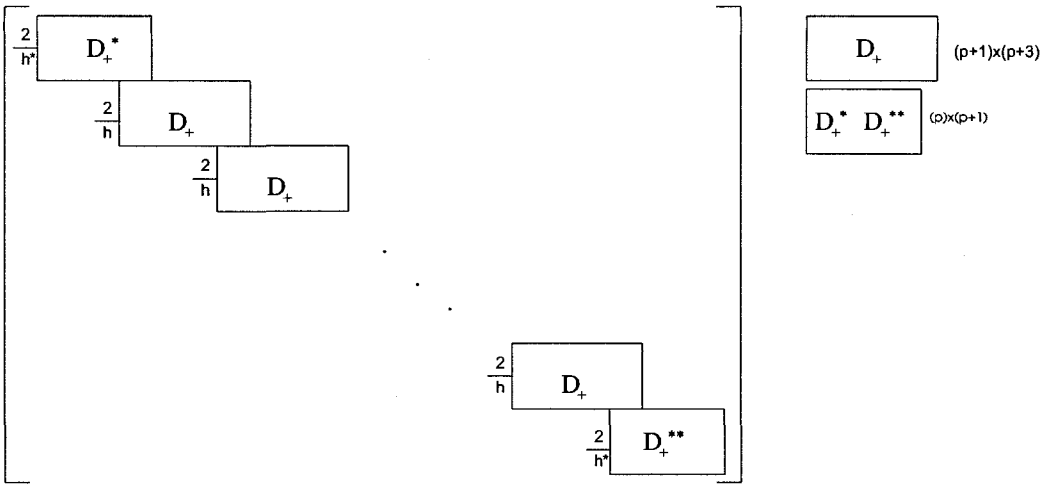

FIG 41: Global matrix block structure for uniform grids with degree lower closure.

V.2 STABILITY AND SUPER-ACCURACY PROPERTIES

V.2.1 Stability

To study the stability of the scheme with boundary closure, we perform an eigenvalue analysis when the scheme is applied to the wave equation

$$\frac{\partial u}{\partial t} + \frac{\partial u}{\partial x} = 0 \tag{62}$$

with a given boundary condition at the left boundary.

Let $\mathbf{u}^h$ denote the vector that contains all nodal values, then the semi-discrete equation for (62) can be written as

$$\frac{d\mathbf{u}^h}{dt} + \mathbf{D}\mathbf{u}^h = 0 \tag{63}$$

where $\mathbf{D}$ is the global differentiation matrix.

For the upwind scheme ($\theta = 1$ and $a > 0$), the global matrix denoted by $\mathbf{G}_+$, where $\mathbf{D}_+^*$ and $\mathbf{D}_+^{**}$ are sub-matrices from **V.1.3**, is of the form (also see Figure (41))

$$\mathbf{G}_+ = \begin{bmatrix} D_+^* & \bar{0} & \bar{0} & \bar{0} & \cdots & \bar{0} & \bar{0} \\ \bar{0} & D^+ & \bar{0} & \bar{0} & \cdots & \bar{0} & \bar{0} \\ \bar{0} & \bar{0} & D^+ & \bar{0} & \cdots & \bar{0} & \bar{0} \\ \vdots & \ddots & \ddots & \ddots & \ddots & \vdots & \vdots \\ \bar{0} & \cdots & \bar{0} & \bar{0} & D^+ & \bar{0} & \bar{0} \\ \bar{0} & \cdots & \bar{0} & \bar{0} & \bar{0} & D_+ & \bar{0} \\ \bar{0} & \cdots & \bar{0} & \bar{0} & \bar{0} & \bar{0} & D_+^{**} \end{bmatrix} \tag{64}$$

For stability, the eigenvalues of $\tilde{\mathbf{G}}_+$, where an over tilde denotes the matrix without the first row and first column, must have positive real parts [10]. The eigenvalues for the fifth-order scheme and the boundary closure presented in previous sections with N=30 elements are shown in Figure (42), left. Stability of the eigenvalues is observed. The eigenvalue plots for the higher order scheme p=9, with Chebychev-Lobatto points, show stability in Figure (42), right with N=30. This was repeated for N=5 to 200, for each p, where stability was maintained.

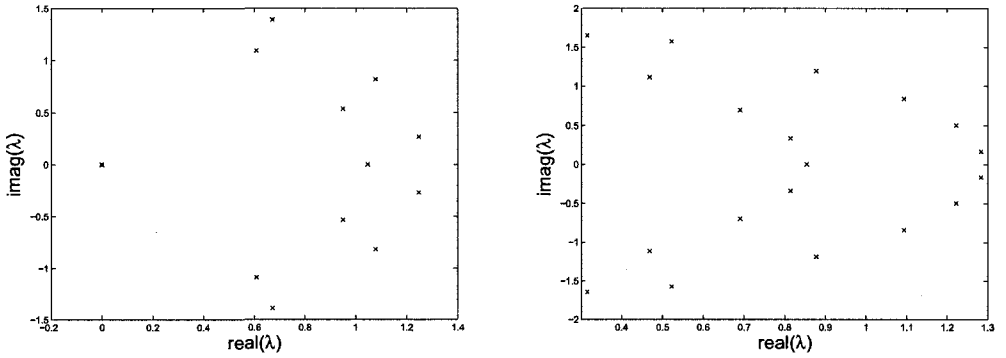

FIG. 42: Left: eigenvalue λ of upwind scheme $\tilde{\mathbf{D}}_+$. Eigenvalues are computed using $N = 30$ elements and $p = 5$. Right: Eigenvalues λ of upwind scheme $\tilde{\mathbf{D}}_+$. Eigenvalues are computed using $N = 30$ elements, $p = 9$, and Chebychev-Lobatto grid.

V.2.2 Super-convergence for wave propagation

The Fourier analysis on the numerical wavenumber for the difference formula (58) should be the same as those for the general discontinuous Galerkin method [25, 27, 3]. As mentioned for Grid Structure I, it has been shown that the numerical wavenumber for DGM is accurate to order $2p+1$ where p is the order of basis functions, the super-convergency property of DGM.

As before, to demonstrate the strong super-accuracy for wave propagation problems, equation (62) is solved in a domain of $0 \leq x \leq 1$ with periodic boundary condition and an initial condition

$$u(x,0) = e^{-\frac{\ln(2)}{0.0481^2}\left(x-\frac{1}{2}\right)^2} \tag{65}$$

and numerical solution is calculated using the upwind scheme given in the previous sections, from $t = 0$ to $t = 51$. To demonstrate the super-accuracy for propagation errors, the solutions at $t = 1$ and $t = 51$ are compared and the L2 norm of the error, $||u^h(x,51) - u^h(x,1)||_2$, is shown in Figure (43) as a function of total number of grid points in the grid refine study. A convergence order close to 11 is observed even though the order of the basis function is $p = 5$, matching the theoretical rate of convergence for the propagation error of order $2p + 1$. See Table II. While Grid Structure II does not have a stable central scheme, (θ=0), investigation on values of θ, other than 1, is of interest. Note that the super-convergence is present in, for example, for $\theta = 0.5$. The scheme is stable and same parameters are used, see Table III.

TABLE II: Convergence Rate data $p = 3, 4, 5, 6$ for Grid Structure II

	θ=1					
	error	*rate*	*error*	*rate*	*error*	*rate*
N		$p=3$		$p=4$		$p=5$
10	—	—	3.4812E-2	—	1.0882E-2	—
15	—	—	8.1723E-3	3.57420	9.3403E-4	6.05570
20	1.7536E-2	—	1.6383E-3	5.58650	7.5280E-5	8.75400
25	7.2867E-3	3.9357	3.2545E-4	7.24280	7.9646E-6	10.0658
30	2.9879E-3	4.8897	7.4643E-5	8.07610	1.1685E-6	10.5270
35	1.2548E-3	5.6280	2.0024E-5	8.53570	2.2870E-7	10.5812
40	5.5270E-4	6.1402	6.2671E-6	8.69908	—	—
45	2.5812E-4	6.4644	2.2300E-6	8.77340	—	—
50	1.2800E-4	6.6575	—	—	—	—

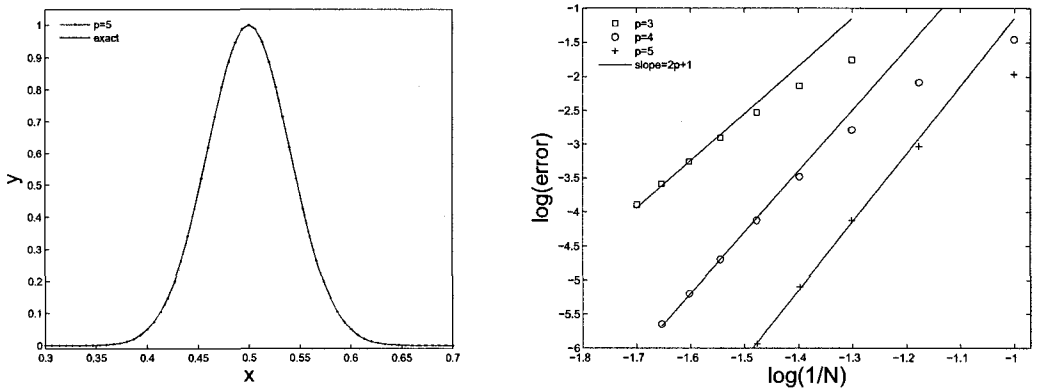

FIG. 43: Left: numerical solution at $t = 51$ in a domain of $[0, 1]$ with periodic boundary condition. Right: mesh refinement study on the L2 norm of the difference between numerical solutions at $t = 1$, $u^h(x, 1)$, and at $t = 51$, $u^h(x, 51)$. $p = 3, 4, 5$ as indicated.

TABLE III: Convergence Rate data $p = 3, 4, 5$ for Grid Structure II

			θ=0.5			
	error	*rate*	*error*	*rate*	*error*	*rate*
N		$p = 3$		$p = 4$		$p = 5$
10	—	—	4.3915E-2	—	1.2243E-2	—
15	—	—	1.1566E-2	3.2907	9.5595E-4	6.2890
20	1.4535E-2	—	2.6231E-3	5.1572	5.5713E-5	9.8809
25	6.0603E-3	3.9204	5.6223E-4	6.9024	4.5372E-6	11.2387
30	2.5681E-3	4.7088	1.2564E-4	8.2189	6.9358E-7	10.3017
35	1.1408E-3	5.2637	3.0320E-5	9.2225	—	—
40	5.3819E-4	5.6264	8.2640E-6	9.7343	—	—
45	2.6986E-4	5.8614	2.5775E-6	9.8921	—	—
50	1.4310E-4	6.0206	—	—	—	—

For Chebychev-Lobatto collocation points, to demonstrate the strong super-accuracy for wave propagation problems, equation (62) is solved with initial condition

$$u(x,0) = e^{-\frac{\ln(2)}{0.033960^2}\left(x-\frac{1}{2}\right)^2} \tag{66}$$

All other conditions are the same. As shown in Figure (43), right, the grid refine study reveals the expected super-convergence with solution profile for $p = 9$, Figure (43), left. Note that for $p = 7, 8, 9$ the rates, numerically, in the tables listed below are closer (at their greatest) to $2p$, $2p$, $2p - 1$ respectively rather than $2p + 1$. This drop in rate(s) as N increases is attributed to machine accuracy, not to the properties of the scheme. See Table IV.

TABLE IV: Convergence Rate data $p = 7, 8, 9$ for Grid Structure II

			θ=1			
	error	*rate*	*error*	*rate*	*error*	*rate*
N		$p = 7$		$p = 8$		$p = 9$
14	—	—	5.6981E-5	—	5.6143E-6	—
16	—	—	1.0179E-5	12.8987	6.9330E-7	15.6334
18	3.0994E-5	—	1.0916E-6	14.2929	9.7579E-8	16.6890
20	8.3038E-6	12.5001	3.8915E-7	15.0582	1.6369E-8	16.9446
22	2.3575E-6	13.2110	8.8807E-8	15.5015	3.3534E-9	16.6343
24	7.1915E-7	13.6448	2.2632E-8	15.7117	—	—
26	2.3617E-7	13.9123	6.6544E-9	15.6753	—	—
28	8.3085E-8	14.0970	2.1057E-9	15.1144	—	—
30	3.1111E-8	14.2377	—	—	—	—
32	1.2391E-8	14.2643	—	—	—	—

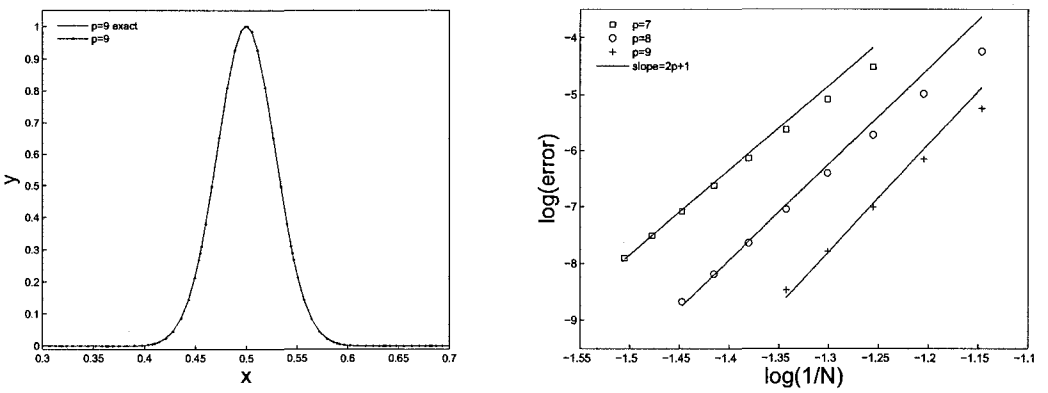

FIG. 44: Left: numerical solution at $t = 51$ in a domain of $[0, 1]$ with periodic boundary condition, $p = 9$. Right: mesh refinement study on the L2 norm of the difference between numerical solutions at $t = 1$, $u^h(x, 1)$, and at $t = 51$, $u^h(x, 51)$. $p = 7, 8, 9$, Chebychev-Lobatto points, as indicated.

The numerical wave number accuracy of the method is examined for DGM-FD and then compared to DRP and compact schemes on equation (62) with domain $-50 \leq x \leq 450$, periodic boundary condition and initial condition

$$u(x, 0) = e^{-\frac{\ln(2)}{3^2}(x)^2} \tag{67}$$

The Fast Fourier Transform (FFT) function in Matlab is used to obtain the difference, $k^* - k$, where k^* is the numerical approximation to the wave number k. On double valued nodal points, the value from the element on the left is used in FFT. As noted for Grid Structure I in section **III.2.2**, if the FFT of exact solution is $u_{exact}(k, t) = e^{-ikt}\hat{u}_0(k)$ then the FFT of numerical solution can be written in terms of numerical wavenumber k^* as $\hat{u}^*(k, t) = e^{-ik^*t}\hat{u}_0(k)$. Therefore an estimation of the difference, $k^* - k$, is

$$k^* - k = -\frac{ln[\hat{u}^*(k, t)/\hat{u}_{exact}(k, t)]}{it}. \tag{68}$$

First we examine the DGM-FD scheme and study the numerical wave number accuracy for the upwind ($\theta = 1$) schemes for varying orders, p=3,4,5. Note in Figure (45) that, as expected, the numerical solution becomes better resolved as the order, p, increases for the upwind scheme.

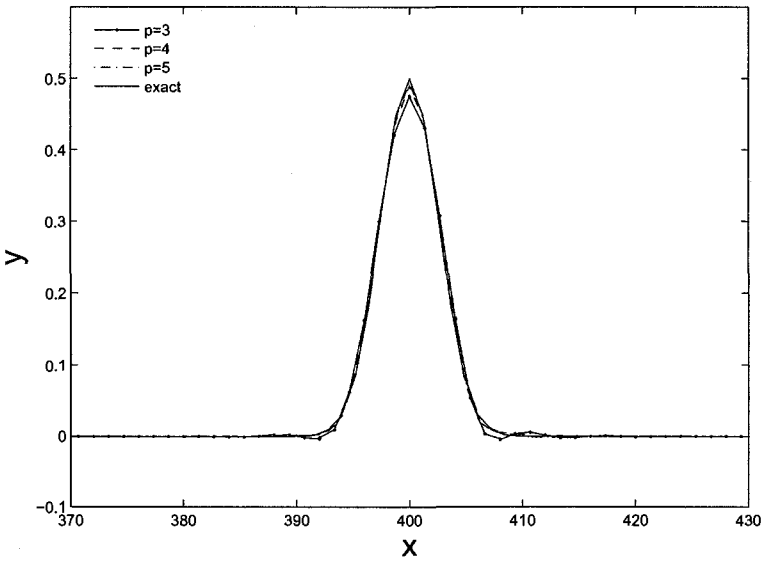

FIG. 45: Gaussian profile Upwind $p = 3, 4, 5$.

The numerical wave number accuracy, both for dispersion, Real$(k^* - k)$, and dissipation, Imag$(k^* - k)$, follows the same trend. See Figure (46).

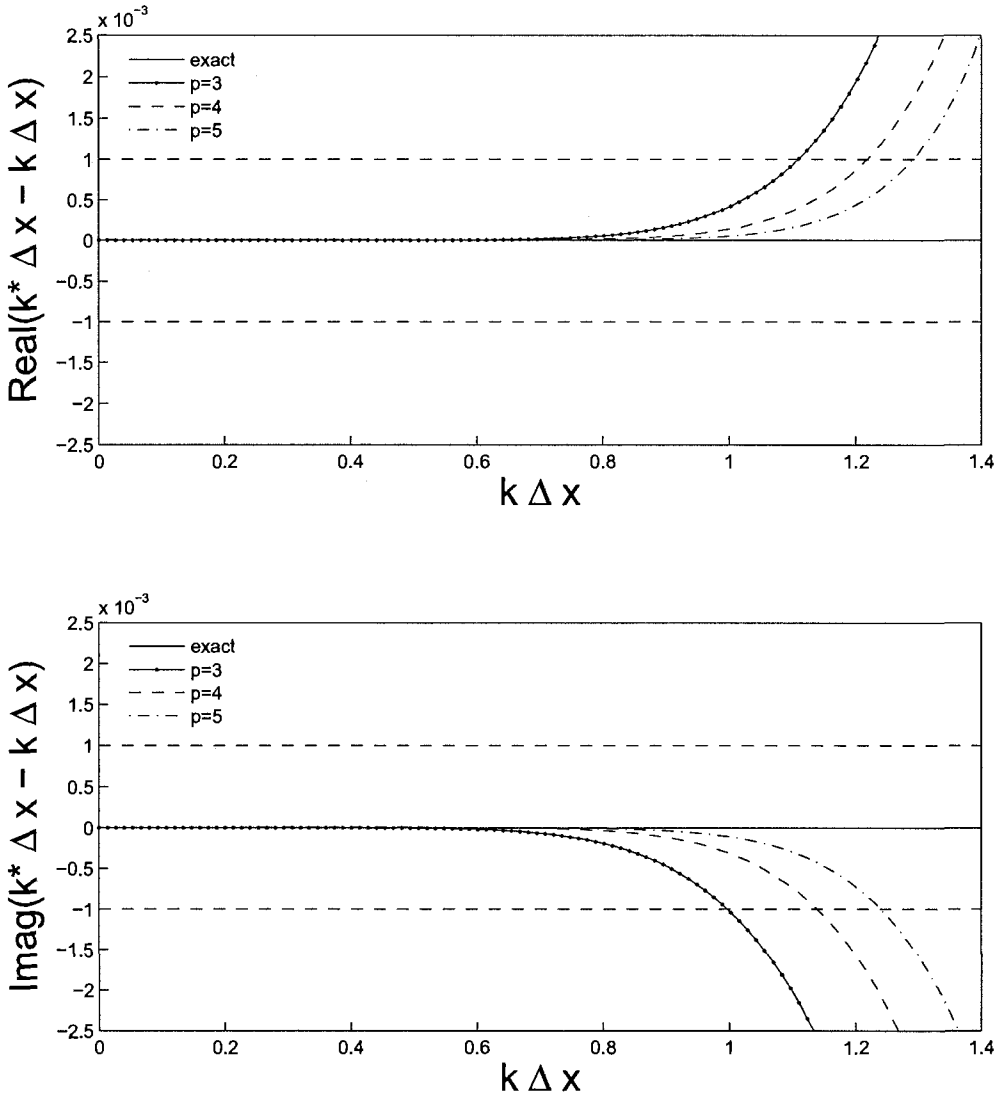

FIG. 46: Top: Real(k*-k) upwind, $p = 3, 4, 5$; Bottom: Imag(k*-k) upwind, $p = 3, 4, 5$.

Now we turn to comparing the performances of DGM-FD, DRP and compact schemes. First, their numerical solutions, then the numerical wave number accuracy data followed by a log-log plot, to show their numerical wave number convergence rates. In Figure (47), profiles for DGM-FD of p=5, 4^{th} and 6^{th} order compact and DRP are shown. DGM-FD performs similarly with 6^{th} order compact scheme and better than both 4^{th} order and DRP. In Figure (48), top, the dispersion properties are examined. For the given tolerance of 10^{-3}, the difference between numerical and theoretical wave numbers, $k^* - k$, is comparable for 6^{th} order compact, and DRP, with $k\Delta x \leq 1$, DGM-FD has larger range, $k\Delta x \leq 1.3$. In Figure (48), bottom, the dissipation properties are examined and as DGM-FD is an upwind scheme, it shows more dispersion than the other (central) schemes. Figure (49) shows the rate of convergence (slope in figure) for DGM-FD as higher than 4^{th}, 6^{th}, 8^{th} order compact and DRP for the given range of Real($k\Delta x$).

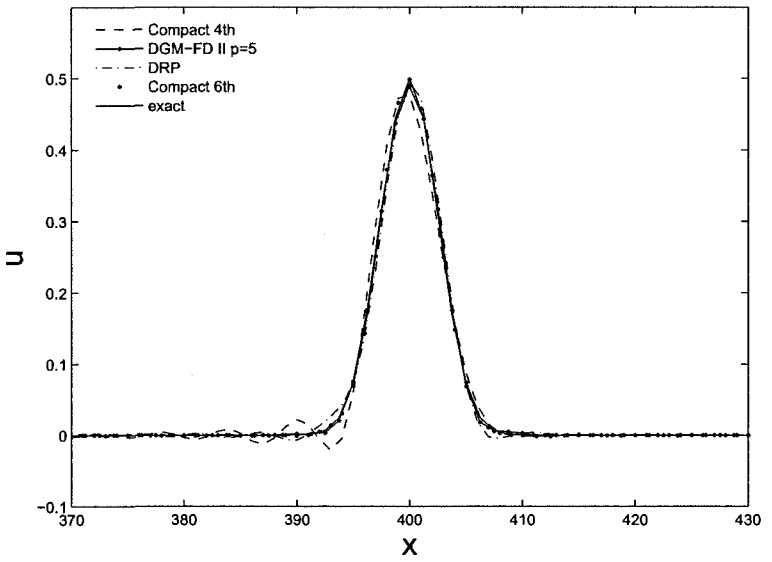

FIG. 47: Gaussian profile Upwind $p = 3, 4, 5$.

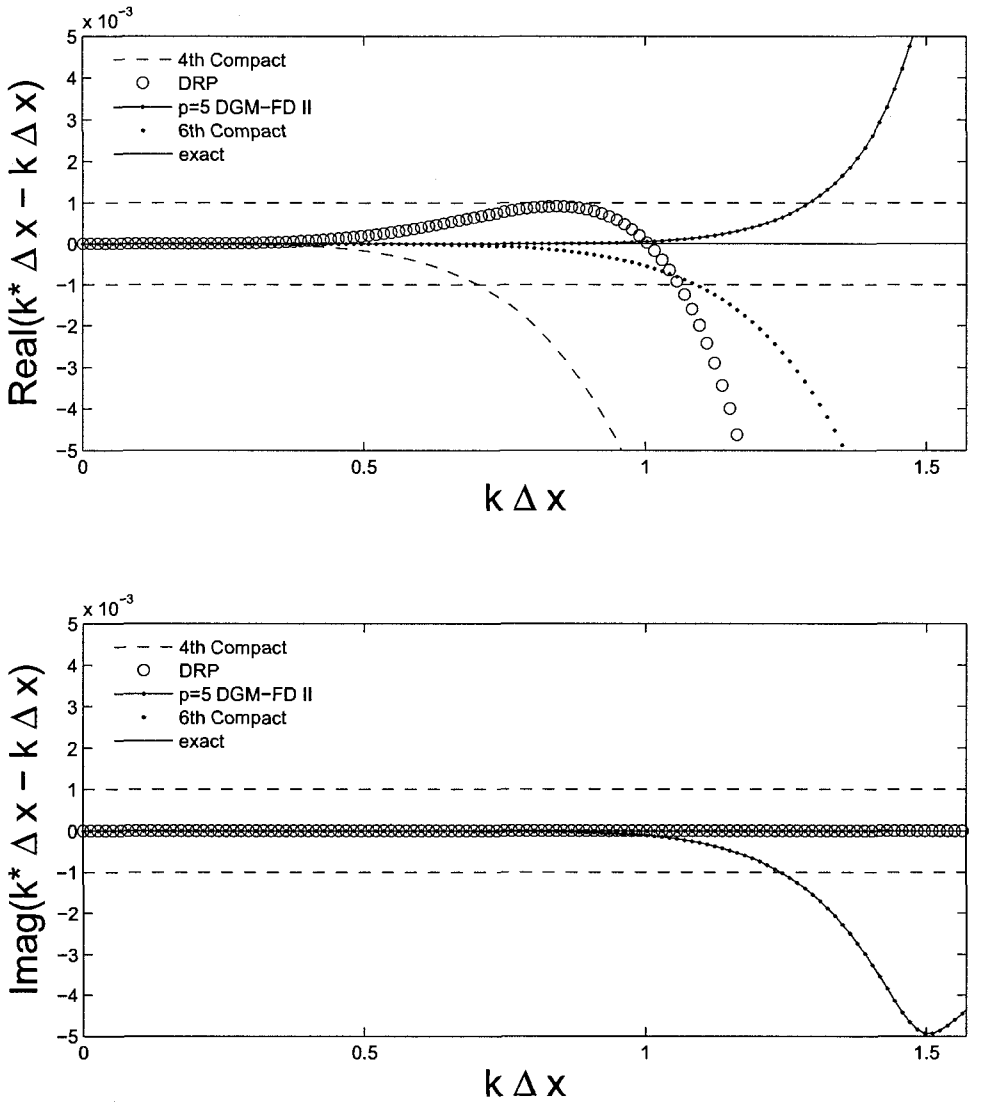

FIG. 48: Top: Real(k*-k) Compact, DRP DGM-FD; Bottom: Imag(k*-k).

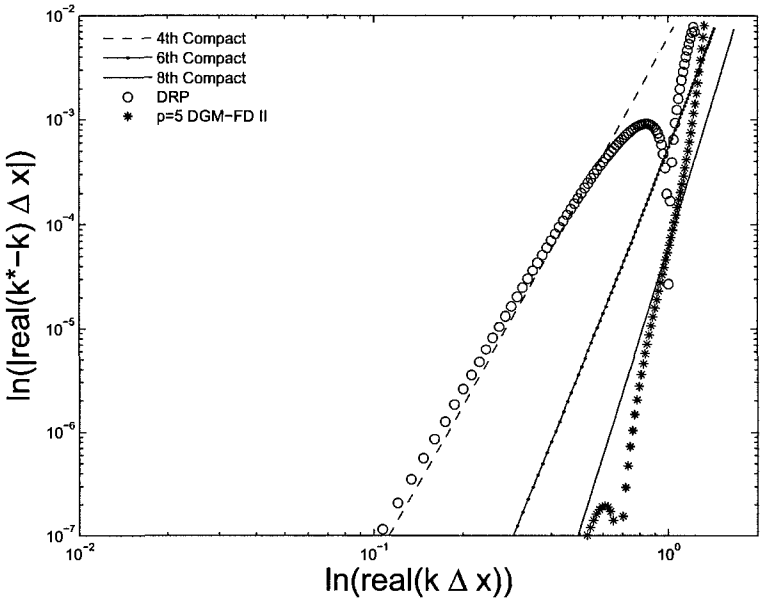

FIG. 49: loglog(real(k*-k)) Compact, DRP, DGM-FD.

V.3 NUMERICAL EXAMPLES

In this section, we show numerical examples of the fifth-order finite difference scheme presented in this section. We solve the same linearized Euler equations and governing equations as presented in section **III.3**.

The mean flow Mach numbers are 0.5 and 0 in the x and y direction, respectively.

V.3.1 Linear Acoustic Example I

The first example is an acoustic pulse in free space. The computational domain is $[-110, 110] \times [-110, 110]$ with the PML absorbing condition applied for the ten grid points around the boundary [26]. Figure (50) shows the computational domain with variable grids. For the x-axis the grid starts as unrefined, with $\Delta x_1 = 1$, and $h{=}p\Delta x_1{=}5$ then $\Delta x_2 = \frac{1}{4}$, and $h{=}p\Delta_2 = 1.25$, then back to the original. The y-axis is the same. The number of collocation points on each side is 310. The initial condition is:

$$\rho(x,0) = e^{[-ln(2)(\frac{x^2+y^2}{9})]} + 0.1e^{[-ln(2)(\frac{(x-67)^2+y^2}{25})]}, \quad u(x,0) = 0.04ye^{[-ln(2)(\frac{(x-67)^2+y^2}{25})]}$$

$$v(x,0) = -0.04(x-67)e^{[-ln(2)(\frac{(x-67)^2+y^2}{25})]}, \quad p(x,0) = e^{[-ln(2)(\frac{x^2+y^2}{9})]}$$

Density contours and a comparison with the exact solution for $t{=}30$, 60, 80 and 100 are shown in Figures (51) and (52). They show smooth contours and good agreement with the exact solution. The numerical simulation is run to $t{=}1000$.

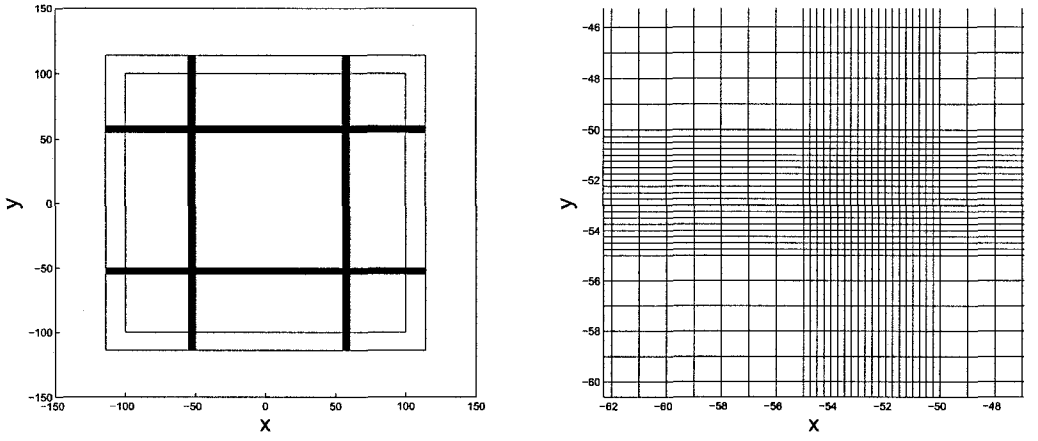

FIG. 50: Computational domain with variable grid sizes.

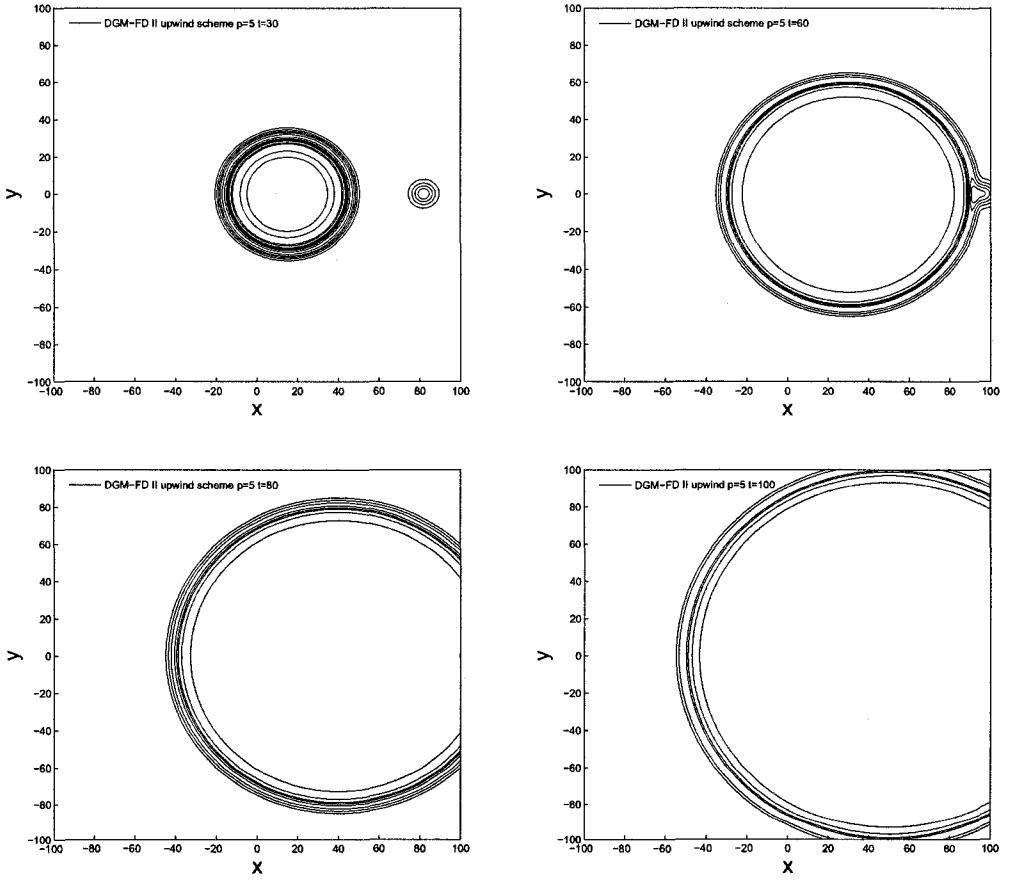

FIG. 51: Contours of density at $t = 30, 60, 80, 100$ in the physical domain.

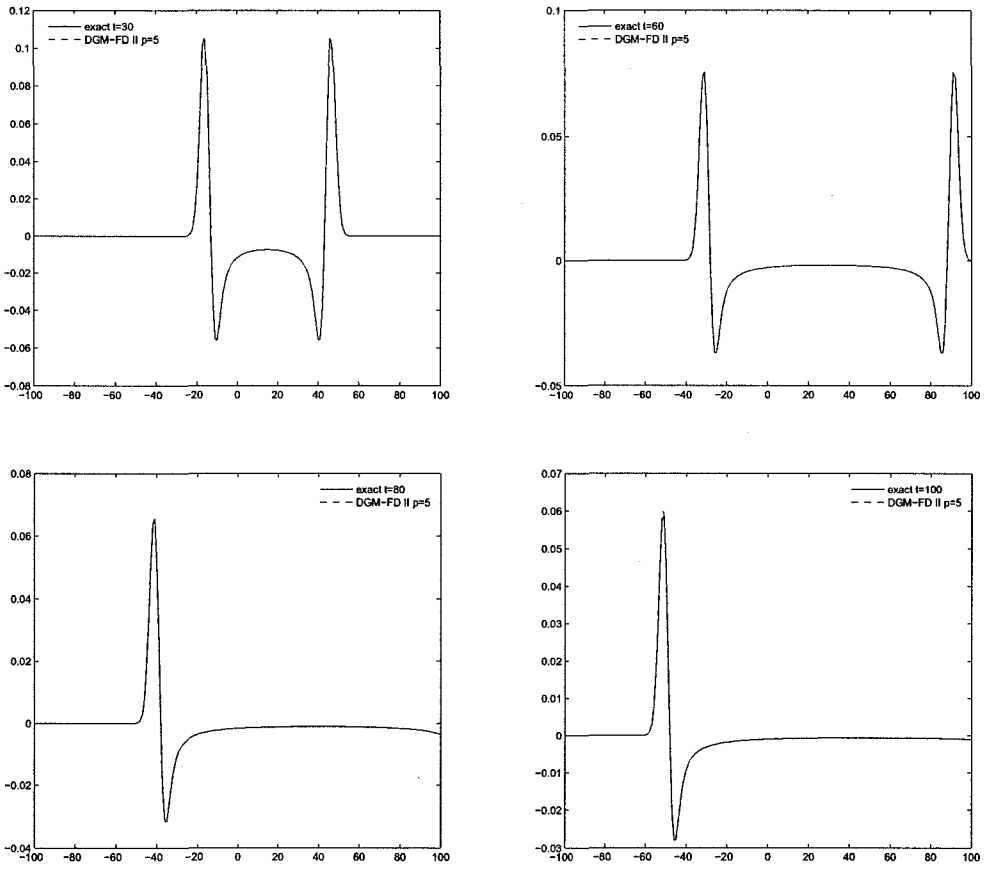

FIG. 52: Comparison of pressure with exact solution along $y = 0$.

V.3.2 Linear Acoustic Example II

This example is the reflection of an acoustic pulse with a wall at $y = 0$. The computational domain is $[-110, 110] \times [0, 220]$ with the PML absorbing condition applied for the ten grid points on the left and right and twenty grid points on the top boundary [26]. The initial condition is the following:

$$p(x,0) = \rho(x,0) = e^{[-ln(2)(\frac{x^2+(y-25)^2}{25})]}, u(x,0) = v(x,0) \equiv 0$$

Density contours, Figure (53), and a comparison with the exact solution, Figure (54), again, shows strong agreement for numerical results for upwind scheme $p = 5$ at t=30, 60, 100, and 150. The numerical simulation is run to t=2000.

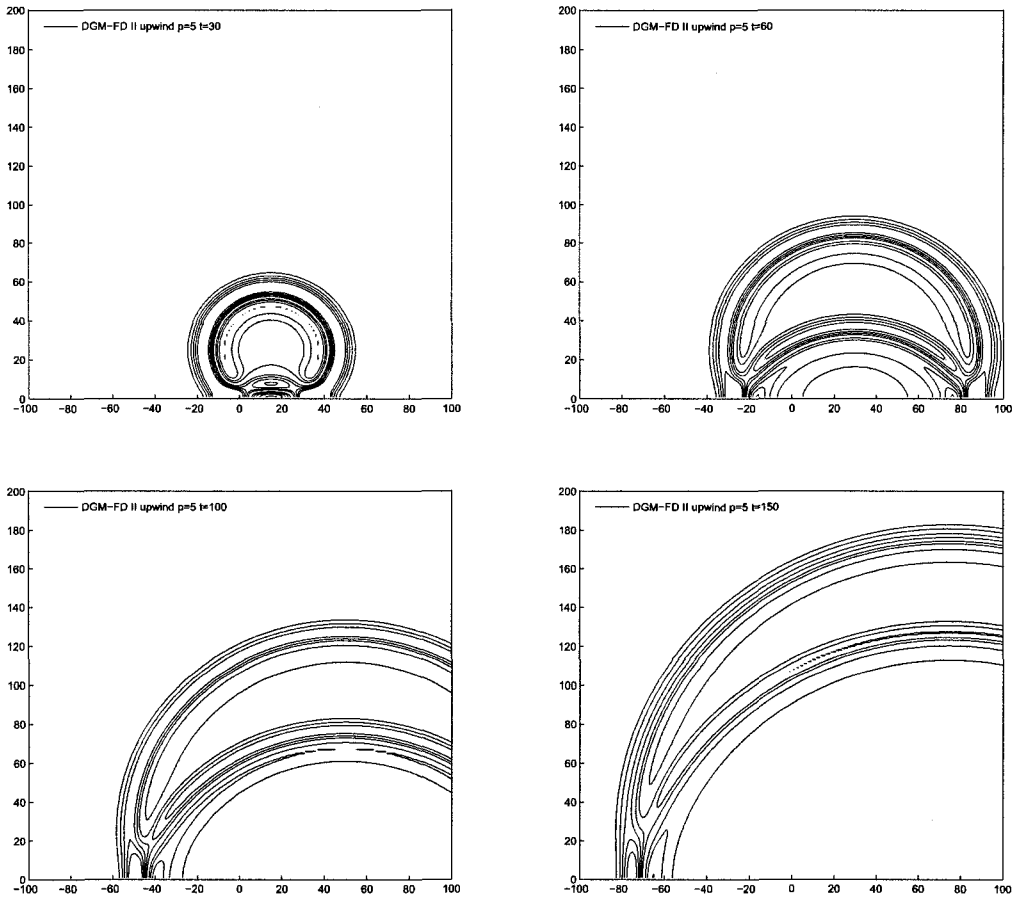

FIG. 53: Contours of density at $t = 30, 60, 100, 150$ in the physical domain.

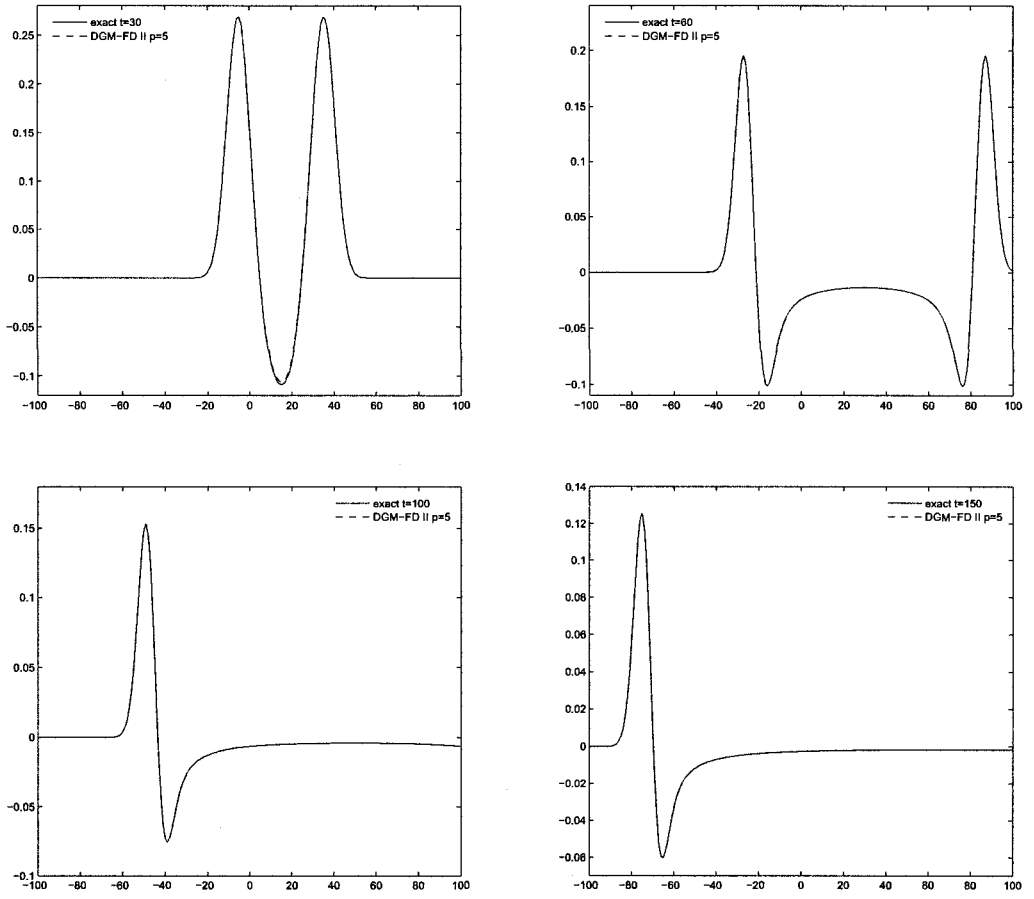

FIG. 54: Comparison of pressure with exact solution along $y = 0$.

Chapter VI

CONCLUSIONS

Numerical schemes for Computational Aeroacoustics problems require low dissipation and low dispersion errors along with high order accuracy, flexibility with variable grid refinements, and then preferably, ease of use. There are many methods that do some of these things well, at the expense of others. The method introduced in this research, DGM-FD, is an attempt to join those methods as one that achieves some of requirements of effective numerical schemes for CAA. DGM-FD is a finite difference type method that has high-order convergence with strong accuracy for numerical wave numbers and is adaptive to non-uniform grids. Like DGM, these methods retain super-accuracy for wave propagations. Of the two grid structures presented, the first has a finite difference type grid with capacity for non-uniform regions as shown with the fourth-order upwind and third order central schemes. The second structure has a shortened stencil for the derivative scheme, with some grid points double-valued and is, again, adaptive to non-uniform grids as the fifth-order upwind scheme shows. For non-linear applications a third order flux finite difference formula is presented where no explicit upwind and downwind split of the flux is required. The schemes achieve stable boundary closures while retaining the formal and wave number super-accuracy for wave propagation problems. Good results in the numerical examples demonstrate the effectiveness of the new schemes and, as the examples show, DGM-FD makes the case for being a strong contender as a useful method for CAA wave propagation applications. It has good numerical wave number and high order accuracy, stable closure and, distinct from other finite difference methods currently used, is dynamically adaptable to non-uniform grids. As DGM-FD is based on DGM, a well known and studied finite element method with many variations presented in the literature, DGM-FD, while new, is not without pedigree. This research also presents a new way to obtain, via extraction from the semi-discretized wave equation, a finite difference method.

While the fourth order DGM-FD does preserve wave number accuracy as well as DRP, it is seemingly more costly as for Grid Structure I, the stencil size is almost doubled, and for Grid Structure II, while having a more compact footprint, some duplicate grid points are required. DGM-FD has, however, a higher order accuracy in numerical wavenumber than DRP. One may consider the fourth order method

proposed in Grid Structure I to be comparable, in cost, to a 15 point finite difference scheme, which is 14^{th} order. However, closure for such a scheme, in traditional finite difference methods, would be prohibitive, and, if possible, would likely reduce the formal order of that method. Note that with the use of Chebychev-Lobatto collocation points, very high order with stable closure methods are possible with DGM-FD. Overall, for an application that requires selective refinement in certain portions of the mesh, DGM-FD is a strong candidate.

The flux formulation provides, perhaps, the best example of what is effective about DGM-FD. It handles non-linear applications in conservation form, and, unlike traditional high-order finite difference upwind schemes, wave splitting is not needed. It provides the strong convergence and wave number accuracy properties we seek with an adaptability to non-uniform meshes. Indeed, in order to execute the Burger's equation with comparable resolution, as shown in the example in section **IV.2.1**, DRP or compact schemes would require three times as many collocation points as DGM-FD needed to provide results presented in this research.

On the topic of the variable grid properties of DGM-FD, Grid Structure II provides availablity of a grid variation usually seen only in FEM, that is, where the refined area may be limited to a small local region. Grid Structure II also shows simplicity in the stencil size as well as boundary closure. Both Structures I and II merit further exploration with performance in applications due to their respective strengths.

Future work is in two directions, with the first, to improve the method in terms of ease of use, and second, to explore its effectiveness in a wider range of applications.

BIBLIOGRAPHY

[1] S. Adjerid, M. Aiffa and J. E. Flaherty, High-order finite element methods for singularly perturbed elliptic and parabolic problems, SIAM Journal Applied Mathematics, 55, No. 2, 520-543, 1995.

[2] S. Adjerid, K.D. Devine, J.E. Flaherty, L. Krivodonova, A posteriori error estimation for discontionuous Galerkin solutions of hyperbolic problems, Computer Methods in Applied Mechanics and Engineering, 191, 1097-1112, 2002.

[3] M. Ainsworth, Dispersive and dissipative behaviour of high order discontinuous Galerkin finite element methods, Journal of Computational Physics, Vol. 198 n.1, 106-130, 2004.

[4] G. Ashcroft and X. Zhang, Optimized prefactored compact schemes, Journal of Computational Physics, Vol. 190 n.2, 459-477, 2003.

[5] H. Atkins, C.-W. Shu, Quadrature-free implementation of discontinous Galerkin methods for hyperbolic eqations, AIAA Journal, Vol. 36, 775, 1998.

[6] F. Bassi, S. Rebay, A high-order accurate discontinous finite element method for the numerical method for the numerical solution of the compressible Navier-Stokes equation, Journal of Computational Physics, 131, 267, 1997.

[7] K.S. Bey, J.T. Oden, A Runge-Kutta Discontinous Galerkin finite element method for high speed flows, 10^{th} *AIAA* Computational Fluid Dynamics Conference, Honolulu, Hawaii, June 24-27, 1991.

[8] R. Biswas, K.D. Devine, J. Flaherty, Parallel, adaptive finite element methods for conservation laws, Applied Numerical Mathematics, 14, 255-283, 1994.

[9] J. P. Boyd, Chebychev and Fourier Spectral Methods, 2^{nd} ed., Dover, Minneola, New York, 86, 98-108, 570, 2000.

[10] M. H. Carpenter , D. Gottlieb , S. Abarbanel, The stability of numerical boundary treatments for compact high-order finite-difference schemes, Journal of Computational Physics, Vol. 108 n.2, 272-295, 1993.

[11] M. H. Carpenter , D. Gottlieb, Spectral Methods on Arbitrary Grids, Journal of Computational Physics, Vol. 129, 74-86, 1996.

[12] N. Chevaugeon, K. Hillewaert, X. Gallex, P. Ploumhans, J.-F. Remacle, Optimal numerical parameterization of discontinuous Galerkin method applied to wave propagation problems, Journal of Computational Physics, Vol. 223, 188-207, 2007.

[13] B. Cockburn, C.-W. Shu, TVB Runge-Kutta local projection discontious Galerkin finite element for conservation laws II. General framework, Mathematical Computing 52, 411, 1989.

[14] B. Cockburn, S.Y. Lin, C.-W. Shu, TVB Runge-Kutta local projection discontious Galerkin finite element for conservation laws III. One dimensional systems, Journal of Computational Physics, 84, 90, 1989.

[15] B. Cockburn, G.E. Karniadakis, C.-W. Shu, The Development of Discontinous Galerkin Methods, lecture notes in computational science and engineering, or in *Discontinous Galerkin Methods*, edited by B. Cockburn *et. al.*, pg 3 (Springer-Verlag, Berlin, 2000).

[16] B. Cockburn, C.-W. Shu, The Runge-Kutta discontinous Galerkin method for the conservation Laws, V, Journal of Computational Physics Vol. 141, 199-224, 1998.

[17] B. Cockburn, Devising discontinous Galerkin methods for non-linear hyperbolic conservation laws, Journal of Computational and Applied Mathematics, Vol. 128, 187-204, 2001.

[18] R. Falk, Analysis of finite elemement methods for linear hyperbolic problems, First international Symposium on Discontinous Galerking Methods (B. Cockburn, G.E. Karaidakis, and C.-W. Shu, eds.), Lecture notes in Computational Science and Engineering, vol. 33, Springer Verlag, May 1999.

[19] A. M. Fernando, F. Q. Hu, A Finite Difference Scheme Based on the Discontinous Galerkin Method Applied to Wave Propagation, AIAA Paper, 2008-2874, 2008.

[20] J.E. Flaherty, L. Krivodonova,J.-F. Remacle, M. S. Shephard, Aspects of discontinous Galerkin methods for hyperbolic conservation laws, Finite Elements in Analysis and Design, Vol. 38, 889-908, 2002.

[21] D. Gottlieb, J.S. Hesthaven, Spectral methods for hyperbolic problems, Journal of Computational and Applied Mathematics, Vol. 128, 83-131, 2001.

[22] T. Hagstrom, J. Goodrich, I. Nazarov and C. Dodson, High-order methods and boundary conditions for simulating subsonic flows, AIAA paper 2005-2869, 2005.

[23] R. Hixon, Prefactored small-stencil compact schemes, Journal of Computational Physics, Vol. 165 n.2, 522-541, 2000.

[24] F. Q. Hu, M. Y. Hussaini and J. L. Manthey, Low-Dissipation and Low-Dispersion Runge-Kutta Schemes for Computational Acoustics, Journal of Computational Physics, Vol. 124, 177-191, 1996.

[25] F. Q. Hu, M. Y. Hussaini and P. Rasetarinera, An analysis of the discontinuous Galerkin method for wave propagation problems, Journal of Computational Physics, Vol. 151, 921-946, 1999.

[26] F. Q. Hu, A stable,Perfectly Matched Layer for linearized Euler equations in unsplit physical variables, Journal of Computational Physics, Vol. 173, 455-480, 2001.

[27] F. Q. Hu and H. L. Atkins, Eigensolution analysis of discontinuous Galerkin method. Part I, One space dimension, Journal of Computational Physics, Vol. 182, 516-545, 2002.

[28] F.Q. Hu, X. D. Li, D. K. Lin, Absorbing boundary conditions for nonlinear Euler and Navier-Stokes equations based on the Perfectly Matched Layer technique, To appear Journal of Computational Physics, 2008.

[29] C. Johnson, J. Pitkarnata, An analysis of the discontinous Galerkin method for a scalar hyperbolic equation, Mathematical Computing, 46, 1, 1986.

[30] S. K. Lele, Compact finite difference schemes with spectral-like resolution, Journal of Compututational Physics, Vol. 103, 16, 1992.

[31] P. Lesaint, P.A. Raviart, On a finite element method for solving the neutron transport equation, Mathematical Aspects of Finite Elements in Partial Differential Equations, Academic Press, San Diego, 89-145, 1974.

[32] A. Zhou, Q. Lin, Optimal and superconvergence estimates of the finite element method for scalar hyperbolic equations, Acta Math Sci. 14, 90-94, 1994.

[33] Q. Lin, N. Yan, A.-H.Zhou, An optimal error estimate of the discontinous Galerkin method, Journal of Engineering Mathematics, 13, 101-105, 1996.

[34] Y. Liu, M. Vinokur, Z. J. Wang, Spectral difference method for unstructured grids I: Basic formulation, Journal of Computational Physics,Vol. 216, 780-801, 2006.

[35] R. B. Lowrie, Compact high-order numerical methods for hyperbolic conservation laws, Ph.D. thesis, University of Michigan, 1996.

[36] E. Marchendise, N. Chevaugeon, J.-F. Remacle, Spatial and spectral superconvergence of discontinous Galerkin method for hyperbolic problems, Journal of Computation and Applied Mathematics, Vol. 215, 484-494, 2008.

[37] T.E. Peterson, A note on the convergence of the discontinous Galerkin method for a scalar hyperbolic equation, SIAM Journal Numerical Analysis, Vol. 28, No. 1, 133-140, February 1991.

[38] M. Popescu, W. Shyy, M. Garbey, Finite volume treatment of dispersion-relation-preserving and optimized prefactored compact schemes for wave propagation, Journal of Computational Physics, Vol. 103, 705-729, 2005

[39] W.H. Reed, T.R. Hill, Triangular Mesh Methods for the Neutron Transport Equation, Los Alamos Scientific Laboratory Report LA-UR-73-479, 1973.

[40] G.R. Richter, An optimal-order error estimate for the discontinous Galerkin method, Mathematical Computing, 50, 75, 1988.

[41] C. K. W. Tam and J. C. Webb, Dispersion-relation-preserving schemes for computational acoustics, Journal of Computational Physics, Vol. 107, 262-281, 1993.

[42] Z.J. Wang, Spectral (Finite) Volume Methods For Conservation Laws on Unstructured Grids, Journal of Computational Physics, Vol. 178, 210-251, 2002.

[43] Z.J. Wang, Y. Liu, Spectral (Finite) Volume Method For Conservation Laws on Unstructured Grids II. Extension to Two-dimensional Scalar Equation, Journal of Computational Physics, Vol. 179, 665-697, 2002.

[44] Z.J. Wang, Y. Liu, Spectral (Finite) Volume Method For Conservation Laws on Unstructured Grids III: One Dimensional Systems and Partition Optimization, Journal of Scientific Computing, Vol. 20, No. 1, February 2004.

[45] Z.J. Wang, L. Zhang, Y. Liu, Spectral (finite) volume method for conservation laws on unstructured grids IV: extension to two-dimensional systems, Journal of Computational Physics, Vol. 194, 716-741, 2004.

[46] Q. Zhou, Z. Yao, F. He, M.Y. Shen, A new family of high-order compact upwind difference schemes with good spectral resolution, Journal of Computational Physics, Vol. 227, 1306-1339, 2007.

APPENDIX A

NINTH ORDER COEFFICIENTS FOR GRID STRUCTURE II

Grid Structure II with p=9 uses Chebychev-Lobatto collocation points on [-1,1]. They are

ξ_i	collocation points
$\xi_{1,10}$	$\mp 1.$
$\xi_{2,9}$	$\mp.9396926207859083840 5$
$\xi_{3,8}$	$\mp.7660444431189780352 0$
$\xi_{4,7}$	$\mp.5000000000000000000$
$\xi_{5,6}$	$\mp.1736481776669303488 9$

The general finite difference matrix, $\mathbf{D}_\theta$ is the linear combination

$$\mathbf{D}_\theta = (1+\frac{\theta|a|}{a})\bar{\mathbf{M}}_- + (\bar{\mathbf{M}}_0 + \frac{\theta|a|}{a}\bar{\mathbf{N}}_0) + (1-\frac{\theta|a|}{a})\bar{\mathbf{M}}_+$$

where $\bar{\mathbf{M}}_-$, $\bar{\mathbf{M}}_0$, $\bar{\mathbf{N}}_0$ and $\bar{\mathbf{M}}_+$ are the required coefficient matrices. The distinct entries of the scheme are contained in $\bar{\mathbf{M}}_- = [m{-}_{ij}]$ and $\bar{\mathbf{M}}_0 = [m0_{ij}]$ and are given in columns of coefficients below. The patterns, (69) and (70), to recover the other coefficients are given for general order, p. Recall, see coefficient matrices of p=5 scheme from **V.1.1**, that some matrices are sparse. In (69), the entries of $\bar{\mathbf{M}}_-$, $\bar{\mathbf{N}}_0$ and $\bar{\mathbf{M}}_+$ that are not specified, are zero.

$$\bar{\mathbf{M}}_-(i,p{+}1) = -\bar{\mathbf{M}}_+(p{+}2{-}i,1) = -\bar{\mathbf{N}}_0(p{+}2{-}i,p{+}1) = -\bar{\mathbf{N}}_0(i,1) \;\; i=1,...(p{+}1). \tag{69}$$

Also,

$$\bar{\mathbf{M}}_0(i,j) = -\bar{\mathbf{M}}_0(p+2-i,p+2-j) \;\; i,j=1...(p+1). \tag{70}$$

$m{-}_{ij}$	$j = 10$
$m{-}_{1j}$	-25.000000000000000002
$m{-}_{2j}$	-2.0549971056719608166
$m{-}_{3j}$	0.078351094085155344510
$m{-}_{4j}$	0.39834976196289062497
$m{-}_{5j}$	-.58977617387944402655
$m{-}_{6j}$	0.69081456438989187085
$m{-}_{7j}$	-.76021194458007812500
$m{-}_{8j}$	0.83146006813753769700
$m{-}_{9j}$	-.97047036698305506775
$m{-}_{10j}$	2.5000000000000000002

$m0_{ij}$	$j = 1$	$j = 2$
$m0_{1j}$	-2.166666666666666668	33.163437477526358434
$m0_{2j}$	-6.2358622637096287883	4.0165432841750743798
$m0_{3j}$	2.0588069485181022679	-5.7587704831436335364
$m0_{4j}$	-1.3983497619628906247	2.2743160852065152257
$m0_{5j}$	1.1948453302447455690	-1.3054072893322786049
$m0_{6j}$	-1.1168366121503537072	0.89819757022257379872
$m0_{7j}$	1.0935452779134114582	-.69459271066772139545
$m0_{8j}$	-1.1145786509954862538	0.58625682771454451228
$m0_{9j}$	1.2282431680144959126	-.53208888623795607056
$m0_{10j}$	-3.0000000000000000000	1.0310912041257633789

$m0_{ij}$	$j = 3$	$j = 4$	$j = 5$
$m0_{1j}$	-8.5486321704130304526	4.0000000000000000012	-2.4202766254612061703
$m0_{2j}$	5.7587704831436335363	-2.2743160852065152261	1.3054072893322786043
$m0_{3j}$	0.92701972987265452789	3.7587704831436335362	-1.6880592574919707132
$m0_{4j}$	-3.7587704831436335357	0.33333333333333333309	3.0641777724759121402
$m0_{5j}$	1.6880592574919707140	-3.0641777724759121419	0.89523555430241985444
$m0_{6j}$	-1.0641777724759121408	1.4844543979371183108	-2.8793852415718167676
$m0_{7j}$	0.78986168726939691506	-1.0000000000000000001	1.4844543979371183102
$m0_{8j}$	-.65270364466613930225	0.78986168726939691530	-1.0641777724759121407
$m0_{9j}$	0.58625682771454451210	-.69459271066772139547	0.89819757022257379838
$m0_{10j}$	-1.1324743314317942274	1.3333333333333333336	-1.7040881910418473459

APPENDIX B

NUMERICAL WAVE NUMBER CALCULATION

Starting with the definition of the Fourier transform of a continuous function, this section derives the formula used in **III.2.2** and **V.2.2** to obtain $[k^* - k]$, the difference of discrete numerical wave numbers, via Fast Fourier Transform (FFT) from the numerical data.

Consider the one-dimensional wave equation (5) with an initial condition: $u(x,0) = f(x)$ and exact solution $U(x,t) = f(x-t)$ after time t. The Fourier transform of $f(x)$ is

$$\hat{f}(k) = \frac{1}{2\pi}\int_{-\infty}^{\infty} e^{-ikx} f(x)dx \tag{71}$$

with inverse

$$f(x) = \int_{-\infty}^{\infty} e^{ikx}\hat{f}(k)dk. \tag{72}$$

Then

$$U(x,t) = f(x-t) = \int_{-\infty}^{\infty} e^{ik(x-t)}\hat{f}(x)dx = e^{-ikt}\int_{-\infty}^{\infty} e^{ikx}\hat{f}(k)dk. \tag{73}$$

Now, the Fourier transform of $U(x,t)$ is

$$\hat{U}(k,t) = \frac{1}{2\pi}\int_{-\infty}^{\infty} e^{-ikx}U(x,t)dx \tag{74}$$

and using (73)

$$= \frac{1}{2\pi}\int_{-\infty}^{\infty} e^{-ikx}\left[e^{-ikt}\int_{-\infty}^{\infty} e^{ikx}\hat{f}(k)dk\right]dx \tag{75}$$

and then (72)

$$= e^{-ikt}\left[\frac{1}{2\pi}\int_{-\infty}^{\infty} e^{-ikx}f(x)\right]dx \tag{76}$$

with (71) we get

$$= e^{-ikt}\hat{f}(k) \tag{77}$$

and because $f(x) = f(x-0) = U(x,0)$ we have $\hat{f}(k) = \hat{U}(x,0)$ or

$$\hat{U}(k,t) = e^{-ikt}\hat{U}(x,0). \tag{78}$$

Now consider the finite difference scheme on a grid of x_j with numerical solution on these grid points denoted by $u_j(t) \approx u(x_j,t)$. Define the discrete Fourier transform:

$$\hat{u}(k,t) = \frac{\Delta x}{2\pi}\Sigma_{j=-\infty}^{\infty} e^{-ikx_j}u_j(t) \tag{79}$$

with inverse:

$$u_j(t) = \int_{-\frac{\pi}{\Delta x}}^{\frac{\pi}{\Delta x}} e^{ikx_j} \hat{u}(k,t) dk \tag{80}$$

Now apply the relationship in (78) and write $\hat{u}(k,t)$ to get a relationship involving k^*, the numerical wave number of the finite difference scheme:

$$\hat{u}(k,t) = e^{-ik^*t} \hat{u}(k,0) \tag{81}$$

If we call $u_e(x,t)$ is the exact solution on the finite difference grid, apply (78) to get

$$\hat{u}_e(k,t) = e^{-ikt} \hat{u}(k,0) \tag{82}$$

where k is the exact wave number. Subsequently, we can find the difference between the numerical and exact wave numbers, $[k^* - k]$ by:

$$[k^* - k] = -\frac{ln[\hat{u}(k,t)/\hat{u_e}(k,t)]}{it}. \tag{83}$$

VITA

Anne Marguerite Fernando
Department of Mathematics and Statistics
Old Dominion University
Norfolk, VA 23529

Education:
- M.S. Applied Mathematics, Georgia Institute of Technology December 2002
- M.S. Statistics, Georgia Institute of Technology, December 1988
- B.S. Computer Science, University of Virginia, January 1986

Employment:
-Assistant Professor / Instructor of Mathematics
Georgia Perimeter College (DeKalb College), Atlanta GA, June 1990 - June 1995
-Systems Engineer IBM Corporation, Jacksonville FL, May 1989 - May 1990

Awards and Honors:
- recipient of Old Dominion University Graduate Fellowship 2007
- recipient of the Grant and Award for Areas of National Need (GAANN) Fellowship 1995 - 96 at NC State
- member of The Honor Society of Phi Kappa Phi
- member of Pi Mu Epsilon Honorary Mathematics Fraternity

Publications and Presentations:
-A Finite Difference Scheme Based on the Discontinuous Galerkin Method Applied to Wave Propagation (with F. Q. Hu), submitted AIAA 2007
-Evaluating Error Probabilities for BPSK Mobile Communication Receivers Using Saddle Point Method (with T.M. Ngyen, Q. Guo, J.Skaggs, J. Huffman, A. Jones), Industrial Mathematics Modeling Workshop, NSA funded, NC State University, Raleigh NC, August 7-16 1995
-A Finite Difference Method Based on the Discontinuous Galerkin Method Applied to Wave Propagation, 2008 SIAM Conference at ODU, Norfolk, April 2007
-Evaluating Error Probabilities for BPSK Mobile Communication Receivers Using Saddle Point Method (with Q. Guo) at N.C. State University, Raleigh, August 1995
-(F.Q. Hu presented) A Finite Difference Scheme Based on the Discontinuous Galerkin Method Applied to Wave Propagation, 14th AIAA/CEAS Aeroacoustics Conference, British Columbia, Canada, May 2007

Typeset using LaTeX.